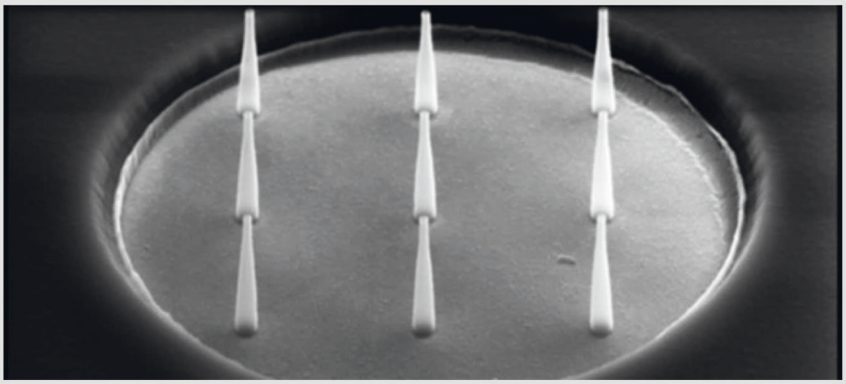

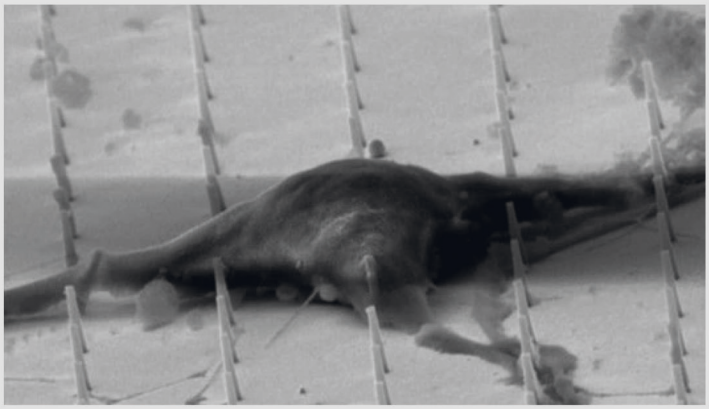

Nanostraw- Nanocavity MEAs as a new tool for long-term and high sensitive recording of neuronal signalse

Pegah Shokoohimehr

Information
Band / Volume 76
ISBN 978-3-95806-593-2

Mitglied der Helmholtz-Gemeinschaft

JÜLICH
Forschungszentrum

Nanostraw- Nanocavity MEAs as a new tool for long-term and high sensitive recording of neuronal signals

Der Fakultät für Mathematik, Informatik und Naturwissenschaften der RWTH Aachen University vorgelegte Dissertation zur Erlangung des akademischen Grades einer Doktorin der Naturwissenschaften

von

Pegah Shokoohimehr, M.Sc.

aus

Tehran, Iran

Berichter: *Prof. Dr. Andreas Offenhäusser*
Prof. Dr. Jörg Fitter

Tag der mündlichen Prüfung: *29.04.2021*

Forschungszentrum Jülich GmbH
Institute of Biological Information Processing
Bioelectronics (IBI-3)

Nanostraw-Nanocavity MEAs as a new tool for long-term and high sensitive recording of neuronal signals

Pegah Shokoohimehr

Schriften des Forschungszentrums Jülich
Reihe Information / Information Band / Volume 76

ISSN 1866-1777 ISBN 978-3-95806-593-2

Bibliografische Information der Deutschen Nationalbibliothek.
Die Deutsche Nationalbibliothek verzeichnet diese Publikation in der
Deutschen Nationalbibliografie; detaillierte Bibliografische Daten
sind im Internet über http://dnb.d-nb.de abrufbar.

Herausgeber und Vertrieb:	Forschungszentrum Jülich GmbH Zentralbibliothek, Verlag 52425 Jülich Tel.: +49 2461 61-5368 Fax: +49 2461 61-6103 zb-publikation@fz-juelich.de www.fz-juelich.de/zb
Umschlaggestaltung:	Grafische Medien, Forschungszentrum Jülich GmbH
Druck:	Grafische Medien, Forschungszentrum Jülich GmbH
Copyright:	Forschungszentrum Jülich 2021

Schriften des Forschungszentrums Jülich
Reihe Information / Information, Band / Volume 76

D 82 (Diss. RWTH Aachen University, 2021)

ISSN 1866-1777
ISBN 978-3-95806-593-2

Vollständig frei verfügbar über das Publikationsportal des Forschungszentrums Jülich (JuSER)
unter www.fz-juelich.de/zb/openaccess.

Eidesstattliche Erklärung

Ich , Pegah Shokoohimehr, erklärt hiermit, dass diese Dissertation und die darin dargelegten Inhalte die eigenen sind und selbstständig, als Ergebnis der eigenen originären Forschung, generiert wurden.

Hiermit erkläre ich an Eides statt

1. Diese Arbeit wurde vollständig oder größtenteils in der Phase als Doktorand dieser Fakultät und Universität angefertigt;

2. Sofern irgendein Bestandteil dieser Dissertation zuvor für einen akademischen Abschluss oder eine andere Qualifikation an dieser oder einer anderen Institution verwendet wurde, wurde dies klar angezeigt;

3. Wenn immer andere eigene- oder Veröffentlichungen Dritter herangezogen wurden, wurden diese klar benannt;

4. Wenn aus anderen eigenen- oder Veröffentlichungen Dritter zitiert wurde, wurde stets die Quelle hierfür angegeben. Diese Dissertation ist vollständig meine eigene Arbeit, mit der Ausnahme solcher Zitate;

5. Alle wesentlichen Quellen von Unterstützung wurden benannt;

6. Wenn immer ein Teil dieser Dissertation auf der Zusammenarbeit mit anderen basiert, wurde von mir klar gekennzeichnet, was von anderen und was von mir selbst erarbeitet wurde;

7. Kein Teil dieser Arbeit wurde vor deren Einreichung veröffentlicht. oder Ein Teil oder Teile dieser Arbeit wurden zuvor veröffentlicht und zwar in: Auflistung Datum Unterschrift.

17. Aug. 2021

Abstract

Electrical measurement of neuronal signals has enabled fundamental discoveries in neuroscience. Patch clamp method as a key standard of electrophysiological device has been shown an access to the interior single cell using an electrode. Via this method recording of the signals from the entire spectrum of the membrane potentials, from action potential down to sub-threshold signals such as post synaptic potentials, is feasible. Due to the invasive nature of this method, long term recording of the cell is challenging. Extracellular electrodes, such as microelectrode arrays, in contrast enable long term recordings of neuronal networks. However, these electrodes can only measure a fraction of the action potentials, which is due to the lack of proper cell-electrode coupling and high noise of the electrodes. Research in the last decade has been focused on overcoming these limitations. Development of the vertical 3D nanoelectrodes has allowed to access the cell's interior, however in most cases after the application of external forces such as opto/electro-poration, and therefore these transient methods are not suitable for long term recordings.

In this thesis, I developed nanostructure microelectrodes by associating two approaches of nanostraws and nanocavities. Using nanostraws facilitate penetration to the cell membrane, and the introduction of nanocavities provide high seal-resistance. The spontaneous electrophysiological recording using our nanoelectrodes demonstrate both extracellular and intracellular (20% of cases) action potentials of cortical rat neurons over long period of time. This approach enables the continuous high signal to noise ratio recordings with high sensitivity and the ability to record post synaptic potentials. To further improve the spatial resolution of neuronal network recordings, our nanoelectrodes can be integrated to CMOS-devices, which is of great interest for the neurophysiological studies.

Zusammenfassung

Die elektrische Messung neuronaler Signale hat grundlegende Entdeckungen in den Neurowissenschaften ermöglicht. Die Patch-Clamp-Methode, als wichtiger Standard elektrophysiologischer Messungen, hat als erste Methode einen Zugang zum Innersten der Zelle mittels einer Elektrode realisiert. Mit dieser Methode ist die Aufzeichnung der Signale aus dem gesamten Spektrum der Membranpotentiale, vom Aktionspotential bis hin zu unterschwelligen Signalen, wie post-synaptischen Potentialen, möglich. Aufgrund ihres invasiven Charakters ist eine langfristige Messung von Zellen schwierig. Extrazelluläre Elektroden, wie z.B. Mikroelektroden-Arrays, ermöglichen dagegen auch langfristige Messungen von neuronalen Netzwerken. Mit diesen Elektroden kann jedoch nur ein Bruchteil der auftretenden Aktionspotentiale gemessen werden. Das ist auf das Fehlen einer starken Zell-Elektroden-Verbindung und das damit einhergehende hohe Rauschen der Elektroden zurückzuführen. Daher hat sich die Forschung der letzten Jahrzehnte hauptsächlich auf die Lösung dieses Problems konzentriert. Die Entwicklung von vertikalen 3D-Nanoelektroden ermöglichte einen ersten, vielversprechenden Zugang zum Zellinneren. Das geschah jedoch in den meisten Fällen nur mit Hilfe äußerer Kräfte wie Opto/Elektro-Poration. Deswegen sind diese transienten Methoden für langfristige Messungen nicht geeignet.

In dieser Arbeit habe ich Nanostruktur-Mikroelektroden entwickelt, indem ich die Vorteile von Nanoröhren sowie von Nanokavitäten kombinierte. Während die Verwendung von Nano-Röhren das Eindringen in die Zellmembran ermöglicht, sorgen Nanokavitäten für einen hohen Abdichtwiderstand. Spontane elektrophysiologische Messungen mit unseren Nanoelektroden zeigen sowohl extrazelluläre als auch intrazelluläre (in 20 % der Fälle) Aktionspotentiale kortikaler Rattenneuronen über einen langen Zeitraum. Der Ansatz erlaubt somit kontinuierliche Messungen mit einem hohen Signal-Rausch-Verhältniss, hoher Empfindlichkeit sowie die Möglichkeit post-synaptische Potentiale aufzuzeichnen. Um die räumliche Auflösung der Messungen von neuronalen Netzwerken weiter zu verbessern, können unsere Nanoelektroden in CMOS-Geräte integriert werden. Dies ist für neurophysiologischen Studien von großem Interesse.

Table of Contents

Chapter 1. Introduction

Brain with its billions of neurons is one of the most complex units of human's body. Understanding of the information processing and the functionality of our brain are the major challenges in modern neuroscience. Our Brain consists of billions of neurons which communicate with each other. These neurons generate electrical pulses or action potential (AP), which could be recorded with the help of electronics devices. The gold standard for recording the action potential of the cell is patch clamp method [1]. This technique has been used to record the electrical activity of individual cells for in vivo [2] [3], ex vivo [4] and in vitro [2] [5] physiological studies for more than decades. The excellent electrode-cell coupling, enables to investigate the full spectrum of the electrical activities of a single cell (resting membrane potential, action potential, excitatory and inhibitory postsynaptic potential) with high resolution and high signal to noise ratio. However, this method is limited to only few cells in parallel (so far 10 cells at a time) [6], therefore it is not suitable for studying the neuronal network which is the key element of electrophysiological investigation. Another drawback of this method is short term recording, because of invasive nature of the micropipette.

To address this issue, extracellular electrophysiology systems (e.g. microelectrode arrays) have been employed to record the electrical signals of larger number of cells in parallel or small networks for long term *in vivo* [7]–[9] and *in vitro* [10]–[12] electrophysiological interrogations. Nevertheless, due to their extracellular design, monitoring the membrane potential and access into the interior cell is almost infeasible, and only a rapid membrane potential changes such as action potential can be revealed. Typically, extracellular recordings are characterized by a larger gap in the interface between the cell/tissue and the device, leads to a sealing reduction which correspond to a leakage current. Also, the small area of the recording sites, causing a higher impedance and as a result increasing the noise.

Numerous studies have been made to resolve these restrictions over the past years, to interface multiple cell types in parallel to achieve non-invasive intracellular recording over long time. By taking advantages of nanofabrication incorporating with conventional microfabrication techniques and introducing the nanosized electrodes, the new perspective architectural developments have been exploited in electrophysiological devices to enhance the extracellular recorded signals and even in some cases intracellular access. Nanomushrooms, nanopillars, vertical nanostructures, carbon nanotubes and nanostraws [13]–[38], are some of the most successful designs containing three dimensional structures with a height of few micrometers and diameters between 80 nm to 600 nm with various shapes, orientations and materials. All these vertical nanostructures are implemented on the flat substrate in order to tight the sealing with cells, engulfment and even penetration into the plasma membrane.

To understand the interface of these vertical nanostructures and the cell, different investigation methods have been performed. Microscopy technique, which includes, optical, fluorescence and electron microscopy, is the most common and fastest method to study the interface. Conventional light microscopy enables to illustrate the position of the cells on the substrate. Via fluorescence microscopy, viability, morphology and adhesion could be assessed. By staining technique, the interactions of the nanostructures with various stained- cell compartments and cytoskeletal structures could be revised [39] [40]. However, due to low resolution (sub-µm), the precise information of the interface is not accessible. In order to visualize the mentioned information with higher resolution (nm range), electron microscopy could be performed. In addition, by applying the cross section via focus ion beam (FIB), an observation of the actual interface between the nanostructures and the neuronal cell is feasible [24]. Furthermore, by using staining and resin embedding technique which has been established and developed previously, more details of the cell components such as mitochondria, nucleus, and plasma lipid bilayer could be perceived [41].

Previous studies reported that the ratio of height to diameter [42] [15] [43] [32], shape and the density of these structures [44] [40] would affect the growth, position and the interface of the cells on the structures. High aspect ratio structures (>10) [40] [45] [46] [43] [32] with sharped edge [47] [31] have been shown to have the potential of complete engulfment or even in-cell penetration [44] [17] [48] [49].

Despite of major improvements of the vertical nanostructures-cell interface, the spontaneous penetration of these structures into the cell is still a challenge. This is due to the present of plasma membrane. Among all cellular components, plasma membrane is in direct contact with the nanostructures and wrap around the nanostructures and engulf. Nevertheless, its elasticity and amphipathic structure, presents a strong layer (only 6nm thick) and avoid perturbation and accessing the cytoplasm for most of the external devices and alter the spontaneous penetration. Therefore, external forces are required in order to perturb the cell membrane and access into the cell interior. There are several available methods to enforce the penetration, among which are mechanical force, chemical approaches, electroporation [25], [31], [43], [44], [50]–[52] and optoporations [31] [44] [30], which are employed to create highly localized stress and rupture the plasma membrane and ease the penetration. However, these methods are transient and after few minutes, plasma membrane reseal the pore and avoid accessing the cell interior. Essentially, it is favorable to utilize the device and technique, enable spontaneously and continuously intracellular recording with limited amount of cell's reactions and deformations.

Additionally, improving the electrical properties of these extracellular devices by decreasing the impedance and therefore the noise reduction is taken into consideration. Some research groups endeavored to apply variant materials to reduce the impedance. Iridium oxide [49] and PEDOT-PSS [53] [54] are the exploited materials. Another attempt to improve the device performance is the employing the nanocavity which has been established and developed previously [55]–[58] It contains the cavity between the recording area and the passivation layer, which has been created

via a chemical etching process. This design could dramatically improve the signal to noise ratio, by increasing the effective area of the electrode, while maintaining the size of electrode aperture, and consequently reducing the impedance.

The purpose of this thesis is to develop the multichannel microelectrode arrays which contain nanostraws, by adjusting previous approaches. In this regard, we used high aspect ratio- sharped edge (160 nm outer diameter and 2.4 µm height) nanostraws made of (TiO_2), protruded on the flat conductive electrode (Pt/Au with 6 and10 µm diameter opening). Additionally, by implementing a sacrificial layer under the conductive electrode and etching this layer chemically, nanocavity was introduced in our MEAs. These combination, is designed to have low impedance and at the interface, nanostraw promotes the plasma membrane to seal tightly or penetrate.

In chapter 2, the fundamental theory required for the discussed topic will be explained. The principle of neuronal cells, their electrical activities and also techniques for recording these activities with the focus on extracellular (MEA) and intracellular (Patch clamp) methods will be described. In following, challenges and limitations of these recording systems and possible solutions will be discussed.

In chapter 3, an overview of the materials and methods in this thesis will be described in detail. The materials and the fabrication process using electron beam lithography and various deposition methods (e.g. PECVD, ALD) will be shown. Characterization techniques for evaluating the fabricated device, and the interface with neuronal cells (e.g. Microscopic, electrochemical and electrophysiological) will be presented.

In chapter 4, the fabrication of nanostraws on Au substrates with different spacing (1 µm, 2 µm, 4 µm, 5 µm, 10 µm and 25 µm) will be described in detail. Various microscopy characterizations (light microscopy, fluorescence microscopy, scanning electron microscopy, cross sectioning for visualizing the interface of the cell and the NS with a nanometer resolution) regarding investigation of the cell-nanostraws interface will be presented. These different spacing have been chosen to investigate and compare the interface of the cell and the nanostraw, and based on its result, the best pitch was chosen for implementing the nanostraws on the nanocavity MEAs for further studies.

In chapter 5, the fabrication of nanostraw on nanocavity MEA devices will be described. For the electrical performance of the fabricated device electrochemical spectroscopy is performed. Electrophysiological recording of neuronal cells and their interface will be the focus of this chapter and the resulted values will be discuss in detail.

In chapter 6, a summary of overall work, obtained results and the possible improvement as an outlook for further works will be discussed.

Chapter 2. Theoretical background

In this chapter, for better understanding the experimental sections, the theoretical background will be discussed. Since the main focus of this thesis is neuronal cell, its network and electrical activities, current methods for the recording the neuronal activities will be discussed. Moreover, for the study of the interface between the neuronal cell and substrate, corresponding theories and methods will be descried in detail.

2.1 Neurons

Cells, as the smallest unit of life with their individual functions and communication, facilitate the complex processes that make up human life and interaction. Among different cell types in our body, neurons are the most remarkable due to their ability to generate electrical activity (action potential (AP)) as well as propagate signals over large distances within a short amount of time. [59].

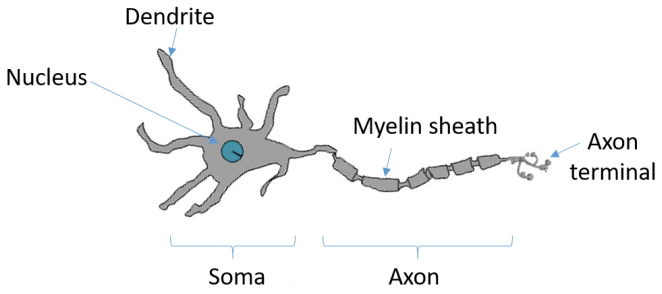

Figure 2.1 Schematic of a neuron: Soma contains cell nucleus. From soma, two types of processes spread to the direction of neighboring cells. Dendrites are responsible for receiving the information, and axon transfers information to downstream neurons via connections between the axon terminal of one cell and the dendrites of another cell. Axons are often shielded with myelin sheath in order to reduce the signal loss.

A neuron contains soma, an axon and multiple dendrites. Soma or cell body, supports the chemical processing of the neuron, such as neurotransmitter (Figure 2.1). Soma consists of cell membrane,

cytoplasm and nucleus. Nucleus has double layer membrane which one side connects to cytoskeletal networks for mechanotransduction, and on the other side connects to chromosomes for gene expression regulation. Nucleus regulates all cellular activities and is responsible for storing DNA and RNA. Cell membrane which made of phospholipids (hydrophilic phosphate groups and hydrophobic lipids) is the interface between the extracellular matrix (ECM) and cytoplasm. Cytoplasm contains cytoskeleton, Golgi apparatus, mitochondria and ribosomes, and all these compartments are responsible for cell activity and responses to an external stimuli. From soma/cell body two types of processes spread, axon and dendrites. The branches of dendrites usually spread few μm from soma and responsible for receiving information. Axon extrude from soma and extend up to meter/s long and is responsible for transferring the information. The whole cell is surrounded by the cell membrane which is supported by cytoskeleton. Cytoskeleton which is important for the membrane's interaction, is a highly dynamic polymer-like structure and responsible for cell assembly and an internal stability, keeping the position of organelles and their reorganization during division, adhesion, migration and intracellular transport [60]. Protein filaments such as microtubules, intermediate filaments and actin filaments form the cell cytoskeleton. Microtubules has a cylindrical shape with 25 nm diameter which spread from the centrosome to the plasma membrane and plays an important role for sustaining polarization of the cell [61]–[63]. Intermediate filaments with a diameter of 15 nm and the ability to self-assemble and extend up to 81 nm wide filaments [64] [65] are preserving cell shape and rigidity.

Actin filaments with diameter of 7-9 nm form by repeating the sub-units of actin monomers (G-actin), and is a semi-flexible polymer chains. They involve in polymerization and depolymerization at the edge of the cell and help kinesis of the cell. Actin filaments links to the plasma membrane through membrane-spanning proteins which allows the signals from ECM to be transmitted to the cytoskeleton and vice versa.

2.2 Membrane potential

Cell membrane, which is made of lipid bilayer, works as an electrical insulator and separates the intracellular region of the cell from the extracellular space. The membrane surrounds the cytoplasm of the cell and helps the diffusions of particular ions. The imbalance of electrical charge that exists between the outer medium and inner cell cytoplasm forms a constant voltage over the cell membrane called resting membrane potential and depends on a cell type and the extracellular region, this potential can vary between -40 mV to -80 mV. Ions are moved across the membrane by active pumps and ion transporters (sodium- potassium exchanger) with consumption of chemical energy to maintain the differences in the ionic concentration. . Knowing the intracellular and extracellular concentration of an ion you can determine what potential it generates using the Nernst equation:

$$E_j = \frac{RT}{\mathrm{zF}} In(\frac{C_j^1}{C_j^2}) \tag{2.1}$$

Where E_j is the voltage across the membrane at an equilibrium point$j$, z is the ion's charge, F is the Faraday's constant, R is the gas constant, T is the absolute temperature, and C_j^1 and C_j^2 are the ion concentrations on outside and inside the cell, respectively. It should be considered that the control of the ion flow through the membrane is mostly done by pores, pumps and ion channels, which have a 'resistivity' to the ion flow. Although cell membrane performs as a capacitor, ion channels and pores behave as variable resistors, and the adapted equation by considering a relative permittivity of each ion types is:

$$V_m = \frac{RT}{\mathrm{zF}} In(\frac{P_j[C]^1}{P_j[C]^2}) \tag{2.2}$$

Where V_m is the membrane voltage measured across the membrane, P_j is the permeability of the ion through the membrane at extracellular concentration $[C]^1$ and intracellular concentration $[C]^2$, respectively, $[C]^1$ and $[C]^2$. Ion types that give the highest current across the membrane are K^+, Na^+ and Cl^-. In this case, the membrane potential is calculated with the Goldman equation as:

$$V_m = \frac{RT}{\mathrm{F}} In(\frac{P_K[K]^1 + P_{Na}[Na]^1 + P_{Cl}[Cl]^2}{P_K[K]^2 + P_{Na}[Na]^2 + P_{Cl}[Cl]^1}) \tag{2.3}$$

Since the extracellular and intracellular is filled with electrolyte with different ionic concentration, a potential difference, membrane potential, is established. While at the equilibrium state, diffusion, pumping leakage and other interactions leads to resting potential. The voltage-activated channels enable further stimulations while ion pumps requires energy to move the ions against the electrochemical gradient.

2.3 Action potential

Several channels with various ion permeability are in the cell membrane. Stimulation, such as temperature, mechanical stress, ligand binding or a voltage across the membrane could change the permeability. Various ion types can flow across the membrane, resulting in a change of the membrane potential, from its resting potential value: The changes can be more positive (depolarization) or more negative (hyperpolarization). Voltage gated channels in the electrogenic cells can be activated, after the membrane potential crosses the threshold causing an action potential. For example in a neuronal cell, the increase of membrane potential from the rest -70 mV,

passes the threshold approximately -55 mV and results in a opened voltage gated sodium channel , and when the membrane potential reaches this value, the sodium channel opens and sodium ions flow into the cell, and potential shoots up to +30 mV (depolarization). When potassium channel open it results in a decreased in membrane potential. Sodium channel then is deactivated and repolarization occurs. At this phase, the membrane potential drops below the resting potential, hyperpolarization phase, where voltage-gated potassium channel deactivated (Figure 2.2).

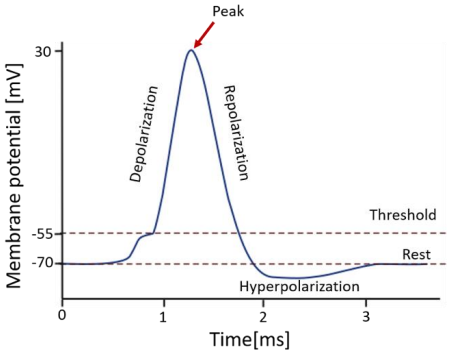

Figure 2.2 Action potential of neuron recorded by patch clamp in current clamp mode. Membrane potential increases from a resting potential to the threshold and voltage-gated-sodium channel opens which results in an overshoot and reaching the saturation of membrane potential at the peak (Depolarization). Then, the Sodium channel is deactivated, while voltage-gated potassium channels open, results in a drop of an membrane potential (Repolarization). In this phase, the membrane potential drop down the resting value (Hyperpolarization) and the voltage-gated potassium is then deactivated.

In the study of the action potential, Hodgkin and Huxley in 1952 described the equivalent circuit model [66] and how action potential in neurons initiated and propagated. This circuit (Figure 2.3) represents the electrical activity through the membrane.

The current changes through membrane is caused either by membrane capacitance (C_m), or by ion flow through a specific ion channels (resistance). Ionic currents contains potassium, sodium and leakage current (I_{Na}, I_K and I_L respectively) which each can be calculated by: $I_{Na}= g_{Na} (E-E_{Na})$, $I_K= g_K (E-E_K)$ and $I_L= g_L (E-E_L)$. E_{Na} and E_k are the equilibrium potentials, E_L is the potential when leakage current is zero. The electrical conductance (g_{Na}^+, g_K^+) which depends on membrane potential (V_m) and time (t), while leakage current represented by linear conductance (g_L). The difference in ion concentration of intra and extracellular, results in an electrochemical gradients and ion flows as voltage sources (V_{Na}^+, V_K^+). The total current through the membrane is:

$$I_m = C_m \frac{dV}{dt} + I_{Na} + I_K + I_L \quad (2.4)$$

Where V is the difference of the membrane potential to its resting potential, and t is the time.

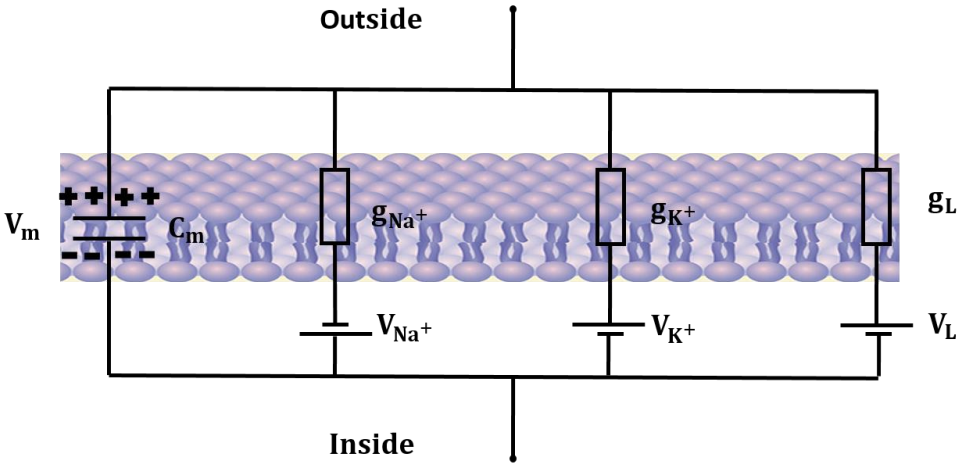

Figure 2.3 Hodgkin and Huxley equivalent circuit as an ideal electric circuit of the membrane [66]. Contains membrane capacitance, three sources of ionic flow and their corresponding conductance (g_{Na}, g_K and g_L). In case of Na^+, the current flow from outside to inside of the cell membrane. in K^- and L (leakage) the current flow from inside the cell to the outside. The potential is due to ionic concentrations differences from inside to the outside of the cell, where membrane is a barrier.

After the action potential occurs in cell body (soma), it continues to the axons. At the end of the axons, pre-synaptic site, where the neurotransmitter is released and the electrical signal converts to a chemical signal. Neighboring cells then detect the neurotransmitters via their post-synaptic site and convert the chemical signal to an electrical signal again. There is a cleft between the presynaptic and postsynaptic site of two cells called the synapse (Figure 2.4).

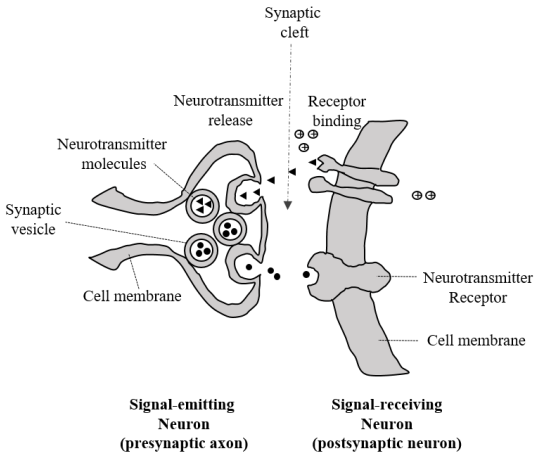

Figure 2.4 Action potential propagation by neurotransmitter release through synapse. Action potential travels down the nerve towards the synapse and neurotransmitter molecules diffuse through synaptic cleft and bind postsynaptic receptor and activate them.

2.4 Electrophysiological recording

As important part of neuroscience, the electrophysiology is a field of study, focusing on investigation of the electrical activity of the biological cells, tissues and organs. It measures the voltage/current differences of ion channels or individual cells. These approaches, compose of an electrodes which capable of recording of electrical activity of the cell on a single level and up to multiple cells (thousands of cells) and networks level for *in vitro* studies [19], [23], [36], [67]–[71] and further *in vivo* studies [72]–[74]. Electrophysiological recording are divided in to intracellular recording with patch- clamp, and extracellular recordings with microelectrode arrays (MEAs). Here, two approaches are described in detail and are performed in this thesis.

2.4.1 Intracellular recording: Patch clamp

The gold standard method to investigate the electrical activity of the cell or a tissue is the patch clamp technique. It is used to measure the cell's electrical properties and its responses to stimulation. The patch clamp technique was invented by Neher and Sakmann to analyze and detect currents from voltage gated ion channels for what they won the Nobel Prize in medicine in 1991 [75].

The actual advantage of this technique compared to the classical intracellular electrophysiology is a tight contact between the cell membrane and glass pipette (giga seal), that dramatically enhances the sensitivity, as well as negative feedback circuit in pre-amplifier that clamps the voltage or current of the membrane in voltage clamp or current clamp mode respectively. The measuring Ag/AgCl electrode placed in electrolyte solution is also utilized for stimulation and the system measures according to the Ag/AgCl reference electrode placed in bath. The pipette solution is composed of ions in concentrations comparable to the inner side of the cell, while the bath solution contained ions in concentrations suitable to the extracellular side of the cell.

The pipette's tip is brought in close contact with the cell membrane and adequate negative pressure, a seal of at least 1GΩ is formed [1]. To access the intracellular side of the membrane, short and weak suction is applied to rupture the membrane sequestrated by the pipette tip. From this point on, the cell membrane voltage and current can be clamped with high precision. In this case, due to the tight sealing, the mechanical stability is very high, with a large signal to noise ratio, recorded voltage/current (Figure 2.5). In the voltage-clamp mode, the voltage is clamped while the ion current is measured via the pipette tip. While, in current clamp, the current is clamped and the voltage is recorded. Nevertheless, by pulling out the pipette tip, the recorded cell might be stressed or die.

In general, despite of high SNR, this method is suffering from invasiveness, and not suitable for long-term recording of a single cell. Additionally, simultaneous recording from several cells and

recording from network of cells, which is the key purpose of neuroscience is not possible, and so far only 10 measurements were established.

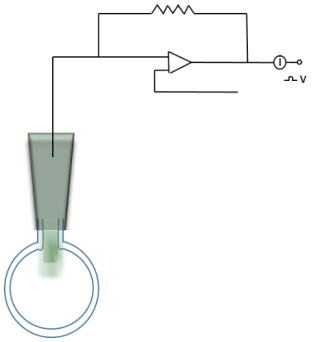

Figure 2.5 The representation of the whole-cell patch clamp technique

2.4.2 Extracellular recordings: MEAs

Another method for measuring the voltage membrane is an extracellular recording which have been used for decades [76] [77]. Unlike, patch-clamp method, this method is non-invasive and capable of long-term recording. MEA is a chip- based device consists of a multi-electrodes (in our work, 8x8 grids), insulated by a dielectric material, and connected to the contact pads. The contact pads are connected to the center of the electrode areas by metal feedlines from one side and also connected to the amplification system for visualization of the recorded signals. A total 64 electrodes are placed on the center of the device (Figure 2.6). In order to perform the electrophysiological measurement, a glass ring glued on top of the chip keeping the cell media for almost a month of culture. The important reason of using the ring is avoiding short circuit of the contact pads for connecting to the pre/and main amplifier for the recording purpose. The electrode properties, such as material and size, also the coupling of the cell and the electrode, sealing resistance, and the amplification system, are the factors affecting the signal amplitude. During an action potential, the ion current generated by a neuron capacitively coupled to the recording device. In order to record neuronal signals, cells were cultured on chips for at least 2 week, when their prominent spontaneous activities can be recorded.

Figure 2.6 Schematic of MEA design side view and top view. Yellow circle is the electrode aperture

Despite of overcoming challenges of intracellular methods, long-term and multi-parallel recording limitations, planar-MEA devices suffer from a low signal-to-noise ratio (SNR). Because of non-adequate cell-electrode coupling, signal amplitude recorded by these devices are low [78]. Moreover, the access to the interior cell as well as sub-threshold signals are almost impossible [79]. These limitations lead to loss of information regarding neuronal networks.

Nanocavity MEAs

As mentioned although microelectrodes have been used for the recording of extracellular action potential over decades, high resolution interface of the individual cells of a network is still a challenge. Utilizing small electrode aperture size for the purpose of single cell resolution, results in the high impedance of the electrode and consequently increased recorded noise amplitude and inadequate device performance. In this regard, an additional layer between the electrode surface and the passivation is utilized, and chemically etched to create cavity-like structure in the device. Chromium layer serves as this sacrificial layer due to its easily etching process via chemical etchant solution, without an additional photolithography step [58] [56] and depending on the etching time, the size of the nanocavity can vary (Figure 2.7). The introduction of nanocavity could improve the device performance dramatically by reducing the impedance of the electrode, while keeping the aperture size of the electrodes for the purpose of single cell resolution.

Figure 2.7 Schematic of Nanocavity-MEA design side view and top view. Yellow circle is the electrode aperture. Lighter yellow square represents the cavity under the electrode aperture

Vertical nanostructure-MEAs

Another limitation of microelectrodes for the recording of an action potential is a loose coupling (which comes from a gap between the cell and the electrode opening) and therefore reduction in recorded signal. An introduction of vertical nanostructure on the surface of the electrode results in an improvement of the cell-electrode coupling due to increases of sealing resistance (R_{seal}), and therefore improving the SNR. More detail of the cell-electrode coupling and corresponding mathematical model will be described later in this chapter (Chapter 2.6).

In 2007, mushroom-shaped 3D electrodes developed by Spira Group [80], confirmed the tight seal with Aplysia Californica neurons with the dramatic increase in the recorded electrical signals up to 4.5 times compare to the previous devices [36]. Later, the interface between cell and 3D structures with various geometries and orientations were interrogated, and capability of intracellular recording using 3D mushroom-shape electrodes was confirmed [81] [34], with the positive monophasic signal shape similar to the action potential recorded by patch-clamp. In later years, other vertical nanoelectrodes were utilized in order to improve the signal amplitude recorded by extracellular electrodes, developed by other groups [19] [82] [49] [53] [83]. It is also reported that the geometry, material, and the orientation of the vertical nanostructures have high affects when interfacing cells [23] [84] . In 2011, high aspect ratio nanostraw devices developed by Melosh group confirmed the capability of intracellular access by nanostraws [37]. This nanostraw is the powerful tool for accessing the cell interior for sensing, biomolecule and drug delivery applications with 7.1% efficiency [48].

In this thesis, two mentioned approaches were implemented in our microelectrode arrays, in order to improve the total signal to noise ratio. The cooperation of high aspect ratio nanostraws and nanocavity MEAs indicates a promising tool for the recording of neuronal cell with high SNR with

the potential of spontaneous in-cell access without any external forces such as electroporation [25], [31], [43], [44], [50], [51] and optoporation [30] [44].

2.5 Electrode-electrolyte interface

When an electrode (electronic conductor) is immersed into an electrolyte (ion conductor), a layer of ion concentration is occurring at the interface. The next layer is then the opposite charge ions due to the Coulomb force which is diffusive rather than static [85] [86].
There are several models describing the double layer phenomena and presence of charge transfer at the electrode-electrolyte interface. The Helmholtz double layer is a simple theoretical consideration of the small area of the interface. (Figure 2.8).

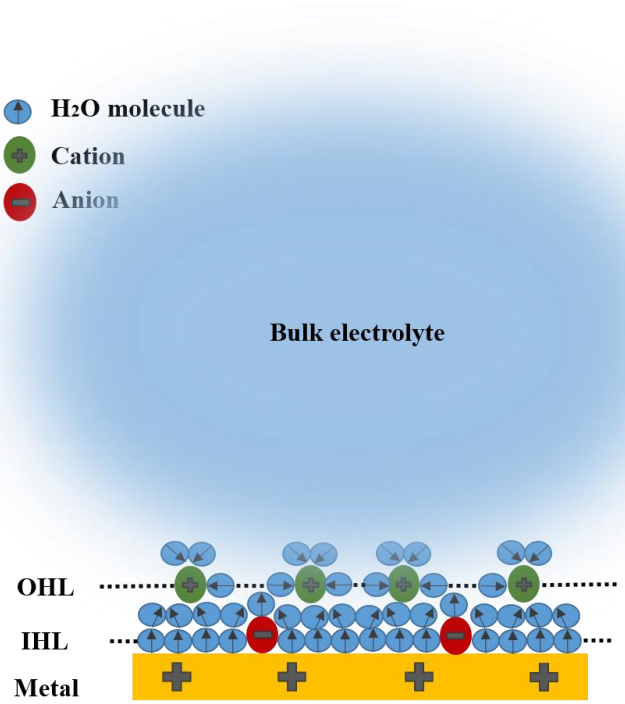

Figure 2.8 The electrical double layer representations. IHL and OHL are Inner and Outer Helmholtz layer, respectively. Green sphere marked the hydrated ions (cation), Red sphere are shown the adsorbed ions (anion) and the blue spheres represent water molecules, and arrows the direction of their dipoles [85].

The capacitance of the double layer is, as in the case of a parallel- plate condenser, is given by:

$$C_{dl} = \frac{\epsilon_0 \epsilon_r A}{d} \tag{2.5}$$

Where d is the thickness of the adsorbed layer of molecules, A is an area of the interface, ϵ_r is the dielectric constant of the medium and ϵ_0 is the vacuum permeability.
However, in this model, the capacitance is considered as a constant factor, and electrolyte is an ideal conductor, which in reality is not correct. Therefore, the Gouy-Chapman model was developed [87] [88] by considering the thermal movement of the ions and proposed a diffuse ion layers at a charged surface. In the Gouy-Chapman model, non-constant capacitance depends on an applied potential and ionic concentration [89]. The model may include double layer diffusion to better describe reality. With an increase of the distance between surface of metal and electrolyte, the electrostatic attraction decreases, and thermal energy is more dominant. A higher potential or a higher electrolyte concentration should result in a more compact layer with higher capacitance. This model is based on the Maxwell-Boltzmann statistics and depends on the charge density, temperature and potential differences between the bulk solution and metal. Ion concentration depends on the potential, ϕ, at the distance of d to the surface with the potential of ϕ_0:

$$\phi = \phi_0 \,.\, exp\,(\frac{-d}{\lambda_D}) \tag{2.6}$$

Where $\lambda_D$is the Debye length:

$$\lambda_D = \sqrt{\frac{\mathcal{E}_0 \mathcal{E}_r K_B T}{2 n_0 z^2 e_0^2}} \tag{2.7}$$

Which the ion bulk concentration in the electrolyte is n_0, with the basic charge of e_0 and ion charge of z, and the Boltzmann constant of $K_B$and temperature T.
As Figure 8 illustrates, the excess charge at the solution has the same value of the solid surface with an opposite sign. This shows that the ions are attracted to the electrode interface, while the attraction is counteract by the random thermal motion for equalization of the concentration. This equilibrium is computed with the Poisson-Boltzmann equation [86]:

$$\frac{d^2\phi}{dx^2} = \frac{\phi(x)}{\lambda_D^2} \tag{2.8}$$

Therefore, the capacity in Gouy-Chapman model is:

$$C_G = \frac{\varepsilon_0 \varepsilon_r}{\lambda_D} . cos\left(\frac{z e_0 \phi(0)}{2 K_B T}\right) \tag{2.9}$$

It should be mentioned that this model suffers from the limitation that it is based on ions, as point charges without specific sizes that are able to approach the electrode surface indefinitely close and the capacitance is increasing infinitely. In order to overcome the mentioned limitations, the Stern model combined both Helmholtz and Gouy-Chapman models, and defines the first layer of ions tightly adsorbed onto the surface and subsequent layers are formed as point charges like in the Gouy-Chapman model [90]. The capacitance of the double layer can be calculated using below equation:

$$\frac{1}{c_s} = \frac{1}{c_H} + \frac{1}{c_G} \tag{2.10}$$

The capacitance can be depicted using Helmholtz capacitance, c_H, and Gouy-Chapman capacitance, c_G in series. Since in this work, the electrode materials are gold and platinum, the double-layer capacitance is approximately $40\ and\ 55\ \frac{\mu F}{cm^2}$, respectively [86] [91] .

In case of the cell-electrode interface, multiple approaches have been used to obtain a mathematical description of the electrophysiology [92] [12] [93].

2.6 Point contact model

A model we chose to describes the neuron- electrode interface, which consists of the electrode, the neuron and the electrolyte filled cleft between these two, is the point contact model [80] [94] [95]. This model was explained by Weis in 1996 and was mostly used for the simple extracellular recording devices [93]. Figure 2.9 represents the simplified contact model of cell and electrode interface as their equivalent circuits. A cell is divided into two parts, free membrane (non-junctional membrane) that has no contact with the electrode, and junctional membrane which is located at the interface to the electrode. Both membranes can be modelled via Hodgkin-Huxley elements (see also Chapter 2.4). An electrode in this model is represented as a capacitance (C_{dl}) parallel to resistor (Z_{CPE}). As mentioned previously (Chapter 2.5) capacitance is proportional to the surface of the electrode (A), and therefore the size of the electrode has an effect on the impedance, the smaller the electrode area, the higher the impedance. Thermal noise during voltage recording is higher when the impedance of the device is high [96] [97]. Beside electrode impedance, other factors have important effects on the interface between the cell and the electrode which need to be described.

Part of the cell current leaves the system via free membrane R_m^f and the electrolyte resistance R_{sol}. The gap between the cell and the electrode is a cleft which is filled with the electrolyte (cell medium). The resistance between the cleft and the surrounding medium is represented by R_{seal} which provides a path for a current emitted from the cell and enters the cleft. Therefore due to losses over R_{seal} and capacitive coupling between the ionic conductor in the cleft and the electrode, the action potential recorded by the electrode may lose some features.

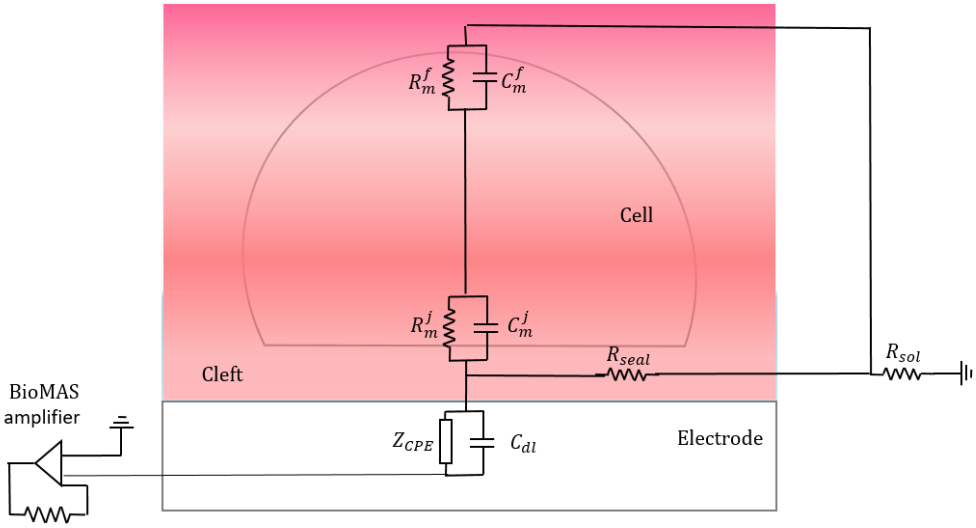

Figure 2.9 Simplified point contact model. It is divided into, cell with two elements (junctional and free- membrane), electrode and the cleft of the junction which is filled with electrolyte (cell medium).

The relation between the current density in the point contact model is calculated via Kirchhoff's law:

$$C_{dl}\frac{dV_j}{dt} + g_j V_j = C_m\frac{d(V_m - V_j)}{dt} + \sum g^{i}_{j}.(V_m - V_j - V_i) \tag{2.11}$$

Where C_{dl} is the electrode capacitance and C_m is the cell membrane capacitance. V_j is the potential inside the junction, V_m is the membrane potential and V_i presented for each ion species based on Hodgkin-Huxley model. g_j is the conductivity of the spread signal in the junction, and the g^{i}_{j} is the ion channel on the junctional membrane. Nevertheless, in this work we neglected the capacitive current at the electrode ($C_{dl}\frac{dV_j}{dt}$, because it has no influence on the action potential) and the potential inside the junction ($V_j \leq V_m$), therefore the simplified equation is:

$$g_j V_j = C_m\frac{d(V_m)}{dt} + \sum g^{i}_{j}.(V_m - V_j - V_i) \tag{2.12}$$

Due to the seal resistance R_{seal}, the part of the signal leaves the cleft, before being recorded by the electrode, and decreases the signal coupling. When the R_{seal} is larger, less current leaves the interface. The relation between the R_{seal} and the electrode impedance, Z_{CPE}, to the input signal that determines the cell-electrode coupling.
In this work, point contact model has been adjusted for the nanostraw-nanocavity MEA devices [80] [94] [93] for estimating the R_{seal} value by performing a voltage-clamp measurement and will be discussed in the chapter 5 of this thesis in detail.

Chapter 3. Material and Methods

3.1 Micro/Nano Fabrication

The production of nanostraws-nanocavity MEAs, was accomplished using cleanroom technology. The conventional processes such as deposition, photo and E-beam lithography, and etching are the main processes used in this thesis and the basics and functionality of these methods are explained here in detail.

3.1.1 Deposition

In the production of microelectrode arrays, there are different deposition techniques available. In this regard, both electrically conductive and insulating layers needs to be deposited. Thermal oxidation [98] of silicon is one method which is divided into dry and wet oxidation. By subjecting the substrate to heat, the substrate material is oxidized. In this work, a thin insulating layer (1µm) of silicon dioxide (SiO_2) is produced on silicon wafer by using oxygen as the process gas at the constant temperature above 1000 °C. Other methods for the production of thin films are physical vapor deposition (PVD) and chemical vapor deposition (CVD). In PVD, the target material is transferred from the solid phase to gas phase by evaporation or sputtering and then deposited on the substrate. On the other hand, in case of CVD process, the layer is produced through chemical reactions or deposition from the gas phase [99]. In this work, for the production of the metal layers, electron beam evaporation, which is a PVD process, was used. The deposition of different insulating layers was done via plasma enhanced vapor deposition (PECVD) and atomic layer deposition (ALD) [100].

3.1.2 Electron beam evaporation

As it is mentioned, there are two types of physical vapor deposition, evaporation and sputtering [99]. In sputtering, high energy particles are bombarded on the target, and cause the atoms of the material to enter the gas. While in the vapor deposition, the material is heated to the boiling temperature. In both methods, the gas phased material, is transported from the source to the surface of the substrate.

In electron beam evaporation, the material is heating by an electron beam until the vapor phase and transferred to sample. The electrons are emitted by a heating wire and subsequently accelerated by an anode. The electron beam is directed to the target material via magnetic field and hits the

material, which is in a solid phase in a crucible and transform into the gas phase and the material is deposited at the substrate surface [101] .

Moreover, the evaporation rate can be controlled by the electron beam. Due to the poor edge coverage of the E-beam evaporation lift-off processes can be done easier and faster. Electron beam evaporation is used to deposit a layer onto a structured photoresist, and the layer can also be structured by removing the resist.

3.1.3 Atomic layer deposition

Atomic layer deposition (ALD) is one of the CVD method. Unlike most CVD processes, in which the reactants are present at the same time and form the layer together, in ALD the individual precursors are introduced into the chamber one after the other, separated by purging steps. Since the mid-1990s, due to the down scaled size of microelectronic devices, ALD is a key process used in semicoduntor industries. Via this technique, the production of conformal thin films with high aspect ratios on non-planar surfaces was conceivable, due to its self-limiting characteristics, which restricts the reaction at the surface to only a monolayer in each cycle. The subsequent cycles result in a uniform, and pinhole free growth on high aspect ratio structures in a low temperature process, while in other deposition techniques such as CVD and PVD, due to their high temperature, fast reactions and shadowing effects [102] [103]. The other advantage is that a high conformal layer and edge coverage can be obtained with this process [104] [105]. However, ALD is a very slow process, due to the layer thickness of angtroms each cycle.

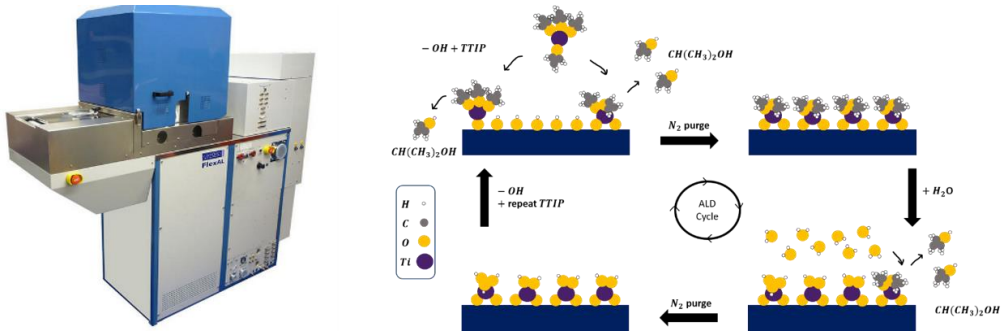

Figure 3.1 Schematic representation of ALD system and its working principle. The process starts with the entrance of the TDMAT (Tetrakis dimethylamido titanium) and its reaction with the hydroxyl groups in the chamber untill the surface is saturated. This chemical reaction produces $CH(CH_3)_2OH$, which then is released from the chamber. In the purging step, remaining TDMAT is removed from the chamber. Then water, as a second reagent, enters the chamber and reacts with the surface, forming TiO_2. This process is repeated in cycles to reach the desired layer thickness.

As mentioned, one of the advantages of ALD is the self-limiting behavior of the process, which comes from the saturation of the individual reactant reactions, and results in an extremely high control of the thickness of the deposited film. For decomposition of the surface, the use of volatile reactants are essential, and to achieve a rapid surface saturtion, a fast and irreversible reaction is required [106] [107].
Different process modes can be carried out for the deposition of the materials via ALD; thermal, plasma and radical-enhanced. ALD process can deposit various material, such as pure elements, oxides, nitrides and sulfides.
Since in this work the electron beam resist (nLOF 2020) used in the fabrication process is not stable at high temperature (above 150 °C), plasma enhanced ALD is implemented, which benefits from reducing the growth temperature to 130 °C and adapting the gas-phase chemistry for the production of thin film [108]. The deposited material is TiO_2, therefore the typical sequence of an ALD cycle for TiO_2 is shown in Figure 3.1 and described in detail below.

Firstly Tetrakis (dimethylamido) titanium (TDMAT) enters the reaction chamber and reacts with the hydroxyl groups until saturation occurs and all functional groups react with the reactant. This chemical reaction produces $CH(CH_3)_2OH$ as a by-product that is released from the chamber. Once the layer is completely saturated, the remaining TMMAT is removed from the process chamber in a purging step. Then, the second reactant, water (H_2O), enters the chamber. The water reacts with the surface until the layer is saturated again to form titanium oxide. This leads to $CH(CH_3)_2OH$ that leaves the chamber with the remaining reactants by a last purging step. At this point an atomic layer of TiO_2 is deposited and the functional groups occupy the same position on the surface like at the beginning of the cycle. Subsequently, further cycles can then be carried out in order to achieve additional atomic layers to reach the desired layer thickness (Figure 3.1).

3.1.4 Plasma enhanced chemical vapor deposition (PECVD)

Plasma enhanced chemical vapor deposition (PECVD) is another coating technique that has been used in this work for the production of the insulating layer. In this method, the deposited material is produced on the surface of the substrate by chemical reaction or decomposition from the gas phase.

In PECVD process, there are two electrodes in parallel inside reaction chamber (recipient). One of the electrode is the ground electrode which is heated and the substrate is placed on it. The other electrode is RF energized electrode. There is the reactant gas (volatile precursor) between these two electrodes, which due to the capacitive coupling between two electrodes the reactant gases are excited into a plasma. The generated plasma consists of ions and free electrons. Therefore, free radicals are generated in the plasma by the collisions of the gas molecules and the free electrons. The ionized atoms are accelerated towards the substrate which is usually located on the cathode.

As a result, the material on the surface of the substrate is coated. The reaction activated by plasma is usually performed at lower temperature (150°C - 350°C) [109] [110].

In this thesis this process was used for deposition of insulating layer. Due to its low temperature, the stress between the deposited layers and the substrate is reduced. Another important advantages of PECVD process is that with the good edge coverage a conformal layer can be achieved for deposition on the walls which is an important factor for deposition of an insulating layer.

The insulating layer produced by PECVD was the combination of silicon dioxide (SiO_2) and silicon nitride (Si_3N_4). Silicon dioxide was obtained with the reaction of silane and oxygen:

$$SiH_4\,(g) + 2\,O_2\,(g) \rightarrow SiO_2\,(s) + 2\,H_2O\,(g)$$

And silicon nitride was obtained with the reaction of silane and ammonia.

$$3SiH_4\,(g) + 4\,NH_3\,(g) \rightarrow Si_3N_4\,(s) + 12\,H_2\,(g)$$

3.1.5 Photolithography

Photolithography is an optical method for creating patterns onto a substrate. In this method, a photosensitive polymer (resist) spin coated on a wafer and then exposed to an ultraviolet light (UV) light. Due to the exposure the chemical structure in the exposed is changed, and the structure of the resist can be created after performing a development step. There are two types of photoresist, positive and negative resists (Figure 3.2).
During an exposure, the positive resists form an indene carboxylic which makes them soluble in aqueous alkaline solutions. Therefore, after exposure and subsequent development step, the exposed areas are removed while the unexposed areas remain. In contrast, the negative photoresist crossed-linked after the exposure and the molecular compounds increase, therefore, the exposed areas remain while the unexposed areas are dissolved [100] [111] [112].
After spin coating both photoresist, it is important to perform a soft bake due to the evaporation of 80% of the solvent which affects both adhesion and photo sensitivity. Additionally, after UV exposure, when using negative photoresist, the post exposure bade (PEB) is required. PEB is changing the position of the polymer molecules, results in smooth sidewalls after the development and increased resolution.
To define a desired structures on a substrate, a photomask which consist of a design, patterned in an absorption layer (Chromium) on a UV transparent substrate (quartz) is used. Due to multiple fabrication processes, the mask is aligned with the substrate using aligner markers. After the exposure, substrate is immersed into a developing solution MIF-326, which contains 0.26% Tetramethylammoniumhydroxid (TMAH) for a certain time, creating a structured photoresist.

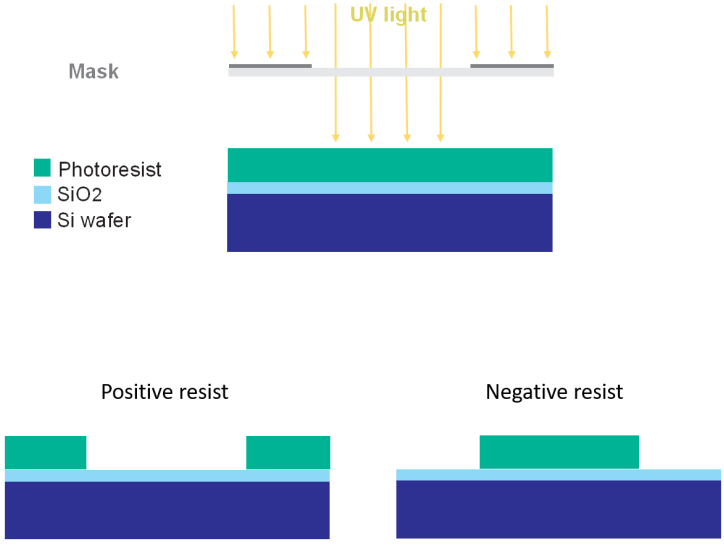

Figure 3.2 Schematic of the two different photoresists using photolithography. Positive photoresist: Exposed areas are removed after development. Negative photoresist: Exposed areas remain after development.

Both photoresists can be used for structuring layers in various purposes. In this we used photoresist for two purposes.

In metallization step, where photoresist is used in the lift-off process. First the photoresist is spin coated on the substrate, followed by exposure and development step, creating a structures made of resist. Then the metal layer is deposited on the structured resist and through a lift-off process the photoresist is removed from the substrate and the metal is structured only in areas where no resist exists.

The photoresist is also used after deposition of passivation. Here, first the passivation layer is deposited on the substrate and then the photoresist which serves as an etching mask is spin coated on the underlying layer. After an exposure (using a mask), and development step, the resist is patterned with the desired structure. The structure of the resist can be transferred to the underlying layer using an etching step. Finally the photoresist is removed and the structured layer remains on the substrate (besides the contact pads and electrode openings).

3.1.6 Electron beam lithography

For fabrication of nanostructures, electron beam lithography (E-beam) is utilized. This is due to the small size and high resolution of the electron beam. The main components of the E-beam lithography system are, the electron gun, lens for focusing the electrons, beam blanker for turning the beam on and off, stigmators for the alignment of the e-beam, vacuum for e-beam isolation from interfaces and a computer with patterning software (Figure 3.3). The complex patterns with sub-nanometer resolution are attainable via this technique [113]. However, due to the relatively high writing time of the pattern, the process is expensive with slow throughput.

The working principle is to write the pattern on an electron-sensitive photoresist. The solubility of the resist is changed when exposed to the e-beam. Depending on the type of resist (positive or negative), the exposed/unexposed area can then be removed by a development process.

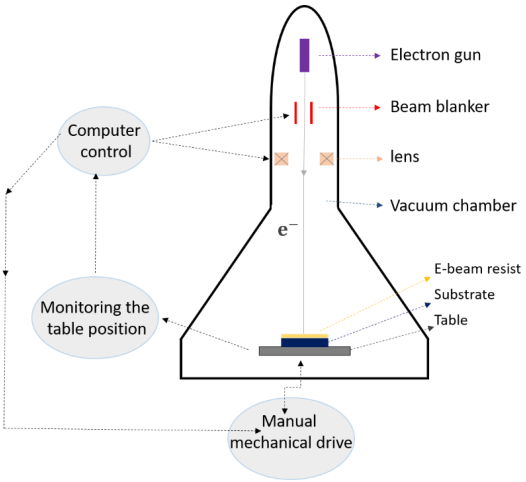

Figure 3.3 Electron beam structure. It consists of electron gun, beam blanker for turning the system on/off, lens for focusing, and mechanical drive, which can be controlled via computer.

3.1.7 Reactive ion etching (RIE)

One of the techniques for structuring the layer is etching, which is usually carried out in combination with photolithography. Since the photoresist in this process serves as an etching mask, it is important to choose the photoresist layer higher in thicknesses with slower etching rate than the target material. Different etching methods are chemical, physical or the combination of both. Wet chemical etching includes dip, spray or electrochemical etching, depends on the concentration of the etching solution, the temperature and the etching time. On the contrary, the physical etching process depends on the used gas's particle density, the gas flow, and the surface geometry. Sputter etching and focus ion beam (FIB) etching are the examples of physical etching processes. The examples of the combined chemical and physical etching technology are reactive ion beam etching (RIBE), reactive ion etching (RIE) and deep reactive ion etching (DRIE).

The resulting etched material can have different profile (isotropic or anisotropic) based on types of etching processes. In an isotropic etching, the material is etched in all directions equally. While in an anisotropic etching, material is removed in one direction. This process enables the production of high aspect ratio structures. The etching process performed in this thesis is RIE and the principle of this method is, the substrate is placed on the bottom electrode in vacuum chamber and high frequency (HF) is applied and create plasma. With the chemical attack of activated particles from the plasma, in addition to a physical attack with the ion bombardment, the etching is performed [110]. High controllability of this technique, results in a uniform etching rate and material removal.

3.1.8 Neuronal culture

Prior to culturing cells, Au samples with Nanostraws first were washed in Milli Q water. In order to avoid contamination, samples had to be sterilized. In that case, samples were immersed into a 70% Ethanol (EtOH, Merck KGaA, Darmstadt, Germany) for 30 sec and subsequently rinsed with ultrapure Milli Q water. Samples were placed in a 6-well plate. In the next step, coating was applied. For that, a 3ml solution of poly-L-lysine hydrobromide (PLL, Sigma-Aldrich, Steinheim, Germany) in Hank's balanced salt solution (HBSS, Sigma-Aldrich, Steinheim, Germany) was prepared in 1:100 dilution respectively. The protein solution was placed on samples at room temperature and incubated for 1 hour. The samples then were washed with HBSS solution and dried. The whole process was done in a laminar flow sterile hood for cell culture. The coated samples could be stored for up to one week at 4°C until cell plating.

The procedure of cortical neuron isolation is described in Appendix 2. Depending on the experiments cortical neurons in supplemented neurobasal medium were plated on each sample. The samples were then kept at 37 °C and 5% CO_2. One to four hours after plating, the medium was replaced completely with the medium. From the first day *in vitro* every three to four days, half of the medium was replaced with the fresh warm (37 °C) medium.
In this work, for the purpose of microscopy characterization 500,000 neurons in 3 ml of supplement medium (Chapter 4), and for the purpose of electrophysiological investigation 200,000 neurons in 1 ml of supplement medium (Chapter 5) were placed on each sample which will be discussed later in chapter 3 and 4 in detail.

3.2 Characterization methods

In the next part of this section, the characterization methods are explained. While ellipsometry is performed for the thickness and homogeneity investigation, multiple microscopy methods are described for study the device (nanostraw and nanostraw-nanocavity-MEAs) and cell properties. Electrochemical impedance measurements are introduced for the devices' electrical characterization, and electrophysiological recordings are performed for the cell and device interaction interrogations.

3.2.1 Ellipsometry

Ellipsometry is an optical method to determine the layer thickness of thin films. In this non-invasive technique, the change of polarization is measured after reflecting by the sample. Sunlight which is an unpolarized light, oscillate light waves in all directions, while polarized light, oscillates only in one direction. The working principle of ellipsometry is, when an unpolarized light with a single wavelength is emitted by a light source through a polarizer, the light is polarized in only one direction. Then, light is reflected at the substrate, resulting in a change of polarization that depend on several properties of the specimen such as refractive index. The analyzer records the changes and evaluates the surface properties (Figure 3.4). In case of multiple layers, due to the limitation of transmission through layers and lack of information regarding material properties, it is sufficient to identify the properties of underneath layers on the substrate, before performing the ellipsometry measurement. This help more precise and reliable measurement from the target material. After the measurement is performed, a mathematical model is used to determine the refractive index and thickness of the material, which includes theoretical properties of the interest material, such as thickness and optical properties, and fit the experimental values with. The ellipsometry can be performed to determine multiple materials, such as metals, dielectrics and semiconductors [114] [115].

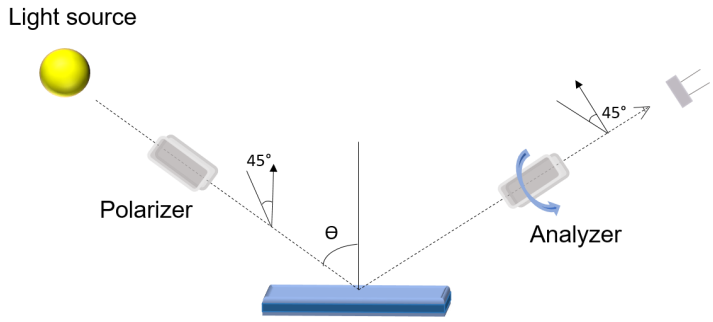

Figure 3.4 Schematic structure of an ellipsometer. Unpolarized light is polarized by polarizer and after hitting the substrate, reflecting with changes in direction of polarization. Analyzer detected the changes and evaluated the mathematical model.

In order to reach to the desired height of structures, the resist thickness after spin coating had to be examined. For that, Ellipsometry (Laser Ellipsometer Sentech SE400, SENTECH Instruments GmbH, Berlin, Germany) was utilized. Due to photosensitivity of the resist, only one sample was taken into consideration for characterization. For the thickness measurement, the sample was placed on the sample plate and positioned under the laser. Afterwards, the position of the area sampled was adjusted by focusing a reticle. The tilt of the sample plate was also adjusted in the dark tilt mode, allowing the sample to be aligned with the ellipsometer correctly, for the measurement. Furthermore, suitable model was selected for the measurement of the layer. Refractive index of all the layers were considered. After the measurement, the results were evaluated by the thickness and then adapted to the selected model via Fitting process. So, the thickness of the measured sample was obtained. In order to evaluate the accurate height, three different spots were measured [114] [115].

3.2.2 Light microscopy

After the device fabrication in order to determine the possible residues and defects, and also after the etching the sacrificial layer and creation of nanocavity and controlling the etching properties, samples were optically examined using the up-right microscope (Microscope: Axioplan 2 Imaging, Camera: AxioCam MRc 5, Zeiss- Oberkochen, Germany). The size (area) of the nanocavity was determined using the Axio Vision SE64 Software.

3.2.3 Live-dead staining (Viability assay) and fluorescence microcopy

After the neuronal culture on the substrate, in order to detect the living and dead cells, a live-dead staining was performed after three days *in vitro* (DIV) using Calcein AM and ethidium homodimer-1 (EthD-1). Calcein AM is a fluorescent dye with an excitation wavelength of 495 nm and an emission wavelength of 515 nm. The molecule, by diffusing into the cell membrane, enters the cell, and intracellular esterases, which are mainly in living cells, convert the calcein to a fluorescent phase. Thus, calcein has been chosen to stain living cells. The EthD-1 is a membrane impermeable fluorescent molecule, with an excitation wavelength of 528 nm and emission wavelength of 617 that binds to DNA. Dead cells usually have a damaged extracellular membrane; therefore EthD-1 can penetrate dead cells and stain the intracellular DNA.

The cells were washed two time with warm PBS and a mixture of 1 µl EthD-1, 1 µl Calcein Am and 10 ml of neurobasal medium was prepared and applied onto the sample and incubated for 15 min at 37 °C. The samples then were washed with PBS. Within the next 30 min the fluorescence images were taken due to the toxicity of the staining dyes. The ZEISS Axio imager Z1 (Carl Zeiss Microscopy GmbH, Oberkochen, Germany) with a 20x water objective was used. And for the image evaluation, ZEISS ZEN microscope software and ImageJ was used.

3.2.4 Cell- vertical nanostructures investigations: Plasma membrane and Actin

For development of the biosensors, understanding the interaction of cell and nanostructure, is crucial. For the last decades it is reported that the presence of vertical nanostructures (10-100 nm(s) diameters) can significantly affect cell behaviors, attachment and activity [116] [117]. It is reported that the cell appears to actively respond to the presence of nanostructures [118]. Here we analyzed the interaction of nanostraw with neuronal cell using molecular biological techniques which describe in the following section.

Plasma membrane

There are several cell components which act as obstacles to hinder the access of the vertical nanostructure in to the cell. The plasma membrane, made of phospholipids (hydrophilic phosphate groups and hydrophobic lipids) is the interface between the extracellular matrix (ECM) and cytoplasm [14] [119] [120]. It is in direct contact with vertical nanostructures, and can deform, wrap around these structures and create local high membrane curvature at the interface.
The membrane curvature is essential for the intracellular signaling [54]. However understanding of how membrane curvature is involved in the intracellular processes is challenging, due to the dynamic characteristic of the membrane curvature, and also the small size which is below the diffraction limit of visible light. Therefore precise location, observation and consequently the manipulation of membrane curvature is difficult to achieve.
Nevertheless, it is reported that when cells are in direct contact to the nanostructures, the membrane curvature can be manipulated resulting in an induced by surface topography [54].

Actin

The other barrier is the cytoskeleton, which is a highly dynamic polymer-like structure and responsible for cell shape and an internal tension balance, maintaining the position of organelles and their reorganization during division, adhesion, migration and intracellular transport [60]. Protein filaments such as microtubules, intermediate filaments and actin filaments form the cell cytoskeleton. The actin filaments of the cell wrap around vertical-nanostructures to stabilize the junctional membrane and enable tight contact [119].

Both plasma membrane and actin can be stained in both living and fixed cells to determine the structure and function of the cytoskeleton. In this work we focused on staining living cells, and this were done using transfected neuronal cells and labeling fluorescent dyes.

The procedure of transfection was firstly 3 to 5 million suspension cells were centrifuged for 3 min at room temperature and then 100 µL of nucleofector transfection solution was added to the neuronal pellet and transferred into an Amaxa cuvette which firstly filled with 3 to 6 µg of Lifeact-RFP cDNA plasmid. Directly, the transfection of the suspended cells was performed using the program G-013 of the Amaxa Nucleofector device and voltage applied. Right after the transfection, for the fast recovery and resealing the cell membrane, 1 mL of warm supplemented RPMI 1640 medium was added to the cuvette. A blue trypan blue exclusion assay was used for counting the live cells and cells were seeded with a density of 150 $\mathrm{cells/mm^2}$ on PLL-coated substrates for imaging of individual neurons. After 1 hour, the medium was exchanged with warm supplemented Neurobasal medium.

The other possibility is visualization of the interaction of the cell membrane with the nanostraw by incubation of living cells with DiI (1,1'-Dioctadecyl-3,3,3'3 Tetramethylindocarbocyanine Perchlorate; Invitrogen). Which means, neurons at DIV 4 to 8 were incubated in 5 µM DiI solution,

diluted in Phosphate Buffer Saline (PBS), for 20 min at 37 °C and subsequently three times washed with PBS solution.

In this thesis, both experiments were performed at 4-8 DIV, on a confocal laser- scanning microscope LSM 880 equipped with an Airyscan detector with super resolution imaging with increased acquisition speeds, using 63x oil immersion objective. High resolution Z-stack images were taken and the image processing is carried out in ZEISS ZEN microscope software and ImageJ.

3.2.5 Preparation and Fixation for electron microcopy

In order to investigate the interface between the cell and the substrate with nanostraw with high resolution, a complementary dual beam system containing both electron microscopy and ion beam milling (Helios NanoLab Dual-beam 600i, FEI) were used. Prior to imaging, preparation of the sample and fixation of the cells are required.

For cell fixation, firstly, the substrate was rinsed three times with warm PBS (37 °C, Sigma Aldrich, USA) and then chemically fixed with 2% glutaraldehyde (GA) (Sigma Aldrich, USA) solution in PBS for 15 min at room temperature for 15 min. Then, sample was washed three times with PBS and MilliQ water to remove the fixative residues.

In order to dry the sample before performing SEM imaging, two different techniques were used.

3.2.5.1 Critical point drying

One of this method is critical point drying (CPD). In this method water in the Fixed-cell sample was replaced with ethanol (intermediate medium) moderately, starting from 10% up to 95% concentration. The sample was incubated for 5 min in 10%, 30% and 50% ethanol, and then 15 min in 70% ethanol, and 3 times for 5 min in 90% and 95% ethanol. Then, the sample was transferred in 100% ethanol at 4 °C, and transported to the chamber of a CPD system (CPD 030, BAL-TEC Company). The chamber in the CPD system was filled with 100% ethanol. Firstly, the chamber was slowly cooled down to 10 °C, and then ethanol was exchanged by CO_2. This exchange medium process was repeated several times until the chamber was filled completely with liquid CO_2. Then, the chamber temperature and pressure was increased up to 40 °C and 73.8 bar. This process, causes the transformation of CO_2, into a supercritical phase. Eventually, the chamber was evacuated while the sample was dried and dehydrated.

In order to enhance the conductivity, a thin layer of platinum (5 nm) was sputtered on to the fixed cell sample (with the current of 15 mA for 35 sec). SEM characterization was carried out with a Gemini 1550 instrument (Leo/Zeiss) using an in-lens detector. The imaging was taken at 3 kV acceleration voltage.

However, CPD technique is restricted in shrinkage artefact during the preparation process and causing damages to cells (body, neurites). This shrinking affects is due to the liquid-gas transition which leads to surface tension, and the reduction in physiological volume up to 20% [121] [122]. Moreover, because of porous and sponge-like morphology of the cell created by this method, the intracellular membrane and other cell compartments are not evident, therefore for the investigation of interface of the cell and substrate staining and resin embedding method can be performed [23].

3.2.5.2 Staining and resin embedding

In the second techniques, after fixation procedure, sample was washed with cacodylate buffer $(Na(CH_3)_2.AsO_4.3H_2O$ two times, unlike CPD process when dehydration was performed using ethanol.

As a post fixation step, sample was immersed into a solution containing, 1% osmium tetroxide (OsO_4) in cacodylate buffer (vol/vol) and incubated for 2 hours on ice. OsO_4 works as an electron stain. In addition to penetration into the cells and organelles, many lipids and proteins in the cell are stabilized with no particular changes in their structural features. In this way, the fluidity of the plasma membrane is reduced to zero [123]. Then, sample was immersed into Milli-Q water five times, for 2 minutes each at room temperature.

Afterwards, sample was immersed into a solution containing, 1% (vol/vol) of Tannic acid and Milli-Q water and incubated for 30 minutes at room temperature. Subsequently, a solution containing 2% uranyl acetate (UrAc) in water, was applied to the sample for 5 hours at 4 °C.

The reason for using Tannic acid is its capability to facilitate the binding of heavy metal stains to the cell's structures, and as a result improving the contrast in electron microscopy imaging. It interacts with osmium in the membrane and enables the uranyl ions to bind. Another reason for utilizing Tannic acid is the protection of several proteins against possible damage during electron microscopy imaging [123] [41].

This step, additional to double fixation with GA and OsO_4, enhances the staining of the cell and its components dramatically. As the heaviest metal used for staining in electron microscopy (atomic number 92), even the a few ions bound to macromolecules are enough to be visualized in the SEM These fixative and staining characteristics of UrAc are due to its capability to react with variety of materials and containing both positive and negative charged proteins. Next, samples were washed with Milli-Q water and dehydration procedure was applied as for the CPD method (10%-100% ethanol).

For the resin procedure, the embedding polymer (which contains Epon 12, DDSA, MNA and DMP-30) prepared fresh. Samples covered with 100% ethanol were replaced gradually with resin in multiple steps (6 steps) with different concentration and incubated for 3 hours each, until the samples were covered with only a pure resin. The challenging step of this method is the removal of resin on the unwanted area. Resin polymerization was performed by incubating the samples overnight (24 hours) at 60 °C (Figure 3.5).

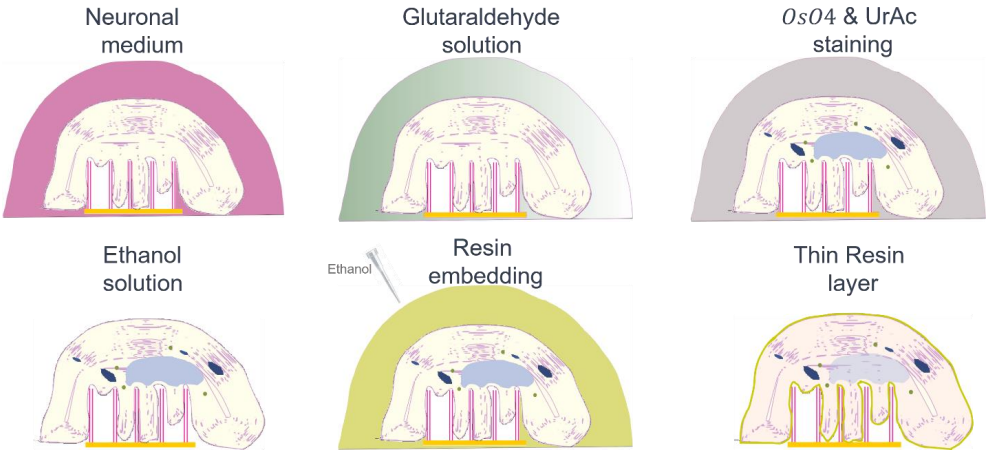

Figure 3.5 Sample preparation prior to electron microscopy using staining and resin embedding. a: Neuron on nanostraws substrate in medium on nanostraws, b: Cell fixation by applying glutaraldehyde solution. c: Second fixation and staining using solution containing OsO_4 and UrAc. d: Replacing staining solutions with ethanol. e: Infiltrated resin and removal of resin using ethanol. f: Thin resin layer on the fixed cell.

3.2.6 Scanning electron microscopy (SEM) characterization

SEM is a type of electron microscopy used for high resolution (≤10 nm) imaging of the sample which contains information about the topography of the sample. A primary beam of electrons was accelerated and focused towards the sample and scan the surface.

Various signals are produced using different modes. Secondary electron detector which is the most common mode, with low energy can pass through few nanometer of the surface of the sample, therefore the image recorded is dominant by topographic information [124]. Back scattered electrons (BSE) contain high energy and after hitting the substrate and elastic interactions with substrate's atoms, it reflected. Heavy elements backscatter electrons stronger than light elements, therefore the produced image is brighter. In this regard, BSE is mostly used to detect contrast in different areas with various chemical compositions [124]. On the other hand, the in-lens detector is located rotationally around the optical axis in the electron column of the microscope. There is a magnetic field at the column and therefore the higher efficient secondary electrons can be collected and the high contrast imaging at low voltage with small working distance is achieved. The entire process is performed in vacuum condition, and in case of a biological sample, sample preparation is required (which we performed and described previously 3.2.5).

For the high resolution investigation of both nanostraws, and neurons and corresponding interface, scanning electron microscopy (SEM) was performed. In this work SEM (Zeiss Gemini 1550 VP field emission SEM, GmbH, Oberkochen, Germany) using both secondary and in-lens detectors for assessing the quality of the fabricated nanostraw (diameter, height and shape), imaging was performed.

3.2.7 Focused Ion Beam

Focused ion beam was implemented using HELIOS NanoLab 600i (FEI Deutschland GmbH, Frankfurt, Germany) DualBeam microscope with electron and ion beam source with an angle of 52°. In order to protect the region of interest during the sectioning process, a thin layer of platinum was deposited via electron beam induced deposition (EBID) at 3 kV acceleration voltage and a current of 1.4 nA and 11 nA. Then, a thick layer of platinum (0.4 µm) was deposited via ion beam induced deposition (IBID) at 30 kV acceleration voltage and a current of 0.33 pA and 0.79 nA. Bulk milling was performed at 30 kV and a current of 0.23 nA and 2.5 nA. Furthermore, the cross section was polished with a voltage of 30 kV and a current of 0.04 nA and 0.79 nA. Cutting procedure was performed using gallium ion source. For SEM imaging, for unstained samples, 3 kV and 0.021 nA in-lens detector mode was performed, and for stained samples, backscattered electron detector was used at 3kV and 0.69 nA (Figure 3.6).

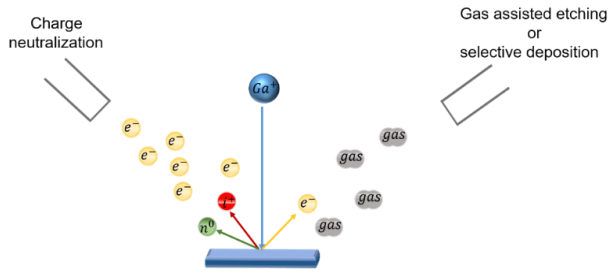

Figure 3.6 The principle of focus ion beam

3.2.8 Energy dispersive X-ray analysis (EDX)

EDX is an x-ray technique for identification of materials compositional elements. This system is attached to electron microscopy (SEM or TEM) due to the capability of the electron microscope to identify the substrate properties. After the elemental mapping of the sample and analysis with EDX, data is generated as a spectra, representing peaks which correspond to various elements which contain in the sample of interest. This non-destructive technique is a useful method for characterization of the sample and evaluating the sufficient parameters in the fabrication process, and also in contamination analysis. In this work, we performed this method to characterize the etching parameters and time for Cr layer (Chapter 5.2).

3.3 Electrochemical impedance spectroscopy

Electrochemical double layer and electrochemical impedance spectroscopy (EIS) is described in order to a better understanding of the transmission between electrolyte and electrode on microelectrode arrays. Afterwards, the electrical circuit elements and the circuit for a single electrochemical cell is discussed in order to help the EIS evaluation.

Impedance spectroscopy

Electrochemical impedance spectroscopy (EIS) defines the response of an electrical circuit due to an alternating current (AC) or voltage as a function of frequency. A small sinusoidal voltage of fixed frequency is applied to an electrochemical cell and the current response is measured and impedance is calculated. The impedance at each frequency (z) is evaluated by Ohm's law ($\frac{E_\omega}{I_\omega}$) :

$$z = \frac{E_\omega}{I_\omega} = \frac{E_0 \sin(\omega t)}{I_0 \sin(\omega t + \phi)} \tag{3.1}$$

Where t is the time point, ω is the angular frequency and ϕ is the phase shift. (Frequency dependent potential to Frequency dependent current).

The electrochemical impedance characterization has been done via VSP-300 multichannel potentiostat measurement (BioLogic Science Instruments), where consists of three electrodes immersing into a phosphate buffer saline (PBS), conductive electrolyte. These three electrodes are:

- Working electrode (WE), where the current is measured and the potential is controlled.
- Reference electrode (RE), where is a point of reference for the potential control and measurement, with a constant electrochemical potential.
- Counter electrode (CE), where carries the current and complete the circuit.

In this body of work, the electrode of the nanostraw-nanocavity MEA was used as a WE, a silver-silver chloride electrode was used as RE (in vivo Metric-'E205') and current flows between WE and CE. The potentiostat has two channels which two WE were possible to be measured simultaneously. The electrometer measured the potential difference between WE and RE, which ideally has an input current of zero and infinite impedance. The MEA is sensitive to an external noise, thus potentiostat setup is placed inside a faraday cage.

A sinusoidal excitation signal was applied with 10 mV amplitude and the frequency was scanned in the range between 1 Hz to 1 MHz and the measurement was performed. For evaluation of the result, EC- lab V 11.30 software was used.

3.4 BioMAS recording

For the electrophysiological recording of neurons, the bioelectronics multifunctional amplifier (BioMAS) system have been designed and developed in-house in IBI3 for electrophysiological measurements. All the electrical recording of the neuronal cultures were performed between 14 to 24 DIV, and there was a possibility to record a same culture in successive DIVs. The experiment was performed, using Ag/AgCl pellet electrode which was immersed in the medium for the grounding. Recording of the nanostraw-cavity MEAs with 8x8 electrode gird, was done by a 64

channel MEA amplifier system designed and developed in our institute with the gain of 10.1 [125]. The main amplifier (LM124, Texas Instruments Inc., Dallas, USA) was connected to the A/D converter (USB-6255 DAQ National Instruments, Austin Texas USA) (Figure 3.7).

Real time recording and adjustment of main amplifier settings were obtained by an in-house developed LabView script (National Instruments, Austin, USA). The sampling rate was 10000Hz, the signals were digitized at +/- 10 V ADC range. Depending of the gain of the main amplifier (10 and 100), low-pass filter at 7.2 and 8.8 Hz was used to prevent signal aligning, while high-pass filter was used to avoid potential drift. A MATLAB and Python script written in our institute were used for processing and analyzing the recorded data.

Figure 3.7 Schematic of BioMAS setup, containing main amplifier, headstage, MEA chip with a growth cells

3.5 On-chip patch-clamp recording

Patch clamp technique was performed in this work, for the purpose of evaluation of the BioMAS recorded signals from NS-NC-MEA devices. In this work, whole-cell recordings were done with amplifier EPC 10 USB (Heka Elektronik GmbH, Germany) and a PatchMaster software (Heka Elektronik GmbH, Germany), at 14-24 DIVs, after the measurements were performed via BioMAS. Before patch experiment in order to visualize cells and their positions, a light microscope (Carl Zeiss AG, Germany) was used. Both MEA and patch amplifier were connected and the

simultaneous recording were performed. To avoid grounding, a Ag/AgCl pellet electrode were used by both systems (Figure 3.8).

The working principle of the patch-clamp method is, the extracellular patch solution was replaced the culture medium, which consists of (in mM): NaCl 120, KCl 3, $MgCl_2$ 1, $CaCl_2$ 2, HEPES 2, at pH=7.3 adjusted with NaOH. Borosilicate glass micropipettes with 1.5 mm diameter, were prepared with a laser puller (P-2000, Sutter Instrument) and filled with the intracellular solution consists of (in mM): NaCl 2, KCl 120, $MgCl_2$ 4, HEPES 5, EGTA 0.2, MgATP 0.2028, at pH=7.3 adjusted with KOH. Therefore, the pipette resistance was in the range between 5-10 MΩ. The micropipette was coming to a close contact with the cell body till the giga-seal was formed, and the slight suction pulses were applied for rupturing the cell membrane and recorded by the tip of the micropipette. The sampling rate of the signal was 10000 Hz and low pass filtered using the Bessel filter at 10 kHz (filter 1) and 3 kHz (filter 2).

Both voltage clamp and current clamp mode which were performed in this work had the holding potential of -60 mV. For the voltage-clamp experiments, hyperpolarizing and depolarizing 500ms pulses were applied in the range between – 120 mV and + 100 mV and the analysis were performed via self-made Python script.

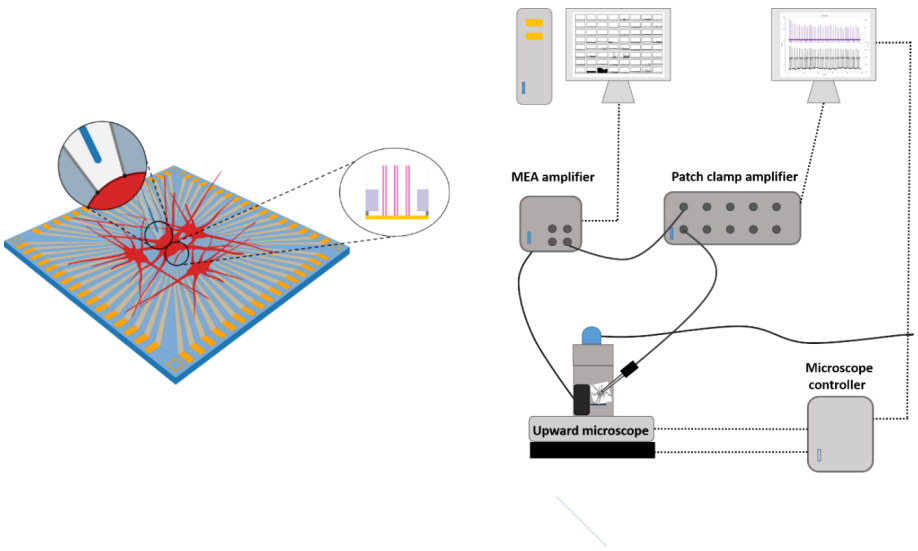

Figure 3.8 Schematic patch and BioMAS setup and their connections to the main amplifier.

Chapter 4. Nanostraws and interaction with cell membrane

As it is reported in previous studies, the interaction of cell- vertical structures is highly dependent on the geometry of the 3D structure. Features like material, shape, size, and aspect ratio, can highly influence the behavior of the cell and its interface with a 3D structure [43]. Various approaches for the fabrication of 3D structures have been presented in different research [54], e.g. for the fabrication of nanowire employing RIE [19], hollow nanostructures employing focused-ion beam milling [43] [126] , and using electron-beam structured polymers [35] [80] as a framework for the fabrication of vertical nanostructure designs. The work of Melosh group [37], using high aspect ratio nanostraws as an intracellular delivery tool, has inspired us to extend their work for our purpose of neuronal network investigation with high SNR and high sensitivity.

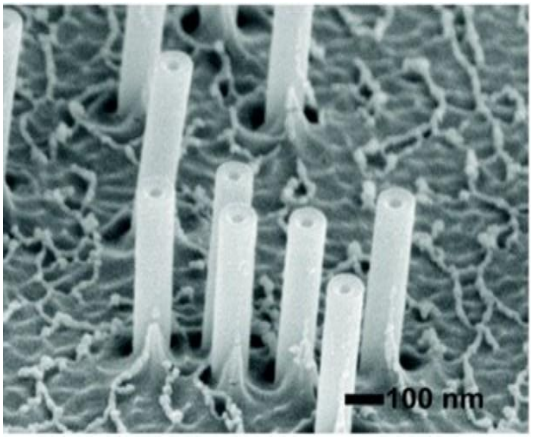

Figure 4.1 Nanostraw fabricated on tracked-etched membrane. Nanostraw fabricated by Jules [37].

The focus of Melosh for the last few years was using nanostraws, as a tool for accessing the cell interior for biomolecular delivery. In this regard, conventional polymeric tracked etch membranes were used as a template [127] [37] [38] [17] (see Figure 4.1). This material has been used for cell cultures and its biocompatibility has been proven for decades. The membrane contains pores with 150 nm diameter, which are distributed randomly in the sample. Aluminum oxide (Al_2O_3) was deposited via atomic layer deposition (ALD) all over the substrate with a thickness of 10 nm. A 5

μm thick positive photoresist was spin coated on the substrate and exposed to a square pattern of UV light and then developed to form a protective layer. In the next step, Al_2O_3 was etched via reactive ion etching (RIE) in a fast process by using BCl_3, Cl_2, and Ar. In order to reach the desired height, reactive RIE with O_2 was utilized and the resultant nanostraws were 3 μm tall [16].

As described, the template used, track etched membrane, was not a suitable material for our interest regarding the investigation of electrical behavior of neuronal networks when interfacing nanostructures. Therefore electron beam lithography was used correspondingly, and the fabrication procedure required to be adapted.

In this chapter, for the ease of production establishment, flat gold substrate was chosen and the suitable parameters were processed and nanostraws were fabricated. Then, suitable spacing between each nanostraws were taken into account and various pitches were implemented, 1-5 μm, on the same substrate. Last but not least, the interface study between primary embryonic rat cortical neurons and nanostraws with different pitches, was carried out via microscopy techniques.

In this section, the experimental work and the subsequent results will be presented and discussed. First the Nanostraws on gold samples with different pitches were fabricated and then characterized via various methods like, ellipsometry and SEM. Cortical neurons then were cultured on a substrate. Fluorescence microscopy will be shown in order to investigate the viability of the structures. Actin and membrane staining are carried out in order to interrogate the cell and nanostraw engulfment. Consequently, high resolution microscopy techniques, FIB/SEM, were performed in order to investigate the interface between the cells and the nanostraws, with nanometer resolution.

4.1 Nanostraw fabrication

The production of the samples was carried out in an ISO 1 cleanroom on n-doped silicon wafers (Si-Mat Silicon materials, Kaufering, Germany) modified with 20nm Ti and 200nm Au/Pt via electron-beam evaporation (Pfeiffer PLS 570, Pfeiffer Vacuum, Asslar, Germany). The wafers were then cut into 1.5x1.5 cm^2 samples, followed by cleaning in acetone and isopropanol for 5-10 min and dried in a stream of nitrogen. As it is mentioned, nanostraw fabrication has to be adapted for our Au substrate. Therefore we used electron beam sensitive photoresist (negative resist nLOF2020) and with the application of an electron beam lithography, nanopoles were created.

In this regard, samples were dehydrated at 150 °C for 10 min, then spin coated with nLOF2020 (Negative photoresist) at 4000rpm for 35 s. Then the samples were placed on a hot plate at 110 °C for 1min for soft-bake.

After spin coating the resist on Au substrate, for evaluating the thickness and property of the resist, ellipsometry was performed. For that, three different regions of the substrate were measured and the mean value and standard deviation were determined. The measured thickness on a sample was 2.5 µm.

In a next step, samples were transferred into a Vistec EBPG 5000plus HS (Vistec Electron beam GmbH, Jana, Germany) electron beam lithography system. The structures were written in circles of 100 nm in diameter, arranged in a square grid of 1 µm, 2 µm, 4 µm, 5 µm, 10 µm and 25 µm spacing were written (Figure 4.2a) with a doses of 1800- 2400 $\mu C / Cm^2$ (Figure 4.2b). All structures were written with a resolution of 2 nm, beam current of 100 pA, and with no proximity correction. It should be mention that although the nanostraws with 10 µm and 25 µm spacing were included in the mask and were produced each time, however no characterizations were performed on those pitches.

Before development process post exposure bake was done by placing samples on a 110 °C hot plate for 1 min. Then, development was performed by immersing the samples into MIF326 (2.38% tetramethylammoniumhydroxid (TMAH)) for 50 sec at room temperature, followed by immersing into water for few minutes in order to stop the development and drying with a stream of nitrogen. This mentioned procedures lead to creation of nanopoles on the Au substrate. For evaluating the height and the diameter of the structures, SEM were performed and sufficient value of E-beam dose was selected. After the development step and creation of nanopoles, the optimal electron beam dose was selected via SEM to assess the fabricated nanopoles properties. Therefore, due to the sufficient height (2.4 µm), diameter (inner diameter 100 nm, outer diameter 160 nm) and robustness of the structures, the selected dose was 1800 $\mu C / Cm^2$ (Figure 4.2b).

Samples were then ready for the deposition of TiO_2. Therefore, 30 nm thick TiO_2 was deposited via plasma enhanced ALD (FlexAl, Oxford Instruments, Abingdon, United Kingdom) at 130 °C and covered all of the sample surface including the nanopole-structures. The reason of using

plasma is compare to the thermal ALD the temperature is reduced, which is necessary for the stability of the resist (lower than 150 °C). In this case, an oxygen plasma was generated. For the production of TiO_2 layers, Tetrakis (dimethylamido) titanium (TDMAT) was used as the precursor.

For achieving a desired thickness of 30 nm, two samples were taken into consideration, and the deposition of different cycles of 501 and 688 cycles with the deposition rate of 0.599 angstroms/cycle were applied, and thickness of the samples were measured using ellipsometry. Three different regions of both substrates were measured and the mean value and standard deviation were determined (Table 4.1).

	Sample 1	Sample 2
Expected thickness d_1 [nm]	30 nm	40 nm
Measured thickness d_2 [nm]	27.52 nm ±0.34 nm	37.19 nm ±0.31 nm
Absolute error d = d_2- d_1 nm	-2.48 nm	-2.822 nm
Relative error |d/ d_2|	0.09	0.08
Relative error (%)	9.01	7.59

Table 4.1 The ellipsometry results of the thickness measurement of TiO_2 for two different Au substrates. The expected and the measured thickness are presented, with the absolute error, relative error and corresponding relative percentage error are shown.

As seen in Table 4.1 based on ellipsometry values, the standard deviations in both samples show that the homogeneity of the TiO_2 over the sample is high. The sample with the deposition of 501 cycles and thickness of 27.52 nm ±0.34 nm STD was selected for the further procedure of nanostraw fabrication.

Then, for structuring the TiO_2, an anisotropic etching process without usage of sacrificial layer and mask, was performed using plasma enhanced RIE. For that, gases used were CF_4 and O_2 with mass flow of 12 sccm (cm^3 / min) and 4 sccm (cm^3 / min), respectively. The RF power was 20 W with the ICP-RF of 400W and bias Voltage of 20 V, the pressure of 0.005 mbar for 38 sec at 0 °C (Table 4.2).

	RIE for TiO_2
Layer thickness[nm]	30
Process gases	CF_4/ O_2
Gas flow [slm]	12/4
Process time [s]	38
ICP power [W]	400
RF power [W]	20
Temperature [°C]	0
Bias Voltage [V]	20

Table 4.2 Process and parameter detail of the TiO_2 etching

After structuring the TiO_2 layer, the fabrication of nanostraws was finished. In the last step, the residual photoresist was removed by immersing into acetone and isopropanol for 15 min each, followed by rinsing in water, then treating with O_2 plasma (200 W, 300 sccm, 3min) to remove any chemical residues. Schematic fabrication flow of the designed nanostraws with multiple spacing and used doses on gold substrate is represented in Figure 4.2.

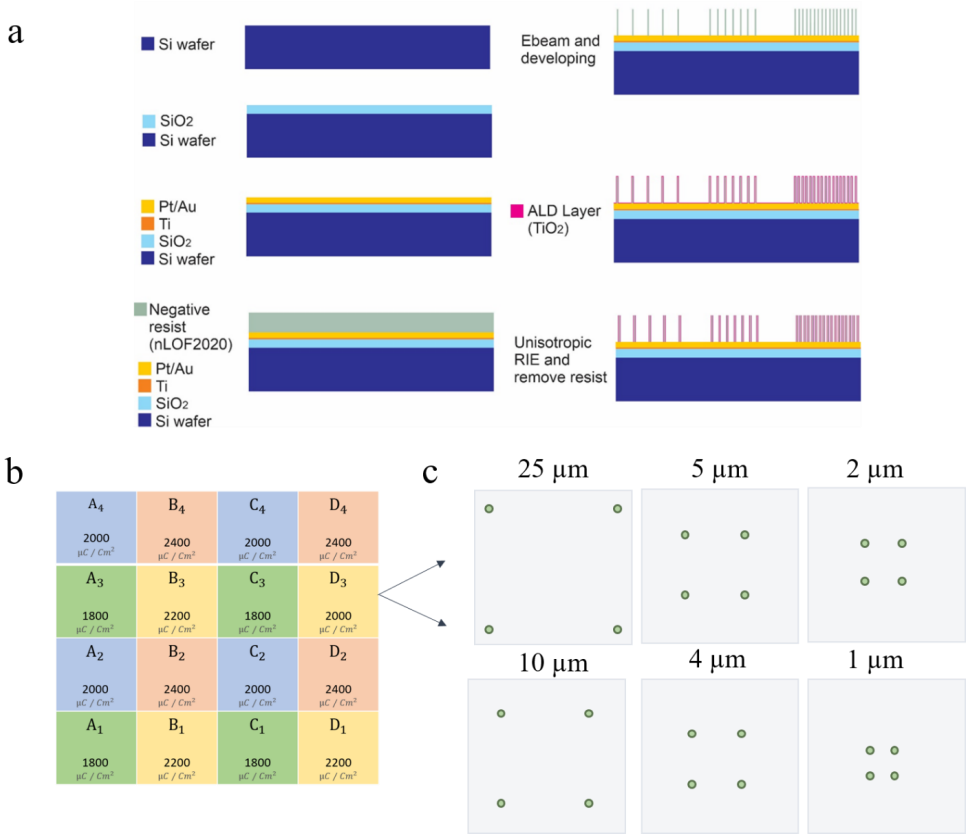

Figure 4.2 Fabrication flow and orientation of the nanostraw design on gold samples. a: Fabrication flow of nanostraw. The details of each step is included in the figure. b: The design of nanostraws with various doses in different region of each sample. The used doses (1800-2400 $\mu C / Cm^2$) are presented in the figure. c: Each box (A-D) consists of multiple nanostraws of 100 nm diameter with various center to center spacing (pitch) between each other. In this body of work 4 different pitches were designed. (1 μm, 2 μm, 4 μm, 5 μm, 10 μm and 25 μm).

4.2 Scanning electron microscopy (SEM) characterization

SEM was performed, for estimating the desired high aspect ratio nanostraws. Here, in Figure 4.3, the fabricated nanostraws with different pitches are shown. Al20though structures were exposed to various conditions in the fabrication processes, the SEM images confirm the stability and strong adhesion of nanostraws on the substrate. The diameter, height and spacing of the nanostraws were measured and the resulting values were, inner diameter of 100 nm, outer diameter of 165 ± 10 nm and the height of 2100 ± 121 nm (Figure 4.3 .d). In order to establish the optimum spacing between nanostraws when interfacing cell, nanostraws with multiple pitches were fabricated and further microscopic characterizations were performed. Figure 4.3 a, b and **c** represent the nanostraws with 1µm, 2µm and 4 µm pitches, respectively.

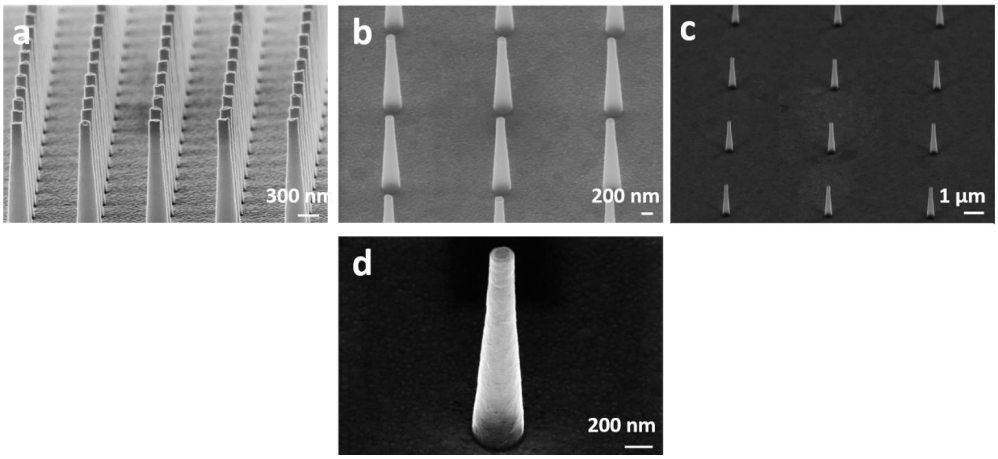

Figure 4.3 SEM images of various nanostraws on Au substrate. a: Arrays of NS with 1 µm pitch. b: Arrays of nanostraws with 2 µm pitch. c: Arrays of nanostraws with 4 µm pitch. d: Single nanostraw with 100 nm inner diameter and outer diameter of 164 nm at the tip, and the height of 2.4 µm.

4.3 Neuronal culture on 3D structure

For the viability assay, neurons were seeded on the NS substrates. Before seeding the cells, samples were coated with PLL, a positively charged polymer, in order to enhance the cell adhesion [128] [129]. For the preparation, 0.01 mg/ml of PLL diluted in HBSS solution is applied to the sample and incubated for 1 h. 500,000 cells were plated on a substrate and after 1 to 4 hours the medium was exchanged in order to remove the dead cells from the culture medium.

Figure 4.4 represents the viability assay of cortical neurons from two gold substrates containing nanostraws (blue square dot regions). For that, the samples at 3 DIV were stained for live and dead cells with Calcein-AM and ethidium homodimer-1 (details in method section 3.2.3) respectively, and fluorescence microscopy was performed. The experiment was performed on the substrate containing both nanostraws and Au with the aim of having a comparable condition for the ample preparations and neuronal cultures with the same density of the entire substrate, therefore more sufficient comparison for the viability assess. It is shown that the numbers of cells and specifically presence of network of neurons are more dominant on the region of nanostraws (blue square dots) compare to the Au regions.

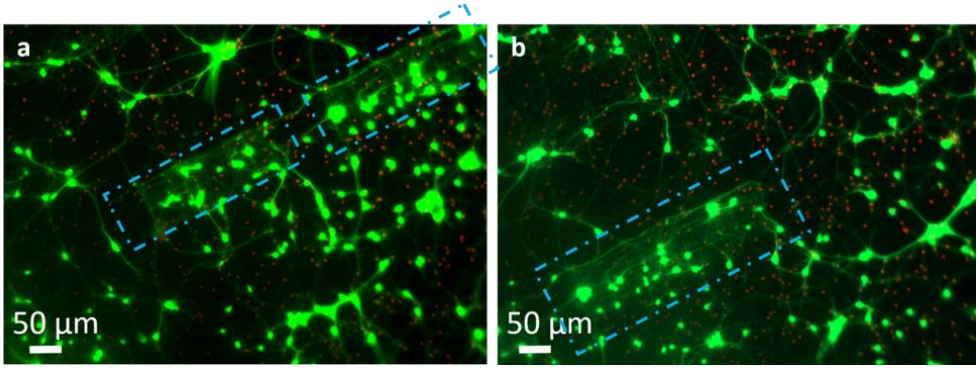

Figure 4.4 Viability assay of gold substrates containing nanostraws. The imaging is performed at DIV 3. Green stained (Calcein-AM), corresponds to living cells and the red dots representing dead cells. Blue square dots represent area containing nanostraws and the rest of the regions are Au substrates.

4.4 Actin and membrane staining in living cells

For further investigation regarding cell-nanostraw interface actin and membrane staining were performed by Frano Milos. For investigation of actin cytoskeleton perturbation at the presence of nanostraw, fluorescent F-actin marker, LifeAct-RFP (a 17-amino-acid peptide) [130]. In this regard, transfected cells (Detail in 3.2.4) were cultured on the substrate containing nanostraws with 2 µm spacing, after 4 to 8 DIV imaging was carried out on a confocal laser-scanning microscope. As seen in Figure 4.5, both samples represent accumulation of F-Actin at different regions of the cell (soma, dendrites) around the nanostraws and formation of actin rings (Figure 4.5**.** b(ii) white rings). It should be noted that no F-actin accumulation was observed on the flat Au substrate (Figure 4.5**.** b(i), blue box). Although this experiments were only performed 2 times and only with nanostraws with 2 µm spacing, however, it is a good indication of the tight engulfment between the neuronal cell membrane and nanostraws [131].

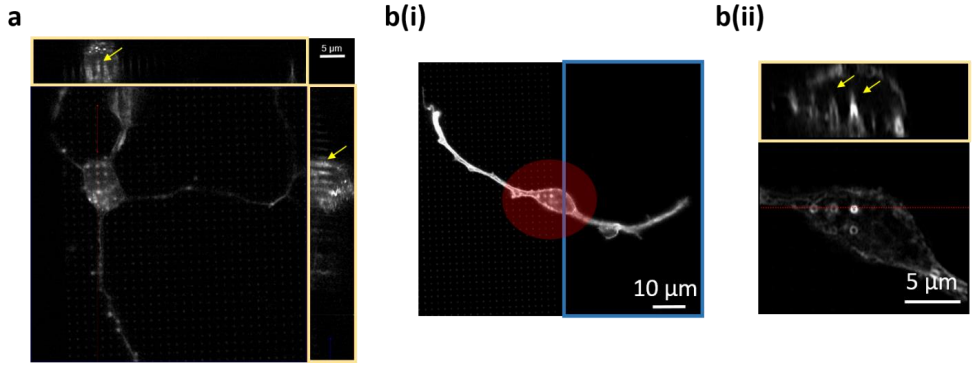

Figure 4.5 Two examples of neuronal actin staining on substrates containing nanostraw with 2 µm pitch. In both a&b, accumulation of F-actin and the formation of actin-rings around the nanostraws are observed (yellow arrows). Yellow boxes (a&b (ii)) are the orthogonal projections of 30, 0.22 µm slices at the position marked by red dots. b(ii) is the zoom-in of red circle in b(i) with an orthogonal projection. Blue box in b(i) is the representation of cell on Au substrate which no actin ring is observed.

Moreover, for the investigation of the interaction between cell membrane and nanostraws, we performed the membrane-staining experiment. For this purpose, neurons were cultured on nanostraw samples with 1µm, 2µm, 4µm and 5µm spacing. Then neurons were incubated in DiI solution at DIV 4-8 (detail in Chapter 3.2.4) and confocal microscopy was performed.

As seen in Figure 4.6.a, the cell membrane is tightly engulfed with the top of the nanostraws. However it is observed that the cell membrane is failed to bend at the bottom of the nanostraws and the gold substrate. The possible reason can be due to the small spacing between the nanostraws. In Figure 4.6.c and d, however, the attachment of the cell to the surface of the Au substrate were observed while the engulfment with nanostraws could not be perceived. On the other hand, in Figure 4.6.b, when the nanostraws were located with 2 µm pitches, the neuron is not only well attached to the surface of the substrate, but also a strong fluorescence signal at the end of the nanostraws is observed which is due to the membrane curvature. In previous studies it is reported that the membrane curvature phenomena is an indication of a close contact between the nanostraws and plasma membrane [131] [119]. However complete penetration could not be proven due to the autofluorescence of the nanostraws, but a close contact between the cell and nanostraws were affirmed.

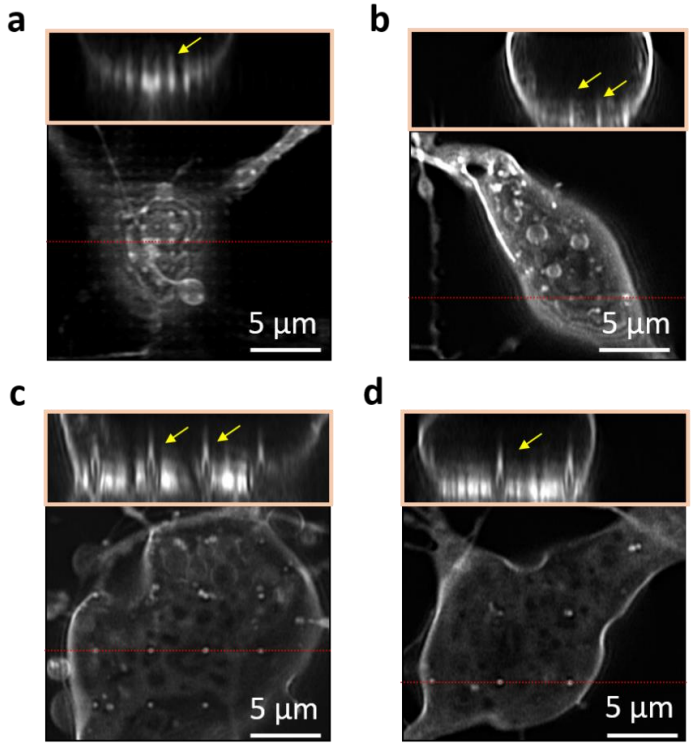

Figure 4.6 Membrane staining on the nanostraw sample with different spacing, containing neuron at DIV 4-8. The red dashed lines represent the location of the orthogonal projections of 30, 0.22 µm slices of a DiI-stained neuron growing on nanostraws. Yellow arrows represent the nanostraws pushing the membrane upward, representing tight engulfment. a, b, c, and d represent the nanostraws with 1 µm, 2µm, 4 µm, 5 µm pitch, respectively.

4.5 Fixation and electron microscopy

Furthermore, due to the limitation of the fluorescence microscopy resolution, additional investigation was performed in order to visualize the interface and the coupling between the cell and the nanostraws with nm resolution.

Here we used two different methods for the fixation and sample preparation. Critical point drying is explained first. Afterwards, staining and resin embedding is demonstrated, and results compared.

4.5.1 Critical point drying (CPD)

At DIV3 live-dead staining was performed on neurons in cell culture medium. After optical imaging, cells were fixed with 2% (Glutaraldehyde) GA in PBS and dried with CPD technique (Figure 4.7 and Figure 4.8). Spacing of nanostraws on the Au substrate is vary from 1 µm to 5 µm for investigating differences in cell behavior. In Figure 4.7.a, the overview of strong guides of neurites outgrowth at the area of nanostraws. Figure 4.7.b and Figure 4.7.c, show the cell body attachment to the nanostraws with 2µm and 5 µm spacing, respectively. No significant difference in the cell attachment in these two pitches can be recognized. However, in Figure 4.7.b and Figure 4.7.c, nanostraws were pulled out from the gold substrate by dendrites which might be due to the fixation or CPD procedures. Figure 4.7.e-g indicates that the neurites well conformed to the nanostraws [132]. As seen in Figure 4.8, on the nanostraw sample with 1 µm pitch, a neuron positions on top of the structures, which can be due to spacing and failure of bending around the structures. In order to achieve the tight engulfment between the neuronal cells and the nanostraws, based on all these observation we selected 2 µm pitch between nanostraws.

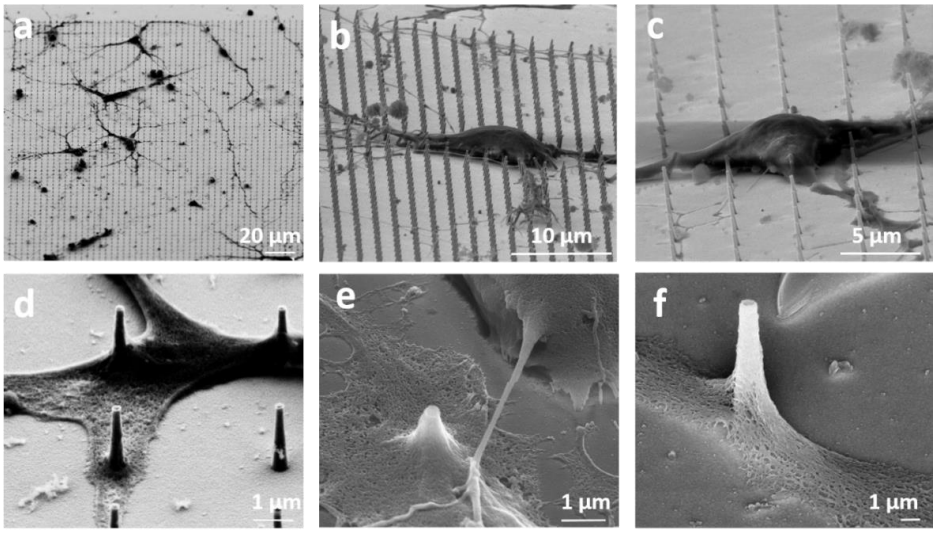

Figure 4.7 SEM of the CPD method on neurons on nanostraw substrates with different pitches. a: Overview of the neuronal growth on the arrays of nanostraws and well-established neurites outgrowth. b: Engulfment of soma to the nanostraw with 2 µm pitch. c: Engulfment of soma to the nanostraws with 5 µm pitch. In both b & c the nanostraws were pulled out by neurites which is the defect of sample preparation. d: Neurites conform the nanostraws with 4 µm spacing. e & f: zoom-in of the neurites attachment to the nanostraws.

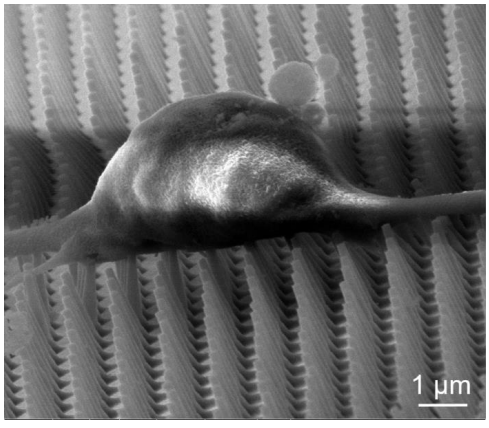

Figure 4.8 SEM image of fixed neuron on nanostraws with 1 µm spacing. As seen due to the spacing between nanostraws, cell fails to bend and is located on top of the structures.

However, CPD technique is restricted due to shrinkage artefact during the preparation process and causing damages to nanostraws, cells (body, neurites) and their connections. Although CPD process is performing at the point of co-existence of liquid and gas phase, however one possible reason of shrinking affects can be due to the liquid-gas transition which leads to surface tension (as seen in Figure 4.7.b and c), and the reduction in physiological volume up to 20% [121] [122]. Moreover, because of porous and sponge-like morphology of the cell (as seen in Figure 4.7.d-f sponges-like structure) created by this method, the intracellular membrane and other cell compartments are not evident, therefore the investigation of actual interface of the cell and nanostructures is not feasible via CPD technique [23].

4.5.2 Staining and resin embedding

In contrast, the resin embedding method preserves the cell volume [41] with minimal structural and morphological damage to the cells and the structures (Figure 4.9). This is due to the replacement of the water components in the cells with infiltrated resin. Additionally, there is significant improvement in cross sectioning of the cell and its components, even revealing the intracellular cell membrane via FIB. This process was done by Elke Brauweiler-Reuters and Elmar Neumann.

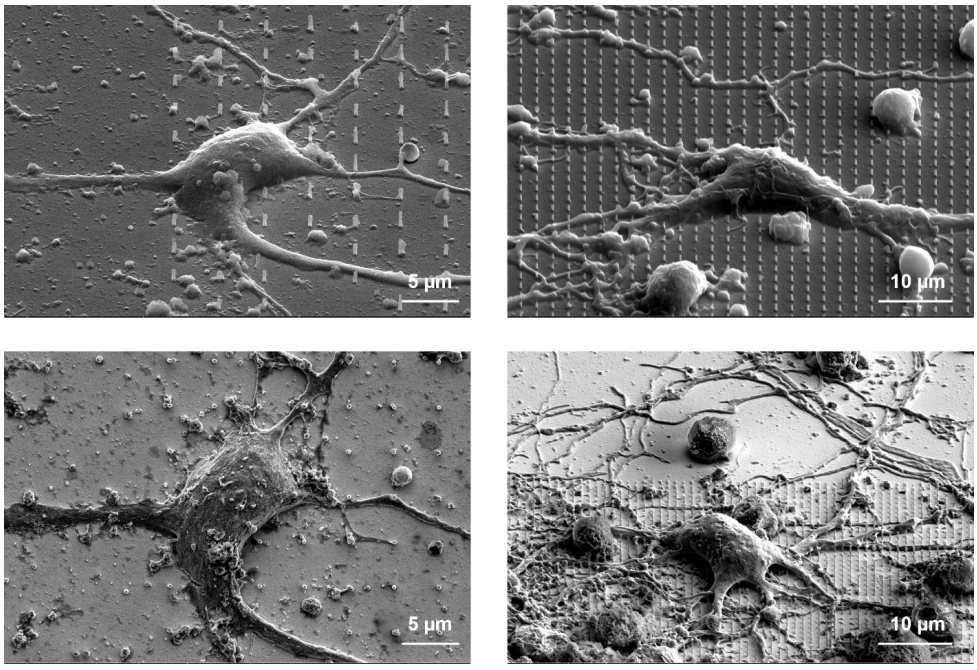

Figure 4.9 SEM images of few examples fixed neurons on nanostraw structures, treated with resin embedding and staining method. As seen compare to CPD technique less shrinkage is evident, and the sponges-like neurons are not visualized.

In Figure 4.9, the high resolution cross sectioning and SEM micrographs of the fixed cells (at div 3) via staining and resin embedding methods are shown. Substrates with different pitches of nanostraws were utilized and cell behavior were compared according to pitch. Unless CPD technique (Figure 4.7 and Figure 4.8), there are less damages appeared on the cells and structures, such as neurite cracked, broken structures and surface tensions, and the interior cell components are perceptible. The cross sectioned of these samples treated with resin embedding techniques represent that the nanostraws were tightly engulfed the cell membrane, also the deformation of the nucleus was observed (Figure 4.10). Nevertheless, due to the few number of performed experiments and lack of statistical investigations, also the poor resolution of the electron microscope compare to the cell membrane thickness (~ 6 nm) the complete penetration could not be verified.

Besides, it should be mentioned that, although in Figure 4.10.a, nanostraws with 1 µm pitch confirmed the tight engulfment of the cell and membrane wrapped around the structures, however in some other experiments that incident was not observed (Figure 4.11). The possible reason could be that 1µm pitch between the nanostraws, sometimes creates a surface that the cell (with the soma

size of 5-20 µm) recognizes as flat resulting in reduced cell penetration and engulfment. It should be mention that, in this set of experiment the cell contains sponges like structure and also the inner side of the cell is not visible. This might be due to the lack of using uranyl in the process or another reason might be failure in handling which is a common challenge in this process.

Although resin embedding method has shown a significant improvement in the investigation of the cell- 3D structures interface, and presenting the cell components clearly, it is still suffer from several drawbacks like, dangerous technique, expensive, and because of the fixation with GA and further processes, changes in cells or/and structures conformations is still a question [133].

For further electrophysiological investigation and the recording of the neuronal activities with the nanoelectrodes devices, based on the micrographs in Figure 4.10 and Figure 4.11, and also the previous experiments (Chapter 4.4) it could be determined that the optimal pitches of nanostraws regarding cell membrane curvature phenomena, could attributed to 2 µm, 4 µm and 5 µm. However, due to the electrode size (6 µm or 10 µm), we selected 2 µm spacing as the optimal pitches of nanostraws.

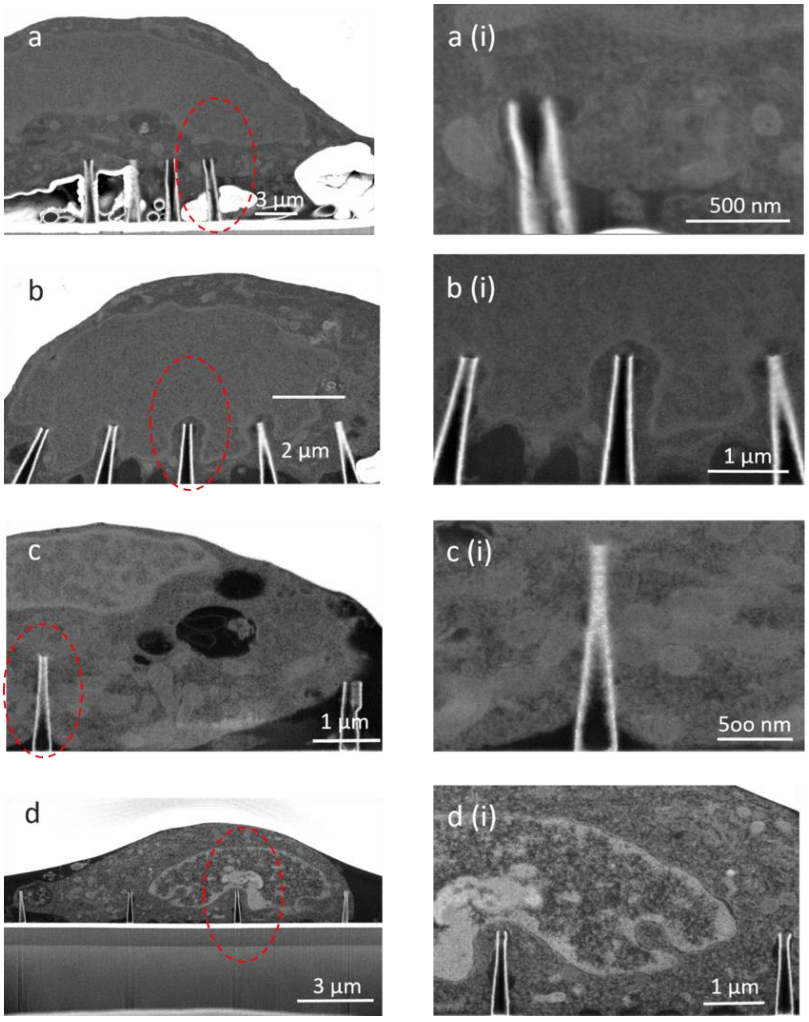

Figure 4.10 FIB cut and SEM of the fixed cells (at DIV 3) on nanostraw substrates with different pitches, treated with staining and resin embedding. Nanostraws with (1 µm. 2 µm, 4 µm and 5 µm pitch, in a, b, c and d, respectively) and corresponding, a(i), b(i), c(i) and d(i) are the zoom in (from red dot regions) of each. The fixed cells on all cases are tightly engulfing the nanostraws. And the nucleus is being deformed at the tip of the nanostraws.

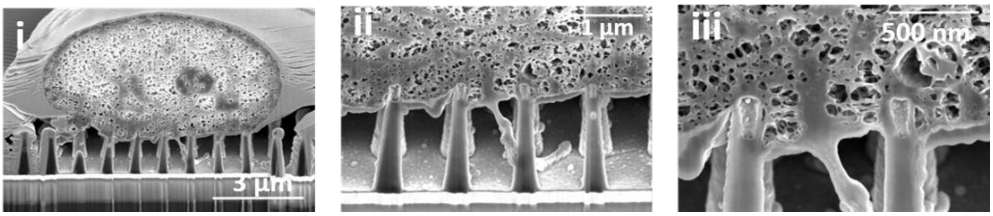

Figure 4.11 SEM image of stained neuron on nanostraws with 1 µm pitch with three different zooms. This experiment was performed uranyless. The cell fails to bend between the nanostraws as much because they are too close together and cell is placed on top of the structures. Therefore tight engulfment is not visualized.

4.6 Conclusion

Nanostraws were fabricated on planar gold substrate. Using the fabrication process developed in this thesis, straws of dimensions, 100nm inner diameter, 165 nm outer diameter, and 2100 nm in height were fabricated with low variation (6% outer diameter, 5% height).
Neuronal culture on the straws separated by different pitches showed that neurons distributed on the whole substrate, and also the presence of neuronal networks are more dominant at the area of nanostraws representing the biocompatibility of nanostraws. More investigation regarding cell-nanostraw interface using actin and membrane staining confirmed the formation of actin rings and membrane curvature with strong fluorescence signals at the end of nanostraws, respectively, are the indication of tight contact between the cells and nanostraws.
A closer investigation of the interface using cross sectioning and electron microscopy showed that straws were tightly engulfed by the cell membrane. Engulfment led to specific structure of the cytoskeleton and plasma membrane deformation on the area on nanostraws, as well as deformation of intracellular structures such as the nucleus. These were most pronounced in substrates with pitch 2-5 µm. In contrast, substrates with only 1µm pitch showed little or no engulfment. At such a small pitch, the neurons are placed on the structures without bending, therefore results in a signal lose for further electrophysiological applications.
Since good MEA recording of neuronal APs will require high SNR while maintaining the small aperture for the purpose of single cell resolution, the nanostraws of pitch 2 µm was selected as candidates for electrode modification. These structures are expected to engulf tightly to the neuronal cells which will improve sealing resistance and therefore higher SNR in electrophysiological recordings. The production procedure and electrophysiological investigations will be discussed in the next chapter.

Chapter 5. Nanostraws on nanocavity MEAs

In chapter 4, it is proved by light and electron microscopy that cellular tight engulfment of the nanostraws occurred due to the size and aspect ratio of the nanostraw. In order to study the electrical activity of the cells, multielectrode arrays (MEAs) are used and nanostraw fabrication which is described in chapter 3 has to be adapted to the nanocavity-MEAs. In this chapter, the fabrication and characterization of the nanostraws on nanocavity-MEAs will be discussed. Afterward, the electrical activities of the neuronal cells will be recorded and evaluated in detail.

(This chapter is in part reproduced from the manuscript, High-aspect-ratio nanoelectrodes enable long-term recordings of neuronal signals with subthreshold resolution, Pegah Shokoohimehr, Bogdana Cepkenovic, Frano Milos, Justus Bednár, Hossein Hassani, Vanessa Maybeck, Andreas Offenhäusser which is submitted in Nov.2021)

The fundamental techniques for the production of microelectrode arrays is microfabrication. All the fabrication processes are done similar to chapter 4, in the cleanroom (ISO-1) of the Helmholtz Nanoelectronic Facility (HNF). First of all, the design and fabrication of microelectrode arrays are described and then the nanostraws transfer and implementation to the microelectrodes will be discussed.

5.1 MEAs fabrication

MEAs were fabricated on 4 inch n-doped silicon wafer (<100> orientation; Siegert Wafer GmbH, Aachen, Germany) covered with a 1 µm silicon dioxide layer. A total number of nine chips (microelectrode arrays) were produced on one wafer. Each MEAs with a size of 1x1 square inch with a circular sensor area in the center with 64 electrodes (8x8 grids with a pitch of 200 µm) were designed. These electrodes were connected to contact pads through metal feedlines. Two of these electrodes with bigger size of 140 µm diameter served as reference electrodes. Insulating layer was deposited onto the metal feedlines and it was opened on the electrode areas and contact pads. The electrode area openings had a diameter of 6 µm and 10 µm, respectively.
The 300 nm thick metallization stack was fabricated for the production of MEA which consists of titanium (20nm), platinum or gold (200nm) and chromium (80nm). Titanium layer served as an adhesion layer between the silicon dioxide and the conductive layer (Pt/Au). Chromium layer was used, first of all as an adhesion layer between the metal layer and the passivation layer, furthermore, to serve as a sacrificial layer for the further production of nanocavity MEAs. Metal layer was deposited via electron beam evaporation. For isolating the feedlines, the stack of silicon

oxide (200nm thickness) and silicon nitride (100nm thickness) was utilized via plasma enhanced chemical vapor deposition (PECVD). In this work stack of $SiO_2/Si_3N_4/SiO_2/Si_3N_4/SiO_2$ (ONONO layer), with a total thickness of 800nm, were employed. For the opening of the electrode area (6 or 10 μm) and contact pads, reactive ion etch (RIE) was used.

The nanocavity MEAs fabrication is investigated in detail at the previous studies [56] and it is not the in the actual focus of this work, but mostly using the concept of nanocavity. The detailed fabrication procedure of MEA device is described in detail in Appendix 1.

After etching the passivation layer, prior to fabrication of nanostraws on the electrode opening (Pt/Au), Cr layer should be removed. Therefore, we performed anisotropic etching process which was established in body of this work and will be presented in detail.

5.2 Chromium physical etch

In order to etch the Cr layer on the electrode opening, RIE was performed. In this step, the photoresist (positive resist AZ5214 E) which has been used for the etching of ONONO layer remained on the substrate serving as a sacrificial layer. The parameters for etching 80 nm of Cr is shown in table 3. In the etching chamber, gasses of Chlorine (Cl_2; 30 sccm) and oxygen (O_2; 20 sccm) were utilized. The RF power was 25 W, the ICP power was 1000 W, and the bias voltage during the process was 75 V, and the process was performed at 20 °C with pressure of 0.0015 mbar. In order to evaluate the sufficient parameters in a wafer scale, we used two samples and performed the RIE etching with the same parameters, with two different times of 60 s and 90 s (Table **5.1**).

	RIE for Cr
Layer thickness[nm]	80
Process gases	Cl_2/O_2
Gas flow [sccm]	30/20
Process time [s]	60/90
RF power [W]	25
ICP power [W]	1000
Bias voltage [V]	75

Table 5.1. Detail parameters for etching 80 nm of Cr via RIE.

The samples were then characterized with EDX for the final conclusion. As seen (Figure 5.1), in both samples there is no Cr residues on the electrode openings. No effects on the beneath electrode (Au/Pt) was also observed when the etching time was longer. Thus, we set 90 sec of etching time for the 4 inch wafer in order to assure the complete and homogenous etching of Cr layer.

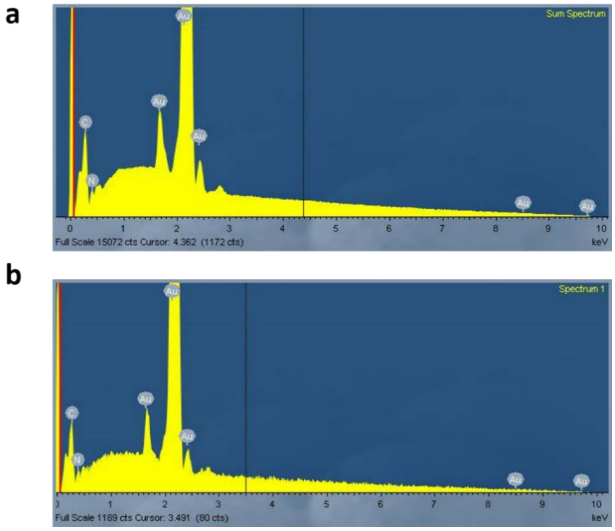

Figure 5.1 EDX analysis after etching 80 nm of Cr on the electrode opening area, in a wafer scale. a: EDX after 60 sec etching. b: EDX after 90 sec etching. It is observed that no Cr residues are on the electrode opening.

After all the etching process, the wafer was cut into 9 pieces of MEA devices with the size of 1x1 inches each (DAD 3350 dicing saw, DISCO Corporation, Tokyo, Japan). The photoresist remained on the wafer as a protection during the sawing process.
Afterwards, the resist was removed from the sample by immersing into acetone followed by isopropanol, 20 min each. In the end samples are cleaned with deionized water (DI-water) and dried carefully in a stream of nitrogen. The fabrication of MEA was completed.

In following the process of nanostraw-nanocavity MEA fabrication and multiple characterizations will be described.

5.3 Nanostraw fabrication on MEAs

In order to fabricate the nanostraws on microelectrode arrays, nanostraws first were made on Au surface which is described in detail in chapter 4. The reason for that was the ease of characterization in each step and further biocompatibility test and cell structure interface investigation. Since the material of the electrode area of MEAs were gold or platinum, Au substrate was used to have the similar substrate with the similar morphology and also chemical or physical quality. All the steps in the process and parameters were established in the body of this work. The microelectrode were also made exclusively as it is already explained in 5.1 and 5.2 (detail in Appendix 1). Therefore, the fabrication of nanostraws had to be implemented on our MEAs system. In this regard, all the process steps from chapter 4 for fabrication of Nanostraw on Au were repeated (Figure 5.3).

The fabrication of Nanostraw- MEA was performed (similar to chapter 4). Firstly, samples were placed on a hot plate for dehydration with the temperature of 150 °C for 5-10 min. Then, negative resist (nLOF 2020) was spin coated on each MEA chip individually, with spin rate of 4000 rpm, open lid for 35 second, then was directly placed on hot plate with 110 °C for 1 min.

For the next step, samples were taken to electron beam lithography. Here, the selected dose was 2400 $\mu C / Cm^2$ due to the sufficient height (2.4 µm), diameter (inner diameter 100 nm, outer diameter 160 nm) and robustness of the structures. The details of the E-beam lithography was mentioned in chapter 4 and it is avoided to describe here over again.

The mask has been used in this step (Figure 5.2), was implemented for the MEA chip, and in this case, alignment was required in order to keep the structures on the electrode aperture. Nanostraws with 2 µm spacing were designed on the center of each electrode. For electrode with diameter of 10 µm, 9 nanostraws were produced, while for the other electrode with 6 µm diameter, 5 nanostraws were fabricated.

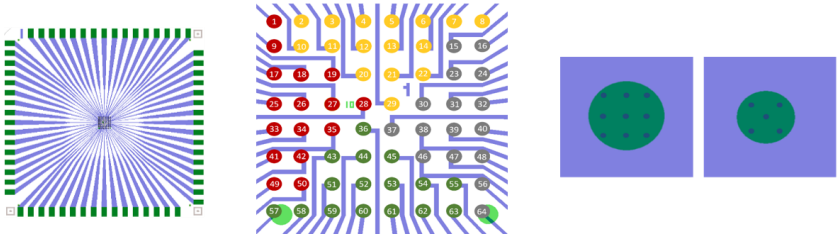

Figure 5.2 Schematic design of nanostraws on MEA device.

Next, post exposure was performed as samples were placed on a hot plate at 110 °C for 1min, then immersed into the MIF326 solution for 50 second, followed by washing with DI-water in order to stop the developing process and clean the sample. In this step, the structured nLOF resist in a form of nanopoles on the center of each electrodes were produced. The height, diameter and the shape of the structures were critical in this step, therefore samples must be observed with an electron microscope (SEM) before continuing to a next step.

Similar to the chapter 4, as a next step, the deposition of 30 nm of TiO_2 via plasma inhanced ALD was performed. TiO_2 was covered on entire surface of the MEA and coverd the nanopoles inside the electrode openings. Then, an anisotropic etch of TiO_2 via plasma reactive ion etching was performed which leads to an etching the undesired area of TiO_2 on the surface without using a protection mask. For that, tetrafluoromethane (CF_4; 12 sccm) and oxygen (O_2; 4 sccm) were the gasses used in the process. The etching time for each MEA chip was 38 sec with the RF power and ICP-RF of 20 W and 400 W repectively. The etching process was performed at 0 °C with the pressure of 0.005 mbar (Table 5.2).

	TiO_2 etch
Layer thickness[nm]	30
Process gases	CF_4/O_2
Gas flow [sccm]	12/4
Process time [s]	38
RF power [W]	20
ICP power [W]	400
Bias voltage [V]	20

Table 5.2. Detail parameters for etching 80 nm of TiO_2 via RIE.

After the anisotripc etch of TiO_2, the residual resist was cleaned from the sample by immersing into acetone and subsequently isopropanol and water for 10 to 20 min each.

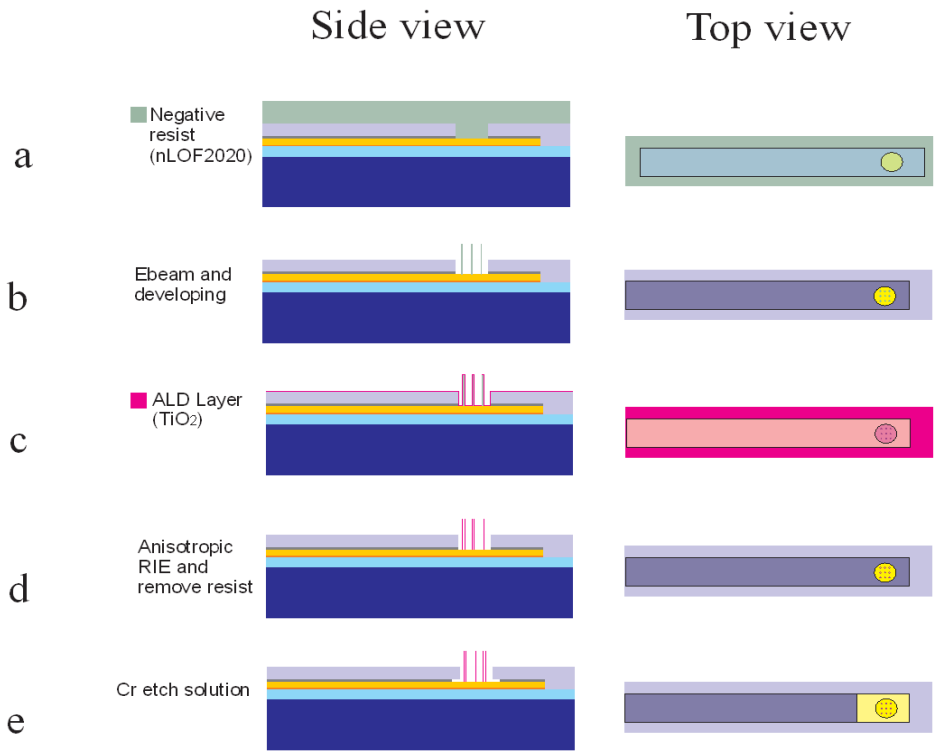

Figure 5.3 Schematic of fabrication flow for the production of nanostraws on MEA, and the introduction of nanocavity. a: Spin coating 2.5 µm of negative resist (nLOF2020) on MEA device. b: Electron beam lithography and development results in nanopoles in the center of electrode openings. c: Thin layer (30 nm) of TiO_2 deposited all over the substrate via PEALD. d: Anisotropic etching of TiO_2 using RIE. e: Applying Cr etchant solution and formation of nanocavity-MEAs.

Moreover, for the introduction of nanocavity, chromium etchant solution was placed on the center of each MEA. Isotropic etching creates the cavity in each direction from all the electrode openings on MEAs. For that, 100 µl of Cr etch solution No.1 from MicroChemicals GmbH (Ulm, Germany) was places on the center of each MEAs. The solution was a combination of perchloric acid ($HClO_4$; 4.25 %), ceric ammonium nitrate($(NH_4)_2[Ce(NO_3)_6]$; 10.9 %) and water (H_2O; 84.85 %). Ceric ammonium nitrate is the main part of the etching process, while the perchloric acid is the stabilizer. The etchant does not attach noble metal such as gold or platinum. Therefore, it is the best candidates for etching the chromium layer.

$$Ce\ (NH_4)_2(NO_3)_6 + Cr \rightarrow Cr\ (NO_3)_3 + 3\ Ce(NH_4)_2(NO_3)_5$$

Figure 5.4, illustrates the nanostraws on microelectrode after chromium etch solution.

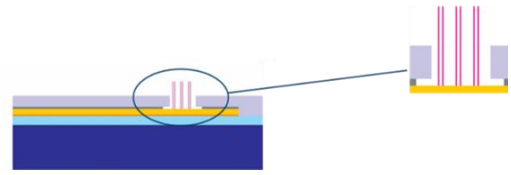

Figure 5.4 Schematic of Nanostraw- nanocavity MEA

For the characterization of our device, various techniques were performed. Microscopy techniques were performed to investigate the quality of the nanostraws- nanocavity MEAs.

5.4 Light and electron microscopy characterization

Similar to the previous chapter (chapter 4), SEM (Zeiss Gemini 1550 VP field emission SEM, GmbH, Oberkochen, Germany) was performed using both secondary and in-lens detectors, for assessing the quality of the fabricated nanostraw (diameter, height and shape).

Figure 5.5, represents the SEM micrograph of the fabricated nanostraws on MEAs. As seen, in spite of various critical fabrication steps, strong bound of the nanostraws on the electrode surface were visualized. Closed view of the nanostraws were presenting the slight conical shape resulted from E-beam exposure dose, which could improve the seal resistance when interfacing neurons as it was reported previously [31] [47]. Since the fabrication process in all steps were controllable, low variations in height and the geometry of the nanostraws were visualized (with less than 0.3% variations). In this work, the height, inner and outer diameter were, 2.4 µm, 100 nm and 160 nm, respectively. A total 18 different regions of the device were taken into account with the average height of 2.44 µm ± 7 nm STD.

Figure 5.6 represents the nanocavity-MEAs after exposing 10 min Cr etching solution. Light yellow areas are the regions of nanocavity and as seen, the etching process in most of the electrodes were performed homogenous.

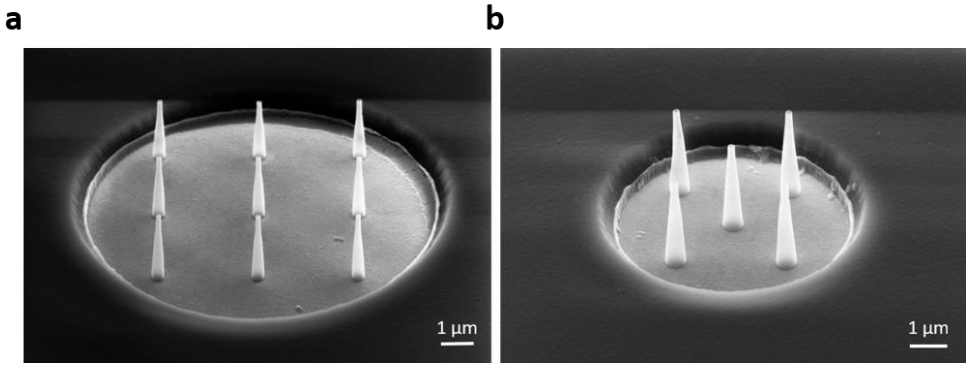

Figure 5.5 SEM micrograph of fabricated nanostraws on MEAs with 2 µm pitch between each nanostraw. a: Representation of 9 nanostraws on the electrode with 10 µm diameter. b: 5 nanostraws on the electrode with 6 µm diameter.

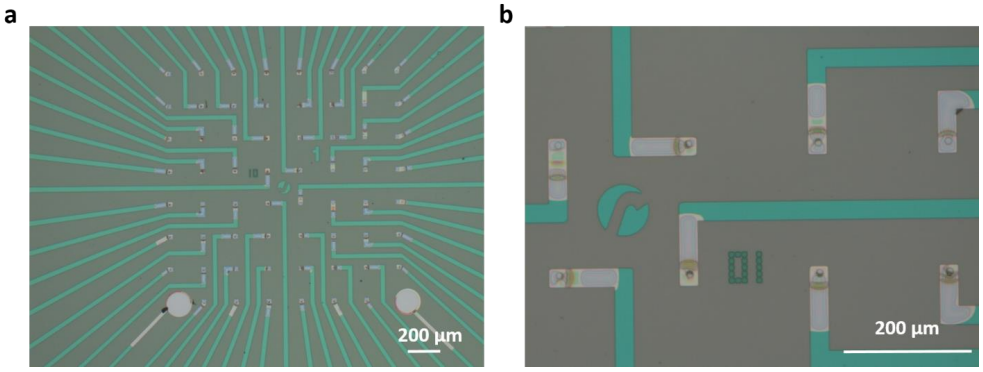

Figure 5.6 Light micrograph of nanostraw-nanocavity-MEAs after 10 minutes of Cr etch. a: Representation of 64 electrodes with 10 µm diameter. b: Zoom in of (a), the light yellow area are the cavities under the electrode openings.

After microscopy characterization of the device, for evaluation of the electrical performance of the device, electrochemical impedance measurement was performed.

5.5 Impedance spectroscopy

In order to characterize the electric performance of NS-NC-MEAs, electrochemical impedance measurements were performed. Impedance measurement defines the resistance of the electrode when current flow through it, and in general describes the electrode properties in case of an electric charge. The measurement was performed over the spectrum of frequency and the impedance of the device was defined at 1 kHz frequency, and due to the electrochemical double layer formed by a water molecule and ions, the capacitance of the electrode was produced.

In order to characterize the NS-NC-MEAs electrical performance, four different conditions were taken into account. For consistency of the measurements and comparisons, in all 4 conditions electrode material was platinum with the diameter of 10 µm and passivated with ONONO layer.

At first, the measurements were performed for the planar MEAs. Total number of 17 electrodes from two different devices were measured and the mean impedance and standard deviation value at 1 kHz were evaluated (|Z|= 763.9 ± 81.2 kΩ) (Figure 5.7).

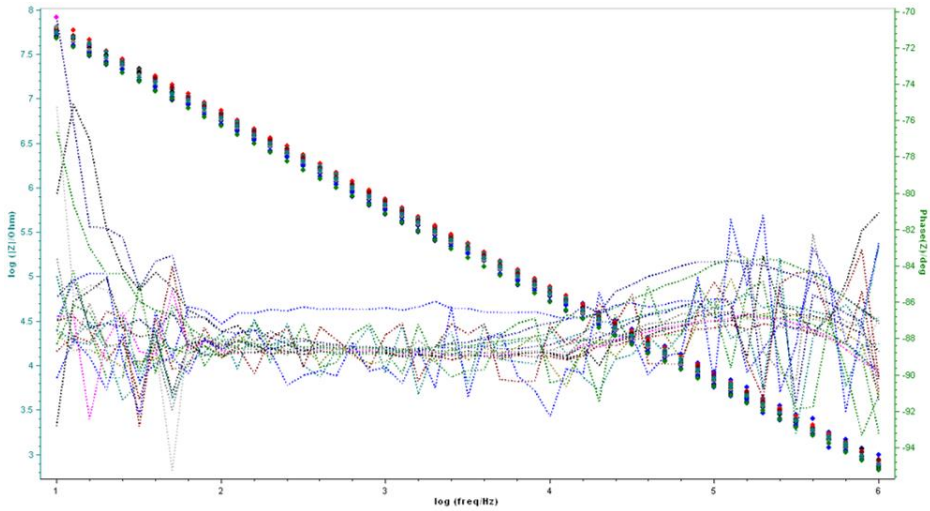

Figure 5.7 Impedance measurement of 17 electrodes from MEAs. The mean impedance and standard deviation value at 1 kHz were evaluated (|Z|= 763.9 ± 81.2 kΩ).

Second measurement was performed after the introduction of nanocavity. For that drop of Cr etchant solution was applied on the center of electrode areas for 10 min, and the measurement of the device was carried out after cleaning with ultrapure water. Then, 59 electrodes were measured and as expected from previous studies [56] [55] [58], dramatic decrease of the electrode impedance was observed (|Z|= 387.9 ± 50.7 kΩ) (Figure 5.8).

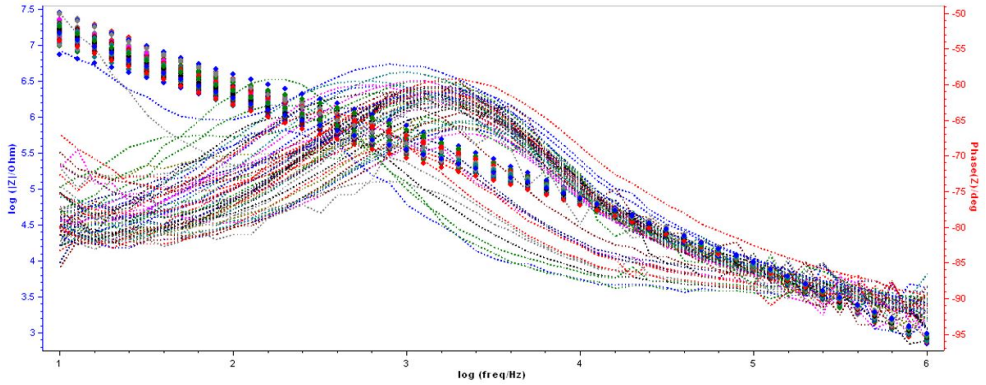

Figure 5.8 Impedance measurement of 59 electrodes from NC-MEAs. The mean impedance and standard deviation value at 1 kHz were evaluated (|Z|= 387.9 ± 50.7 kΩ).

For the evaluation of the NS presence on the device, two more experiments were carried out. Therefore, impedance was measured for the MEAs containing NS. The mean impedance of 25 electrodes was |Z|= 764.9 ± 89.5 kΩ, which compare to planar MEA, no explicit difference was observed (Figure 5.9).

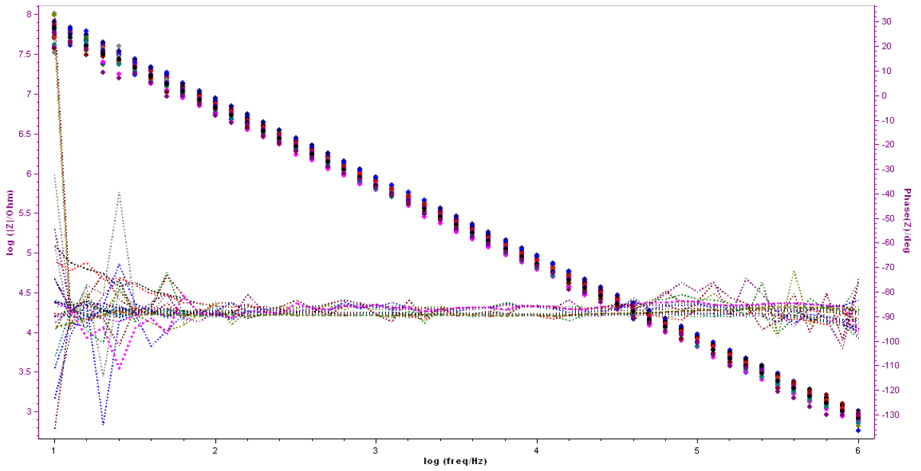

Figure 5.9 Impedance measurement of 25 electrodes from NS-MEAs. The mean impedance and standard deviation value at 1 kHz were evaluated (|Z|= 764.9 ± 89.5 kΩ).

Afterwards, similar to the previous measurement, 10 min of Cr etchant solution was applied. After the measurement of 53 electrodes, dropped of the impedance to |Z|= 323.46 ± 73.6 kΩ was perceived (Figure 5.10).

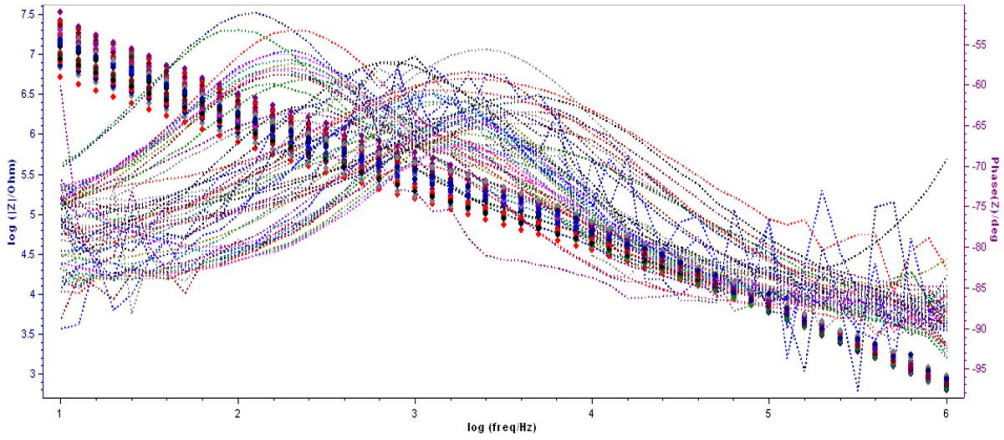

Figure 5.10 Impedance measurement for 35 electrodes from NS-NC-MEAs. The mean impedance and standard deviation value at 1 kHz were evaluated (|Z|= 323.46 ± 73.6 kΩ).

The resulted values were compared and as expected the introduction of nanocavity on MEAs leads to a drastic reduction of impedance, while maintaining the origin of electrode diameter. While the presence of NS on the MEA device, has no effect in the impedance values (Table 5.3).

Diameter 10 µm	MEAs	Nanocavity MEAs
Planar	763.9 ± 81.2 kΩ	387.90 ± 50.7 kΩ
Nanostraw	764.9 ± 89.5 kΩ	323.46 ± 73.6 kΩ

Table 5.3 The mean value of the electrochemical impedance measurements at 1 kHz for four different devices with corresponding standard deviations are represented. The impedance value of planar-MEAs (n: 17) and nanostraw-MEAs (n:25), confirm no impact of nanostraws on the electrode impedance. However, the impedance values for both nanocavity-MEAs and Nanostraw-nanocavity MEAs, were halved the impedance value of the MEAs.

After analysis the electrical properties of the NS-NC-MEAs, further investigations regarding electrical activity of neurons when interfacing NS-NC-MEAs were carried out. Hence, after sample preparations and coating, cortical neurons were cultured on chips, viability assays and subsequently electrophysiological recordings were accomplished.

5.6 Neuronal culture

Viability assay of the nanostraw-nanocavity MEAs were performed via life-dead staining, similar to the previous chapter (chapter 4).

As before, prior to cell seeding, PLL coating was performed to improve the cell adhesion (with the same concentration 0.01 mg/ml of PLL in HBSS solution). In each sample 0.5-1 ml of the prepared solution was applied and incubated for 1 hour at room temperature, followed by rinsing in HBSS solution. The total number of 200,000 neurons were seeded on the substrate, and after 1 to 4 hours of incubation, the cell media was exchanged. Half of the cultural medium changed every 3-4 days (Figure 5.11).

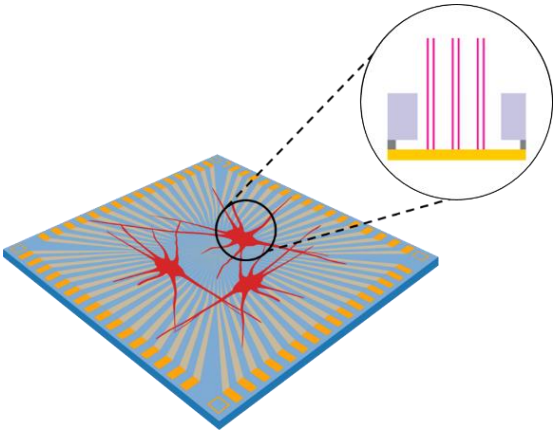

Figure 5.11 Schematic of Neuronal growth on nanostraws- nanocavity MEAs design

5.7 Life-dead staining and fluorescence microscopy

The staining and imaging for the NS-NC-MEAs were employed in older days *in vitro* (14-24 DIV), mostly after the electrophysiological recordings. After 14-24 DIVs, live and dead cells were stained by labeling dyes (Calcein-AM and ethidium homodimer-1 respectively), and visualized by fluorescent filters, according to the wavelength of the dyes (green and red, respectively). Similar to the previous chapter (4), fluorescence microscopy was performed via Apotome (Axio Imager Z1, Oberkochen, Germany, with 10x and 20x objectives) and the image processing was performed with ZEN and ImageJ.

As seen, Figure 5.12 shows that the number of the live neurons is much higher compare to the dead cells. It also displays creation of networks on the entire substrates [contains: nanostraw (TiO_2), electrode area (Pt/Au) and passivation (SiO_2)] which also represents the biocompatibility of our device even after 19 days in culture.

Moreover, for the investigation of device performance, the number of living cells (n: 37) on the center or near 62 electrode openings (reference electrodes were excluded) were counted, and these numbers were compared with the active channels which were recorded by the NS-NC-MEAs and will be described later in this chapter.

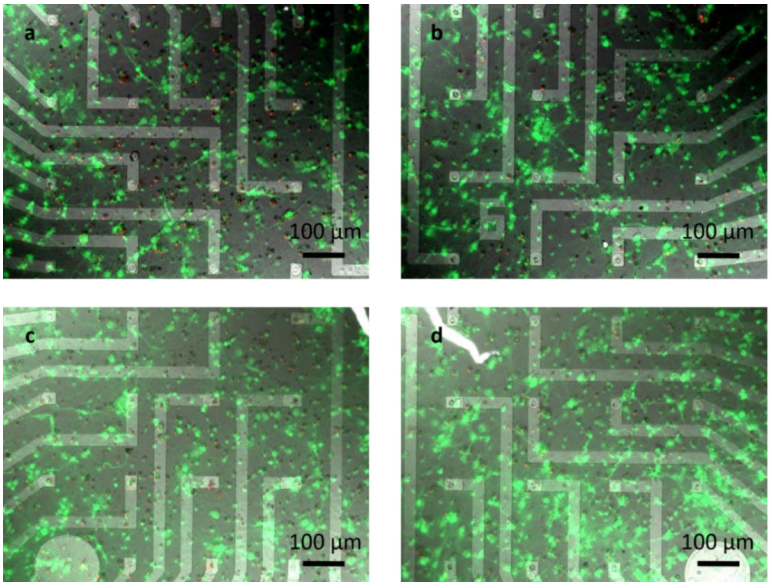

Figure 5.12 Viability assay of neuronal cultures on Ns-nanocavity MEAs in 19DIV. Electrode diameter: 6µm- Nanocavity. Out of 62 electrode openings 37 channels contain cells on/near-by.

For high resolution imaging and also investigation of the interface between the neuron and NS-NC-MEAs, FIB cut and SEM were performed.

5.8 Fixation and electron microscopy

As in chapter 4, prior to cross sectioning via FIB and SEM microscopy, sample preparations were performed. The procedure was described in detail in previous chapter.

It should be noted that this experiment was only performed once and the presented micrograph is not giving the strong answer regarding the actual interface, since the nanostraw on the electrode is not in good condition. However, the sample preparation, staining-resin embedding, and also FIB milling process have been performed well (Figure 5.13).

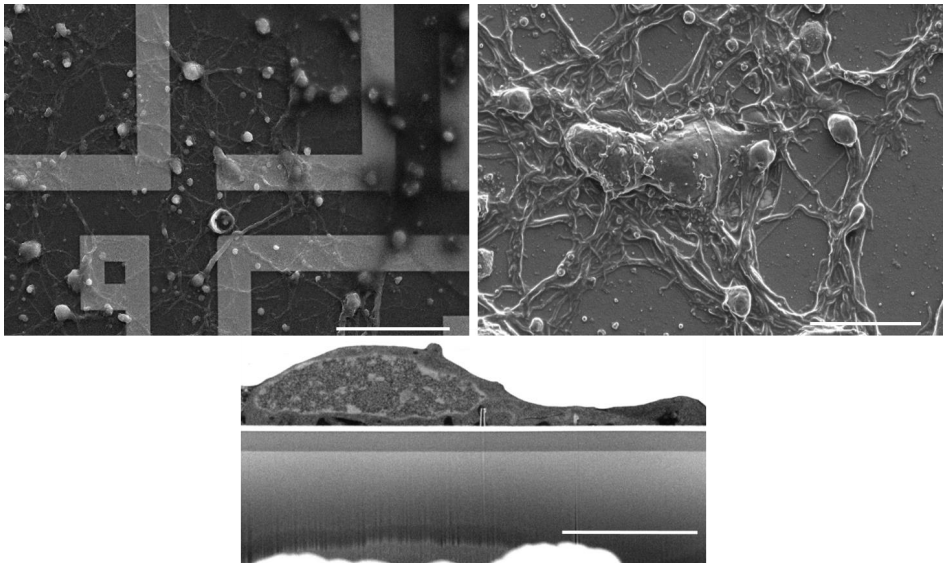

Figure 5.13 Scales: Tope left: 100 um-Top bottom: 20 um- Bottom 5um

5.9 Electrophysiological investigation of neuronal cells on NS-cavity MEAs

For electrophysiological characterization, 790 cell/mm^2 (200 k in 18 mm inner radius ring) cortical neurons from rat embryos were seeded on each chip and kept in culture at least for two weeks enabling electrical recording of the neuronal cells when reaching their spontaneous activities.

Electrophysiological recordings were performed by an in-house made 64 channel pre-amplifier [58] and headstage connected to the main amplifier. In order to evaluate the nanostraw-nanocavity MEAs, recordings were done with multiple devices.

For the purpose of the device performance and network connectivity investigations, recording of the device containing 62 channels were taken into account. Figure 5.14 represents 20 seconds recording of the NS-NC-MEAs at 18 DIV. As it is presented, 35 out of 62 channels are showing electrical activities (Figure 5.14.a), containing bursting activities (Figure 5.14.b) which fits well with the micrograph (Figure 5.12) and the number of alive cells on the center/ near electrodes (37 out of 62 electrodes). This resembles the strong connectivity of the neuronal network as well as high performance of the device.

It should be mentioned that in order to evaluate our device performance, we repeated the experiments on in multiple cultures and recordings by applying the cleaning procedure after each time usage. This cleaning process was performed using ethanol and ultrapure water, and in some cases treating with O_2 plasma which is described in Appendix 2.

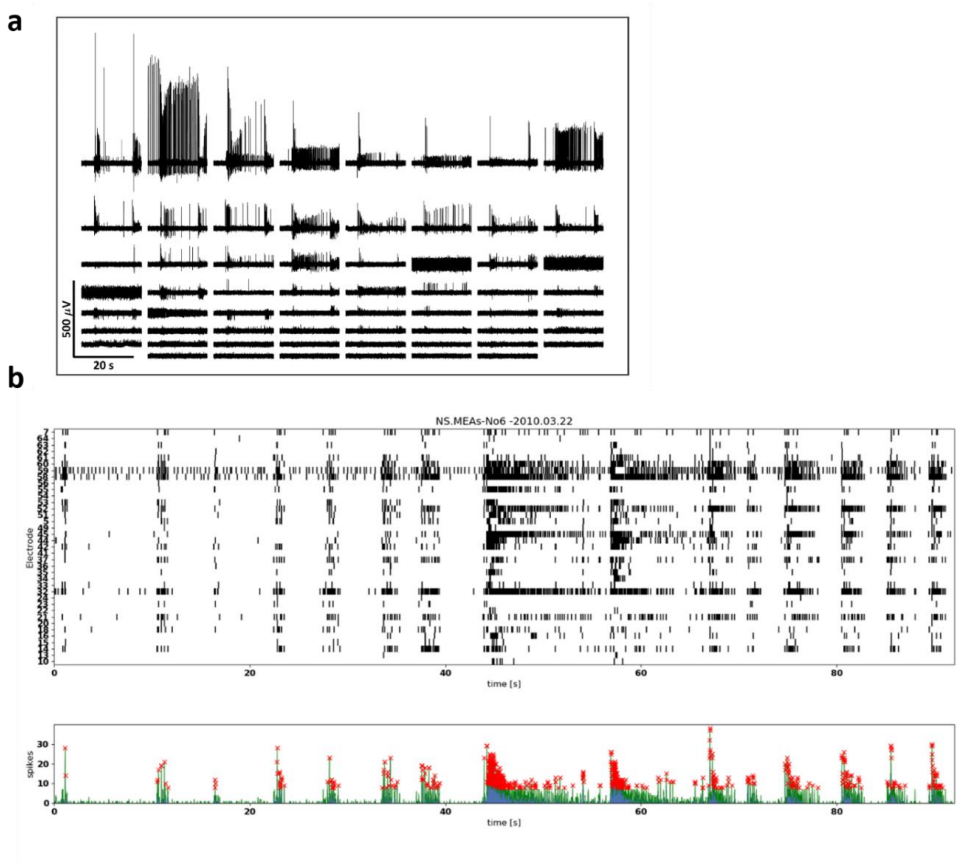

Figure 5.14 Electrophysiological recording of NS-NC-MEAs at 18DIV. a: Simultaneous recordings from 62 channels on Nanostraw nanocavity MEAs. Each spikes is represented as multiplication of signal standard deviation of corresponding channel. b: Raster plot of 35 active channels representing busting activities.

As seen in Figure 5.14.a, most of the recorded signals on different channels are dominated by monophasic positive peaks. In order to evaluate the signal to noise ratio (SNR), signal lever was detected from the peak to peak signal amplitude, and the noise level is determined by taking the root mean square (rms). Calculated average signal to noise ratio (avg. SNR) in all 35 active channels is 16.5, which indicates the high SNR for the recorded signals.

For more investigations, multiple recordings were performed with the individual device or multiple devices. A total number of 72 NS-NC-MEAs with 693 active channels were recorded over 12 neuronal preparations, and their signal amplitudes were taken into consideration. Figure 5.15, represents the scatter plot of all recorded signals. Each dot signifies one recorded signal on the X-axes which implies the signal amplitudes. As seen, detected signals are vary between 40 µV to 9 mV. Based on our research studies, low signal amplitude (40- 100 µV) are comparable to the signals recorded from planar MEAs, due to the loose coupling [128] (Figure 5.15 in green). Signals between 100 µV to 350 µV are matched with the signal reported for nanocavity MEA devices (Figure 5.15 in blue [134]). Furthermore, Signal amplitudes above 350 µV up to 9 mV, are 20 % of all the recorded signals (Figure 5.15 in red). It is observed that the signals with high amplitudes (>350 µV) are mostly dominated by positive spikes.

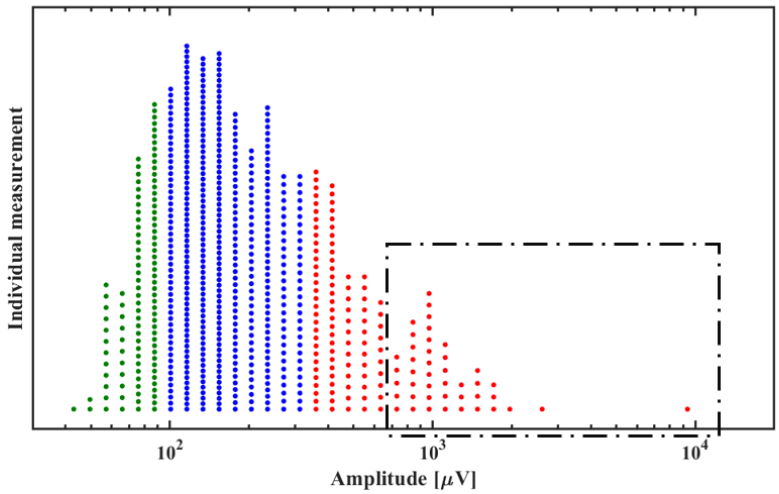

Figure 5.15 Scatter plot of recording 72 NS-NC-MEAs with 693 active channels. Each dots represents one recorded channels with corresponding signal amplitude in X-axes. Green dots, are signals between 40 µV to 100 µV. Blue regions show the signals between 100 µV to 350 µV and resembles signal recorded from nanocavity MEA devices. Red dots are the high amplitude signals which between 350 µV up to 9 mV. Black box (dots) are the recorded signals with the amplitude above 800 µV.

In Figure 5.16, the average spike amplitude of few recorded signals from multiple channels/ devices are plotted. As presented, although the majority of the spike shapes are dominated by positive monophasic spikes, negative and biphasic spikes are also detected in some rare cases.

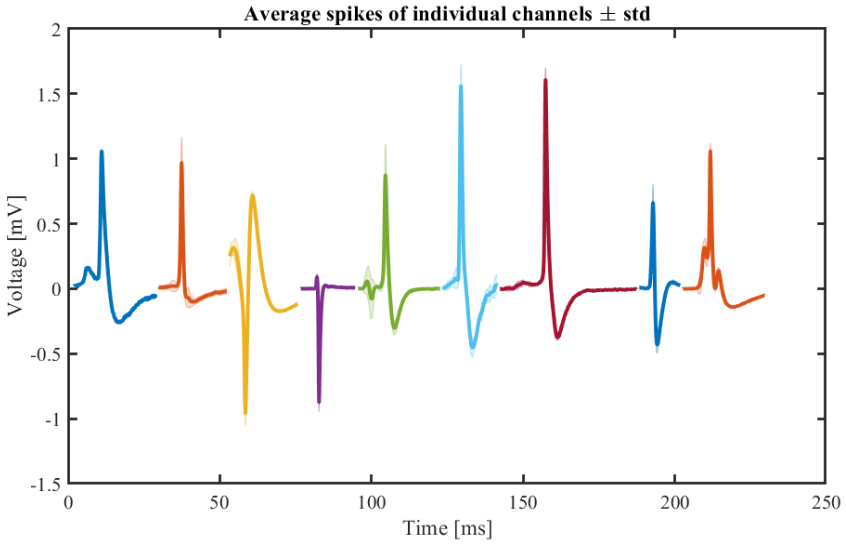

Figure 5.16 Average signal amplitude. Each signal is the average of the signal recorded from the channel and representing different shape of the action potentials for the signals above 800 µV. As seen high amplitude signals are dominated by positive monophasic shapes, but in few cases negative and monophasic is also visualized.

One of the advantages of our device is capability of recording high amplitude signals without an external force, like electroporation and optoporations. For the next experiment, in order to investigate the invasiveness and long-term recording capability, recordings of the device in successive DIVs were performed (Figure 5.17). For this purpose, two different channels were taken into consideration at 14 DIV and 21 DIV. In the first case, Figure 5.17.a, the recorded signals in both days, show a consistent waveform, with the voltage amplitude of 896 µV and noise of 26.4 µV at 14DIV, and the voltage amplitude of 1285 µV and. noise of 52.3 µV at 21 DIV.

However, in the second case, Figure 5.17.b, we observed dramatic increase in the amplitude, with signal amplitude of 430 µV and noise of 26.88 µV at 14 DIV, to 2.6 mV signal amplitude and noise of 100 µV at 21 DIV. Moreover, these signals were recorded with additional small spikes (50-200µV).

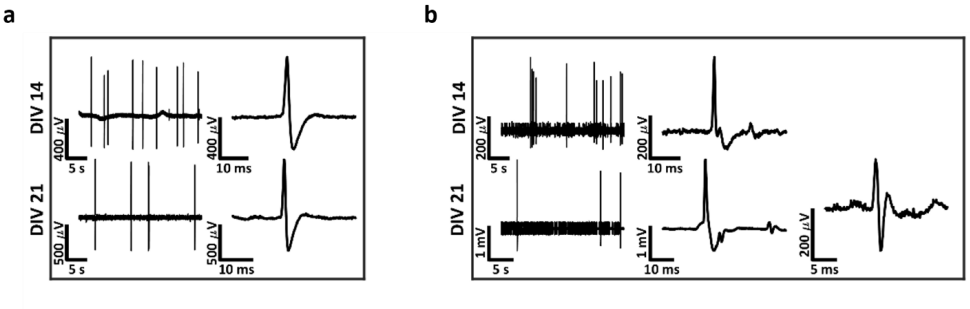

Figure 5.17 Recording of the neuronal activity in successive DIVs at 14 DIV and 21 DIV. a: signal recorded from the channel in 2 different DIVs and no explicit changes in the waveform were observed. b: Signal recorded from a channel in 2 different DIVs and dramatic increase in the amplitude with changes in waveforms were observed, an at 21 DIV, smalls signal amplitudes were also observed.

Remarkably, we noticed that when the signal amplitude was above 800 µV in our other recordings (Figure 5.15 in black box), additional small signals were also appeared. For that, all 38 channels with signal amplitudes above 800 µV were taken into account. Amongst those, 7 channel signals have typical negative peak shape, similar to signals from planar MEAs, monophasic positive peaks were appeared in 9 channels. Interestingly, 22 channels (58% out of 38 channels), exhibited

positive high amplitude signals, followed by small spikes, which could resemble sub-threshold neuronal signals. Few examples of these recorded signals are represented in Figure 5.18.

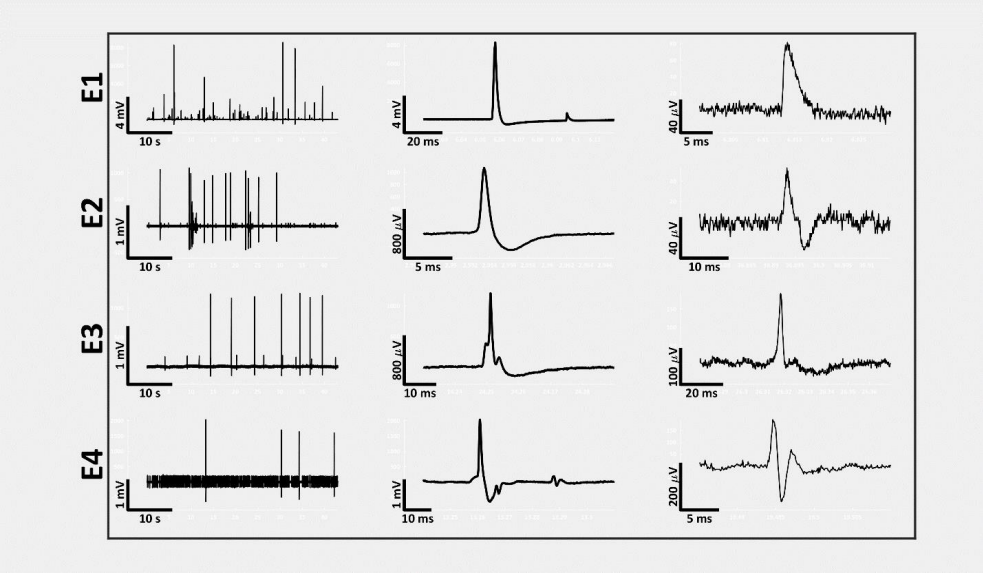

Figure 5.18 Examples of signals recorded above 800 µV, containing small signal amplitudes. Zoom in of the high amplitude signals, and zoom in of the small amplitude signals are presented.

For further electrophysiological investigation of the NS-NC-MEAs, different experiments with 2 types of devices were performed.

In the first experiment, the absence of nanocavity on the NS-MEA was taken into consideration. This experiment was done, in order to evaluate the device while holding the high impedance. Therefore, after the fabrication of NS-MEAs, introduction of nanocavity and applying Cr etchant solution was excluded from the device preparation.

Electrical recording of the device at 14 DIV was performed similar to the previous measurements. Nevertheless, expectedly, no high signal amplitudes were observed in this experiment which could be due to higher impedance of the device and higher the noise level correspondingly.

In the second experiment, the inner part of the NS was filled, in order to determine the straw effect on the device performance. This experiment could help us understanding, whether the large signals recorded or/and the additional small spikes were due to the tight engulfment from outer side of the NS, or/ and through the NS devices.

In order to create such system while maintaining the fabrication process and materials, after the fabrication of NS, the resist (nLOF2020), was not removed from the sample and the experiment was performed with filled-NS-nanocavity MEAs, similar to the previous measurements (at 14 DIV). A total 10 samples were utilized for the measurement, among those 58 channels showed activities. Through these active channels only 2 recorded signals were above 800 μV (with the highest 1735 μV), and no additional small signal was observed.

Although, statistical analysis was not carried out, however, this results could be an indication of the significance necessity of the combination of nanostraw and nanocavity MEAs, for the improvement of the device impedance, tighter engulfment and in total higher SNR. Furthermore, this could be another indication regarding our hypothesis that be the sub-threshold neuronal signals were recorded through nanostraws.

Simultaneous patch clamp and NS-NC MEA recording

To confirm and evaluate the recorded signals with an individual cell resolution from NS-NC-MEAs, patch clamp experiment was performed simultaneously with MEA recordings by Bogdana Cepkenovic.

After recording the neuronal activity with NS-NC-MEA, the recorded channels were observed through upward light microscope and neuron situated on or near the electrode area was chosen for the patch clamp experiment (in current clamp mode) and simultaneous recording of spontaneous of evoked APs with both MEA were measured.

In case of a spontaneous recording, a negative current was applied to keep the recorded potential at -60 mV and signals from both MEA and patch were recorded (Figure 5.19).

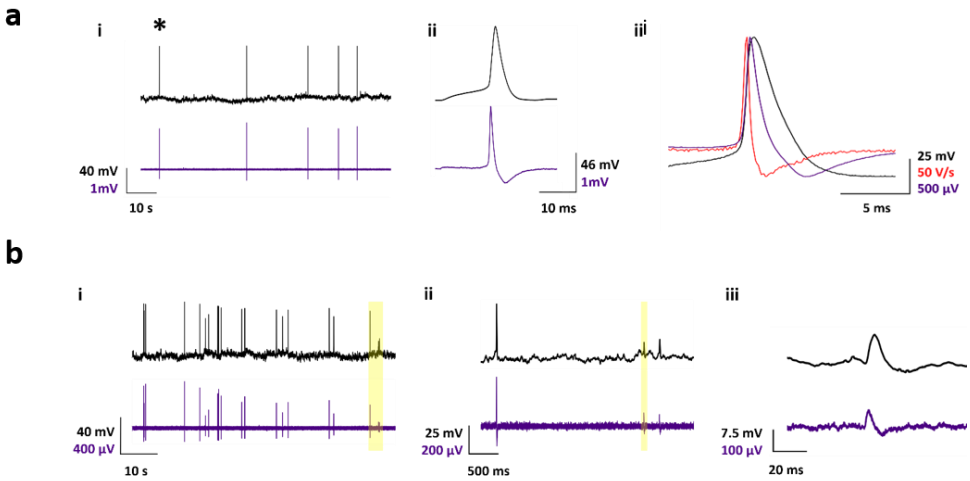

Figure 5.19 Simultaneous patch clamp (black traces) and MEA recording (in purple traces) of spontaneous activity with holding potential of -60 mV. a: (i) Spontaneous recording of neuronal activity, (ii) zoomed in of (i)*. (iii) The overlay of patch clamp (black), its first time derivative (red) and MEA spike (purple). b: NS-NC MEAs are capable of recording intracellularly with PSP resolution. . (i) Simultaneous patch clamp (black) and MEA (blue) recording with firing activities. (ii) Zoom of yellow region in (i), APs and two PSPs recorded by patch and corresponding MEA spikes. (iii) Zoom in of the first PSP (yellow rectangle) in (ii)).

Moreover, +300 pA pulse was induced and the action potential was recorded. Figure 5.20, represents the induced APs simultaneously recorded with patch and MEA. Due to the high capacitance of the MEA, or high-pass filter (72 Hz), the MEA recordings did not show the baseline potential shift towards positive depolarizing values during the stimulation. That MEAs are recording changes in membrane potentials in also confirmed by negative spikes corresponding to the end of stimulation.

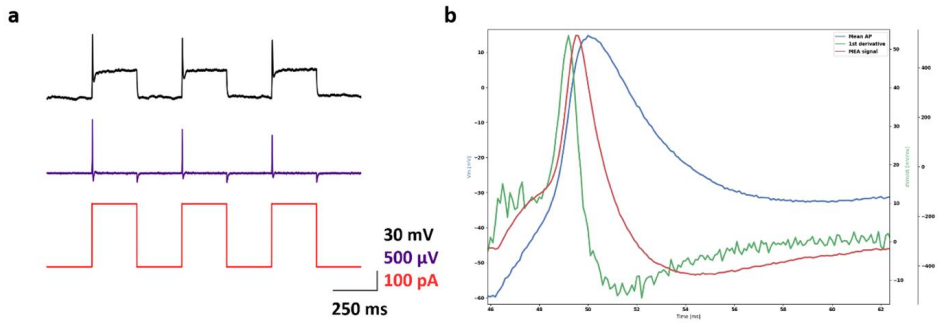

Figure 5.20 Induced APs by applying 300 pA. a: An induced AP recordings by patch clamp (black) and MEA (purple) for 1.75 s. Action potentials were induced by pulses shown in red. b: Comparison of NS-NC MEA recorded spike (red), action potential (blue) and its first time derivative (green). With the average waveforms for a 24.5 s recording.

As seen in Figure 5.19, in both conditions, the signal recorded by NS-NC-MEAs matches the recorded AP by patch clamp, and this indicates the single resolution capability of our device (Figure 5.19.a). Note that, monophasic positive signal shape recorded by MEA resembles the intracellular patch clamp recording with a large transient depolarization followed by hyperpolarization. It is interesting to note that the subthreshold pre-spike depolarization is also recorded by our device and patch, simultaneously Figure 5.19.b). The waveform of MEA recorded signals are between voltage trace recorded AP by patch and the first time derivative, and it could be an indication of in-cell configuration (Figure 5.19.a (iii)).

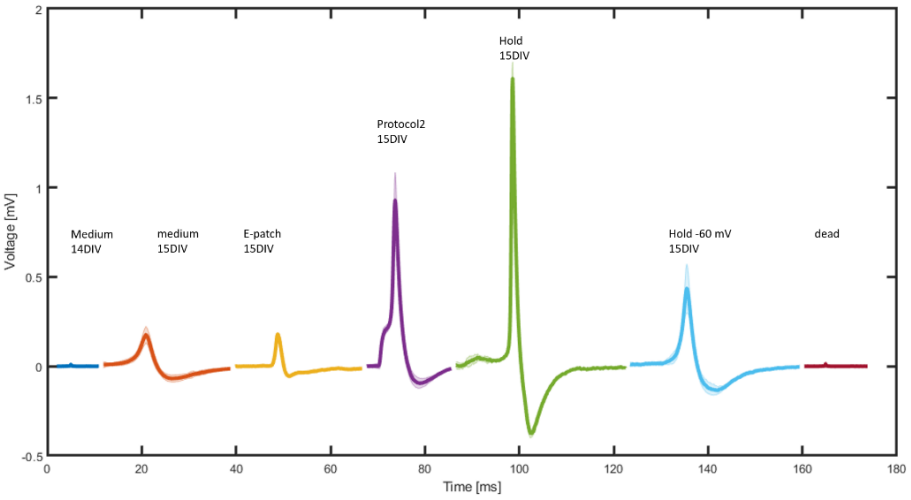

Figure 5.21 An overview of average MEA recording signals in multiple conditions, before and after patch clamp experiment. Blue trace are the avg. signals recorded at 14 DIV. Orange trace is the signals recorded at 15 DIV. yellow trace is the when medium was exchanged with an extracellular patch solution at the same day. Purple is an AP when current with 300pA was applied. Green is the signal on holding. Light blue is when is hold on -60 mV. Red is when the cell was dead and no signal was recorded.

The AP recorded by patch with 58.31 ± 22.59 mV of an amplitude and duration of 4.9 ± 1.94 ms, and corresponding MEA recorded signal with 847.69 ± 637.55 µV and 2.57 ± 1.05 ms in amplitude and duration (Table 5.4).

	Signal amplitudes	Duration
Patch-clamp	58.3 ± 22.59 mV	4.9 ± 1.94 ms
NS-NC-MEAs	847.69 ± 637.55 µV	2.57 ± 1.05 ms

Table 5.4 Signal amplitude and duration recorded by patch clamp and NS-NC-MEAs

As it is presented in Table 6, there is a linear correlation (Pearson´s test: $R = 0.98$, $p < 0.001$ and $R = 0.69$, $p < 0.001$, respectively) between the AP recorded by patch with 58.31 ± 22.59 mV of an amplitude and duration of 4.9 ± 1.94 ms, and MEA recorded signal with 847.69 ± 637.55 µV and 2.57 ± 1.05 ms in amplitude and duration. All the stated amplitudes are based on peak to peak signals, and the durations are at 50% of an AP height. This shows that the intracellular recordings performed by patch clamp, compared to the in-cell recording by MEA device is longer in duration, which is in accordance with the previous studies [34] [52] [30].

In our previous MEA recordings large signals with additional small spikes were detected as presented in Figure 5.17 and Figure 5.18, and was also observed by other groups [34] [52] [30] which attributed as subthreshold potentials. In our simultaneous recordings, post synaptic potential signals recorded by patch was simultaneously detected by our MEA signals as well which is the confirmation of PSP resolution capability of our NS-NC-MEAs. Our device might also be sensitive for other biological events as well, but we could not detected since the hardware applied high-pass filter was 72 Hz.

The calculated coupling coefficient, which is the peak to peak amplitude of MEA spikes versus an action potential record by patch is : $a = APA_{MEA} / APA_{Patch}$ [79], represents the seal resistance and junctional membrane resistance relation ($a = R_{seal}/(R_{seal}+ R_{JM})$). This coupling coefficient was estimated then ca. 1 % which is about 10x larger than reported values for planar MEAs [36]. To estimate the seal resistance R_{seal} we performed further electrophysiological measurements and used standard point contact model [135] (see Figure 5.22).

Estimation of $\mathbf{R_{seal}}$ values using point contact model

As mentioned for estimation and comparison of R_{seal} in different cell-electrode couplings (Figure 5.22), point contact model was used. This approach has been adapted previously by Wrobel [95] for characterization of coupling between a field effect transistor and HEK cells. In this work point contact model was also used in order to estimate the R_{seal} for cell and nanostraw coupling, which was done by Justus Bednár.

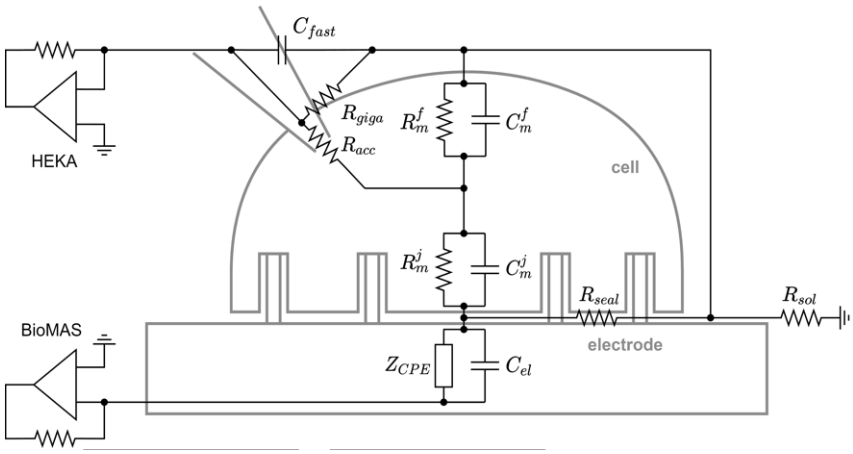

Figure 5.22 Electrical point-contact-model for a cell. Tight seal formed between cell and a nanostraw-MEA, together with a patch pipette, that is used for intracellular stimulation and measurement.

By fitting the analytical expressions (5.1) and (5.2) respectively to V_{MEA}, the time constant (5.3) will be obtained as one of the optimized parameters 0, V_0 and τ. This is the time constant of exponential decay of corresponding MEA transients upon the end of the pulse Voltage, in voltage clamp mode.

Due to our interest in an estimated value of R_{seal}, it is necessary to assume a value for C_m^j. The total capacitance of the cell membrane, sometimes referred to C_{slow} which is defined experimentally by patch clamp.

$$V_{on}(t) = O + V_0 \cdot e^{-\frac{t-t_0}{\tau}} \tag{5.1}$$

$$V_{off}(t) = O - V_0 \cdot e^{-\frac{t-t_0}{\tau}} \tag{5.2}$$

$$\tau = C_m^j \cdot R_{seal} \tag{5.3}$$

C_{slow} is connected to C_m^j by equations (5.4) and (5.5) with α, the ratio of junctional cell membrane area, A_j, to the total cell membrane area, A_t.

$$C_{slow} = C_m^j + C_m^f \tag{5.4}$$

$$C_m^j = \alpha \cdot C_{slow} \tag{5.5}$$

With the comparison of A_j and the bottom of a half-sphere and A_t with the total surface of that half-sphere, the obtained α value was on the correct order of magnitude. Nevertheless, due to the complexity of the neuron topography, the value of $\alpha = 1/3$ was given as an upper boundary and therefore R_{seal} value, using calculation (5.6), as a lower boundary was calculated:

$$R_{seal} = \frac{\tau}{\alpha \cdot C_{slow}} \tag{5.6}$$

In this regard, the condition of extracellular measurements with an intact cell membrane were taken into consideration (Tight seal). To define R_{seal} values, voltage-clamp measurement was performed. An intracellular voltage, V_{in} is applied and gets clamped to a pre-defined value, while the MEA signal was recorded, V_j [95] (based on a point contact model: $V_J = V_{MEA}$.). When applying a voltage to V_{in}, the voltage of the cleft between cell and nanostraw-MEA, V_j, first follows the V_{in}, but then decays (τ) exponentially. It can be assumed that the decay time is due to the membrane capacitance of the junction C_m^j and R_{seal} ($\tau = C_m^j \cdot R_{seal}$). When the voltage clamp of the cell ends, a second exponential response of V_{MEA} was observed for a similar reason (current over sealing resistance) (See equivalent circuit in Figure 5.23).

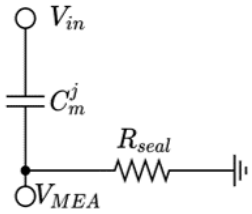

Figure 5.23 Equivalent circuit used for modeling R_{seal}

For estimating the R_{seal}, the exponential fits to V_{MEA} were used with the assumption of $C_m^j = 1/3 C_m$ and C_m can be determined during the patch clamp experiment. In Figure 5.24, the model of V_{MEA} during stimulus onset and offset together with exponential fits are shown.

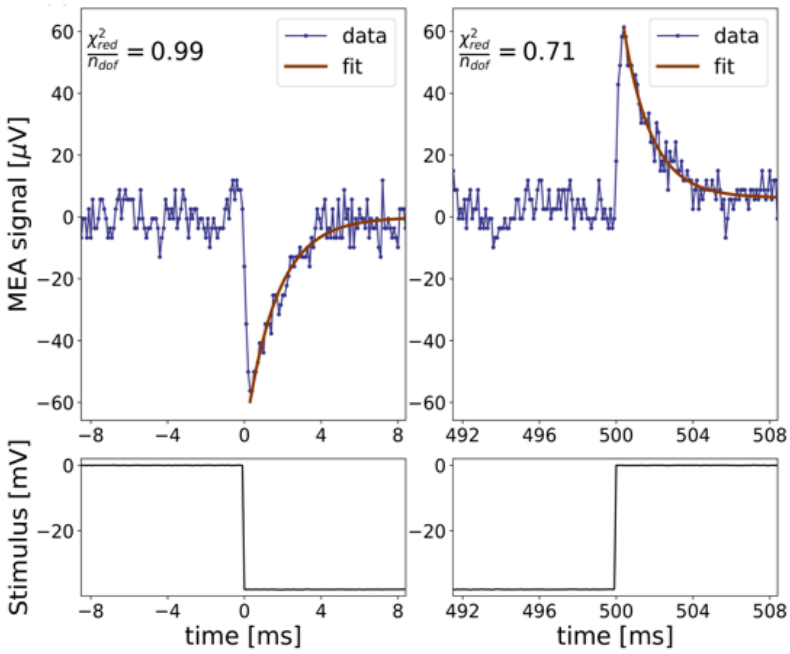

Figure 5.24 Voltage Clamp responses of MEA-signals at rising and falling edge of a negative patch clamp stimulus. (Sample 3). The results of exponential fits are indicated in red.

R_{seal} Obtained values for τ were depicted and R_{seal} matches the expected range. Obtained values for τ were between 0.5 – 2.5 ms, resulting in R_{seal}, between 20 MΩ and 400 MΩ. Although this values are above those planar MEA recordings [136], it must be noted that in order to precisely evaluate the R_{seal} , the electrode opening size is required [135]. Taking into account the coupling coefficient α ~ 1%, and the seal resistance R_{seal} ~ 20-400 MΩ leads to the junctional membrane resistance RJM ~ 2-40 GΩ which is in accordance to literature values for in-cell recordings [34].

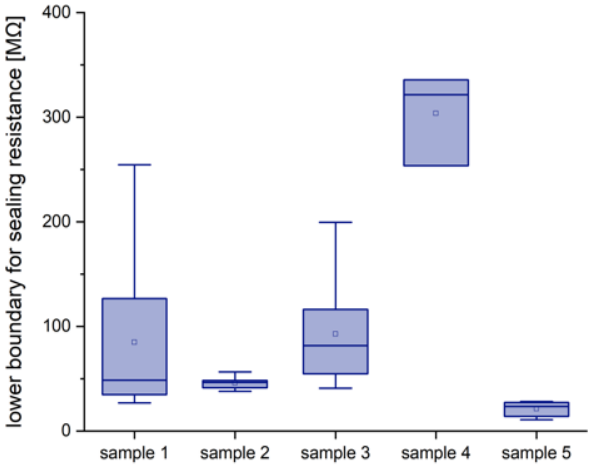

Figure 5.25 Boxplot with values of R_{seal}. Sample 4 has the highest R_{seal} and the lowest signal amplitude among other samples.

5.10 Conclusion

MEA devices have been used over decades for recording the neuronal action potentials. However, signal recorded with these devices are limited in high noise and low signal amplitudes. Various methods were developed for the improvement of the signal recordings by lowering the device impedance leading to reducing the noise and enhancing the seal resistance which results in a signal improvement.

In this chapter, we combine vertical nanostraws and nanocavity MEAs for further improvement in signal to noise ratio of neuronal electrical action potentials. Two approaches are applied for this improvement. Firstly, by introduction of nanocavity-MEAs, the contact resistant is improved while maintaining the electrode aperture and therefore reduction in the impedance. Another methodology is implementing high aspect ratio nanostraws on the electrode area, and therefore when interfacing cell, thanks to cell membrane plasticity and high adhesion, the sealing resistance improves dramatically and leads to tight engulfment and in 3% of the cases spontaneous in-cell penetration occurs.

Nanostraws made of TiO_2 are fabricated similar to the previous chapter, on the Au/Pt surface. However, in this experiment, the microelectrodes are passivated with ONONO layer and for the introduction of nanocavity, Cr etchant solution is applied and the nanocavity area is controlled via up-ward light microscope.

The electrical performance of the device then is evaluated by electrochemical impedance measurement and the effect of nanocavity introduction on the impedance reduction is confirmed. Moreover, the electrophysiological measurement confirm the spontaneous intracellular recording (in-cell recordings) of neuronal cells (14-24 DIV) in 20% of cases with PSP resolution and prove by simultaneous patch clamp and MEA recordings.

Chapter 6. Summary and outlook

The focus of this thesis is investigation of the interface between the neuronal cells and electronic devices. Conventional MEAs are most widely used for extracellular recording of action potentials. When this planar electrodes interfacing cells, due to the gap between cell membrane and electrode surface (cleft) which results in low coupling, only larger signals can be detected. Moreover, because of small electrode aperture, the noise amplitudes are high. The combination of these two issues result in low SNR of the recorded signals using planar MEAs. Numerous methods and materials have been developed in order to overcome these limitations. Application of vertical nanostructures were presented in literature for improving the coupling between the cell and substrate. These 3D structures reduce the cleft and therefore increase the sealing resistance and signal amplitude. In the later researches it is reported that the high aspect ratio causes tight engulfment and therefore increases the signal amplitude. Introduction of nanocavity between the electrode opening and passivation, on the other hand, increase the effective area without increasing the electrode opening, and reduce the impedance of the electrode and as a result decreases the noise amplitude.

In the body of this work, I have combined these two state-of-the-art approaches by designing high aspect ratio nanostructures on nanocavity-MEAs and developed a new type of nanoelectrodes for improving the SNR of the neuronal electrical activities. High aspect ratio nanostraws made of TiO_2 served as nanostructures, and Cr layer between electrode and passivation served as sacrificial layer and etched chemically for creation of nanocavity MEAs. The fabrication of nanostraws is reproduced very well because of using electron beam lithography in combination with ALD processes.

At first, before employing the nanostraws on the nanocavity-MEAs, we designed and fabricated the nanostraws on a planar substrate (Au) for the ease of fabrication in each step. Moreover, since the electrode openings were in a range of few µm (6µm and 10 µm), because of single cell resolution, unlimited amount of nanostraws were not feasible to be implemented on the electrodes. Therefore, different pitches between nanostraws were designed (1 µm, 2µm, 4µm and 5 µm) on Au substrate, fabrication materials and parameters were established. Then, the interface between the nanostraws (with different pitches) and neuronal cells via microscopic techniques were interrogated. Fluorescence microscopy was used to characterize the cell viability of the gold substrates containing nanostraws. We then characterized the mechanical responses of cell when interfacing nanostraws, by performing actin and membrane staining. Furthermore, for high resolution (nanometers) investigation of the interface between cell and nanostraw, electron microscopy and cross sectioning were carried out. These microscopic methods confirmed the tight seal and even deformation of plasma membrane and nucleus, in all 4 different pitches. However, in case of of 1 µm pitch, cells failed to bend between the nanostraws, due to the spacing and thus

cells were placed on top of the structures. Therefore, we selected 2 µm spacing between nanostraws as the most sufficient pitch for the MEA electrode size.

In the later part of this work, nanostraws with 2 µm pitches were designed and implemented on the nanocavity-MEA. Cortical rat neurons were cultured and the electrical recordings between 14 to 24 DIV were performed using in-house developed electrophysiology setup, so called BioMAS setup. The nanostraw-nanocavity MEA represented the high performance of recording neuronal networks with firing activities. Moreover, our device is able to record high SNR for multiple cultures after proper cleaning. In contrast to state of the art literature no external forces like optoporation or electroporation [44] are required to achieve high percentage of in-cell recordings. Even more, the high sensitivity of our device allows the detection of sub-threshold signals like PSPs.

Even though combination of nanostraw and nanocavity MEAs exhibit high potential for neuronal recordings in network level, nevertheless, to improve the probability of intracellular recordings, more optimization is required. One of the opportunity is integrating our device to HD-MEAs (CMOS-MEAs) [137] [138] to increase the spatial resolution and capability of intracellular recordings at sub-cellular level. This approach would support to comprehend of signal at network level, plus single cell level and its components such as, soma, axon and dendrites. Further, this methodology can be extended in combination with *in vivo* electrophysiological devices for mapping the neuronal circuit with high temporal and high SNR resolution.

Chapter 6. Summary and outlook

Acknowledgments

I would like to express my sincere gratitude to all my friends, family and the colleagues at **ICS8/IBI3** institute for their help and support during my research and writing process. In particular I would like to thank following people.

First and foremost I am extremely grateful to **Prof. Dr. Offenhäusser** for giving me the opportunity to be part of this great institute. I was blessed to work at your group under your supervision. Your constant supports, encouragements and even criticisms helped me grow up not only as a scientist but also as a person for life. Additionally your open nature and great personality create great vibes, make our institute even more special. This motivated me to continue even in difficult times and made me love my job every day more and more.

Prof. Dr. Fitter thank you for kindly accepting to be the second examiner of my work.

I want to thank **Dr. Vanessa Maybeck** for your help in every steps of my work. Your advices, supports and criticisms motivated me find my way in the right direction. I think every groups need someone like you.

I am deeply grateful to **Marko**, Michael and Regina for all the cleanroom supports. Thank you for all the technical/non-technical discussions and guidance. Your kind attitudes created a friendly environment for all of us to work in.

I would like to especially thank **Dr. Stefan Trellenkamp** and **Dr. Florian Lentz** for not only the E-beam lithography supports, but also for all the productive discussions which helped me find the best way to produce my devices.

I would like to thank **Dr. Elmar Neumann** and **Elke** for their support regarding staining and FIB cut and specifically all great ideas at the beginning of my PhD work.

I would like to thank **Tina** for first of all the Bio-lab supports, and also for everything else. You are the symbol of kind and strong woman who always eager to help others.

I would like to thank all the HNF staff, for your unconditional supports. In particular, **Bernd**, **Mathias**, **Janin**, **Hubbert**, **Andrea**, **Gregory** and **Steffi**, Working with you made the cleanroom work a lot more fun and also pave the way for the successful device fabrication.

I would like to thank **Dr. Dirk Mayer**, not only for answering all the basic chemistry questions, but also for organizing a lot of fun activities which make our institute even more amazing.

I would like to thank **Susanne** for everything you do at the institute and kindly answering all the quick questions.

I would thank all the IT staff, specifically **Sacha** and **Stefan** for your technical supports and quick responses.

Bogdana, I am deeply grateful to have you as both a colleague and a friend. Your motivation and persevere always inspired me. Thank you in particular for the patch-clamp support. Working with you was a great experience.

Frano, I would like to thank you for helping me in the fluorescence and confocal microscopy part of the project. It was great working with you.

Erfan, thank you for all your supports especially when it came to data processing. You were always there when I needed.

Jamal, **Jasmin** and **Bogdana**, it was an honor for me to have the experience of being a supervisor. I have learned a lot with you.

Stella, **Jamal**, **Bohdan**, **Viviana**, **Kagithiri**, **Lena**, **Ekaterina**, **Timm**, **Dominik**, **Nouran**, **Irina**, **Silke**, **Corrina**, **Jelena**, **Gabriela**, **Chris**, **Justus**, **Niko** and all the IBI3 members, I cannot be more grateful for having you guys as my colleagues and friends during all these years. Thank you, not only for the scientific discussions and supports, but also for the great people you are. I will always appreciate all our memorable time at work, summer/winter schools, Christmas parties, hiking trips, Firmenlauf, outdoor activities, lasertag, bus trips and gym.

I would like to thank **Anastasia** for being a nice and funny office-mate. Specially coping with the warm office in winter.

My flat mate **Bruna** who always supports me and celebrates the success with me.

Pooneh, thank you for being such a wonderful sister. You and **Kamyar** always support me and believe in me, even when I do not believe in myself. Thank you two for always being there for me no matter what.

My parents, thanks for your unconditional love and constant support. You always encourage me to reach my goals and to be a better version of myself. Thank you for the life you made for us, and thank you for guiding us to be strong people.

My grandma, who passed away in my PhD time, she has been always my role model as a strong woman who lived life the way she wanted. My dream is to live a life the way she did.

Acknowledgments

References

[1] D. R. Tobergte and S. Curtis, “Introductory guide to patch clamp electrophysiology,” *J. Chem. Inf. Model.*, vol. 53, no. 9, pp. 1689–1699, 2013.

[2] J. Oliver, *Patch-Clamp Analysis Advanced Techniques*, vol. 53, no. 9. 2013.

[3] J. S. Jouhanneau and J. F. A. Poulet, “Multiple Two-Photon Targeted Whole-Cell Patch-Clamp Recordings from Monosynaptically Connected Neurons in vivo,” *Front. Synaptic Neurosci.*, vol. 11, no. MAY, pp. 1–13, 2019.

[4] A. Segev, F. Garcia-Oscos, and S. Kourrich, “Whole-cell patch-clamp recordings in brain slices,” *J. Vis. Exp.*, vol. 2016, no. 112, pp. 1–10, 2016.

[5] C. C. H. Petersen, “Whole-Cell Recording of Neuronal Membrane Potential during Behavior,” *Neuron*, vol. 95, no. 6, pp. 1266–1281, 2017.

[6] G. Wang *et al.*, “An optogenetics- and imaging-assisted simultaneous multiple patch-clamp recording system for decoding complex neural circuits,” *Nat. Protoc.*, vol. 10, no. 3, pp. 397–412, 2015.

[7] B. Neurobiology, *Encyclopedia of Psychopharmacology*. 2010.

[8] C. E. Urch and A. H. Dickenson, “In vivo single unit extracellular recordings from spinal cord neurones of rats,” *Brain Res. Protoc.*, vol. 12, no. 1, pp. 26–34, 2003.

[9] M. T. Chen, M. Morales, D. J. Woodward, B. J. Hoffer, and P. H. Janak, “In vivo extracellular recording of striatal neurons in the awake rat following unilateral 6-hydroxydopamine lesions,” *Exp. Neurol.*, vol. 171, no. 1, pp. 72–83, 2001.

[10] A. Fendyur and M. E. Spira, “Toward on-chip, in-cell recordings from cultured cardiomyocytes by arrays of gold mushroom-shaped microelectrodes,” *Front. Neuroeng.*, vol. 5, no. AUGUST, pp. 1–10, 2012.

[11] V. Viswam, M. E. J. Obien, F. Franke, U. Frey, and A. Hierlemann, “Optimal electrode size for multi-scale extracellular-potential recording from neuronal assemblies,” *Front. Neurosci.*, vol. 13, no. APR, pp. 1–23, 2019.

[12] P. Massobrio, G. Massobrio, and S. Martinoia, “Interfacing cultured neurons to microtransducers arrays: A review of the neuro-electronic junction models,” *Front. Neurosci.*, vol. 10, no. JUN, pp. 1–13, 2016.

[13] Y. Zhao, S. S. You, A. Zhang, J.-H. Lee, J. Huang, and C. M. Lieber, “Scalable ultrasmall three-dimensional nanowire transistor probes for intracellular recording,” *Nat. Nanotechnol.*, 2019.

[14] T. Berthing *et al.*, “Cell membrane conformation at vertical nanowire array interface revealed by fluorescence imaging,” *Nanotechnology*, vol. 23, no. 41, 2012.

[15] X. Xie, A. M. Xu, S. Leal-Ortiz, Y. Cao, C. C. Garner, and N. a Melosh, “Nanostraw -

Electroporation System for Highly Efficient Intracellular Delivery and Transfection.," *ACS Nano*, vol. 7, no. 5, pp. 4351–4358, 2013.

[16] Y. Cao *et al.*, "Nondestructive nanostraw intracellular sampling for longitudinal cell monitoring," *Proc. Natl. Acad. Sci. U. S. A.*, vol. 114, no. 10, pp. E1866–E1874, 2017.

[17] X. Xie, A. M. Xu, M. R. Angle, N. Tayebi, P. Verma, and N. A. Melosh, "Mechanical model of vertical nanowire cell penetration," *Nano Lett.*, vol. 13, no. 12, pp. 6002–6008, 2013.

[18] R. Liu *et al.*, "High Density Individually Addressable Nanowire Arrays Record Intracellular Activity from Primary Rodent and Human Stem Cell Derived Neurons," *Nano Lett.*, vol. 17, no. 5, pp. 2757–2764, 2017.

[19] J. T. Robinson, M. Jorgolli, A. K. Shalek, M.-H. Yoon, R. S. Gertner, and H. Park, "Vertical nanowire electrode arrays as a scalable platform for intracellular interfacing to neuronal circuits," *Nat. Nanotechnol.*, vol. 7, no. 3, pp. 180–184, 2012.

[20] S. Weidlich, K. J. Krause, J. Schnitker, B. Wolfrum, and A. Offenhäusser, "MEAs and 3D nanoelectrodes: electrodeposition as tool for a precisely controlled nanofabrication," *Nanotechnology*, vol. 28, no. 9, p. 095302, 2017.

[21] W. Zhao *et al.*, "Nanoscale manipulation of membrane curvature for probing endocytosis in live cells," *Nat. Nanotechnol.*, no. June, pp. 1–9, 2017.

[22] F. Santoro, J. Schnitker, G. Panaitov, and A. Offenhäusser, "On chip guidance and recording of cardiomyocytes with 3D mushroom-shaped electrodes," *Nano Lett.*, vol. 13, no. 11, pp. 5379–5384, 2013.

[23] F. Santoro *et al.*, "Interfacing electrogenic cells with 3D nanoelectrodes: Position, shape, and size matter," *ACS Nano*, vol. 8, no. 7, pp. 6713–6723, 2014.

[24] F. Santoro, E. Neumann, G. Panaitov, and A. Offenhäusser, "FIB section of cell-electrode interface: An approach for reducing curtaining effects," *Microelectron. Eng.*, vol. 124, pp. 17–21, 2014.

[25] C. Xie, Z. Lin, L. Hanson, Y. Cui, and B. Cui, "Intracellular recording of action potentials by nanopillar electroporation," *Nat. Nanotechnol.*, vol. 7, no. 3, pp. 185–190, 2012.

[26] F. Santoro *et al.*, "Revealing the Cell-Material Interface with Nanometer Resolution by Focused Ion Beam/Scanning Electron Microscopy," *ACS Nano*, vol. 11, no. 8, pp. 8320–8328, 2017.

[27] A. Hai, J. Shappir, and M. E. Spira, "In-cell recordings by extracellular microelectrodes," *Nat. Methods*, vol. 7, no. 3, pp. 200–202, Mar. 2010.

[28] X. Duan *et al.*, "Intracellular recordings of action potentials by an extracellular nanoscale field-effect transistor," *Nat. Nanotechnol.*, vol. 7, no. 3, pp. 174–179, 2012.

[29] M. R. Angle, B. Cui, and N. A. Melosh, "Nanotechnology and neurophysiology," *Curr. Opin. Neurobiol.*, vol. 32, pp. 132–140, 2015.

[30] M. Dipalo *et al.*, "Intracellular and Extracellular Recording of Spontaneous Action Potentials in Mammalian Neurons and Cardiac Cells with 3D Plasmonic Nanoelectrodes,"

Nano Lett., p. acs.nanolett.7b01523, 2017.

[31] B. X. E. Desbiolles, E. de Coulon, A. Bertsch, S. Rohr, and P. Renaud, "Intracellular Recording of Cardiomyocyte Action Potentials with Nanopatterned Volcano-Shaped Microelectrode Arrays," *Nano Lett.*, vol. 19, no. 9, pp. 6173–6181, 2019.

[32] D. Brüggemann, B. Wolfrum, V. Maybeck, Y. Mourzina, M. Jansen, and A. Offenhäusser, "Nanostructured gold microelectrodes for extracellular recording from electrogenic cells," *Nanotechnology*, vol. 22, no. 26, 2011.

[33] J. T. Robinson, M. Jorgolli, and H. Park, "Nanowire electrodes for high-density stimulation and measurement of neural circuits," *Front. Neural Circuits*, vol. 7, no. March, pp. 1–5, 2013.

[34] N. Shmoel, N. Rabieh, S. M. Ojovan, H. Erez, E. Maydan, and M. E. Spira, "Multisite electrophysiological recordings by self-assembled loose-patch-like junctions between cultured hippocampal neurons and mushroom-shaped microelectrodes," *Sci. Rep.*, vol. 6, no. January, p. 27110, 2016.

[35] S. M. Ojovan *et al.*, "A feasibility study of multi-site,intracellular recordings from mammalian neurons by extracellular gold mushroom-shaped microelectrodes.," *Sci. Rep.*, vol. 5, no. August, p. 14100, 2015.

[36] M. E. Spira and A. Hai, "Multi-electrode array technologies for neuroscience and cardiology," *Nat. Nanotechnol.*, vol. 8, no. 2, pp. 83–94, 2013.

[37] J. J. Vandersarl, A. M. Xu, and N. A. Melosh, "Nanostraws for direct fluidic intracellular access," *Nano Lett.*, vol. 12, no. 8, pp. 3881–3886, 2012.

[38] C. B. Fox *et al.*, "Fabrication of Sealed Nanostraw Microdevices for Oral Drug Delivery," *ACS Nano*, vol. 10, no. 6, pp. 5873–5881, 2016.

[39] W. Zhao, F. Santoro, and B. Cui, *curvature*, vol. 14, no. 6. 2019.

[40] H. Y. Lou, W. Zhao, Y. Zeng, and B. Cui, "The Role of Membrane Curvature in Nanoscale Topography-Induced Intracellular Signaling," *Acc. Chem. Res.*, vol. 51, no. 5, pp. 1046–1053, 2018.

[41] A. Belu *et al.*, "Ultra-thin resin embedding method for scanning electron microscopy of individual cells on high and low aspect ratio 3D nanostructures," *J. Microsc.*, vol. 263, no. 1, pp. 78–86, 2016.

[42] B. D. Almquist and N. A. Melosh, "Fusion of biomimetic stealth probes into lipid bilayer cores," *Proc. Natl. Acad. Sci.*, vol. 107, no. 13, pp. 5815–5820, 2010.

[43] M. Dipalo *et al.*, "Cells Adhering to 3D Vertical Nanostructures: Cell Membrane Reshaping without Stable Internalization," *Nano Lett.*, vol. 18, no. 9, pp. 6100–6105, 2018.

[44] M. Dipalo *et al.*, "Membrane Poration Mechanisms at the Cell–Nanostructure Interface," *Adv. Biosyst.*, vol. 3, no. 12, pp. 1–8, 2019.

[45] C. Nick, S. Quednau, R. Sarwar, H. F. Schlaak, and C. Thielemann, "High aspect ratio gold nanopillars on microelectrodes for neural interfaces," *Microsyst. Technol.*, vol. 20, no. 10–

11, pp. 1849–1857, 2014.

[46] T. Ozel, B. Zhang, R. Gao, R. W. Day, C. M. Lieber, and D. G. Nocera, “Electrochemical Deposition of Conformal and Functional Layers on High Aspect Ratio Silicon Micro / Nanowires Electrochemical Deposition of Conformal and Functional Layers on High Aspect Ratio Silicon Micro / Nanowires,” 2017.

[47] F. De Angelis *et al.*, “3D hollow nanostructures as building blocks for multifunctional plasmonics,” *Nano Lett.*, vol. 13, no. 8, pp. 3553–3558, 2013.

[48] A. M. Xu *et al.*, “Quantification of nanowire penetration into living cells,” *Nat. Commun.*, vol. 5, pp. 1–8, 2014.

[49] Z. C. Lin, C. Xie, Y. Osakada, Y. Cui, and B. Cui, “Iridium oxide nanotube electrodes for sensitive and prolonged intracellular measurement of action potentials,” *Nat. Commun.*, vol. 5, pp. 1–10, 2014.

[50] Z. C. Lin *et al.*, “Accurate nanoelectrode recording of human pluripotent stem cell-derived cardiomyocytes for assaying drugs and modeling disease,” *Microsystems Nanoeng.*, vol. 3, no. October 2016, p. 16080, 2017.

[51] J. Abbott, T. Ye, D. Ham, and H. Park, “Optimizing Nanoelectrode Arrays for Scalable Intracellular Electrophysiology,” *Acc. Chem. Res.*, vol. 51, no. 3, pp. 600–608, 2018.

[52] J. Abbott *et al.*, “A nanoelectrode array for obtaining intracellular recordings from thousands of connected neurons,” *Nat. Biomed. Eng.*, vol. 4, no. FebruarY, Feb. 2019.

[53] Y. Liu *et al.*, “Soft conductive micropillar electrode arrays for biologically relevant electrophysiological recording,” *Proc. Natl. Acad. Sci.*, vol. 115, no. 46, pp. 11718–11723, 2018.

[54] X. Li *et al.*, *A nanostructure platform for live-cell manipulation of membrane curvature*, vol. 14, no. 6. Springer US, 2019.

[55] A. Czeschik *et al.*, “Nanostructured cavity devices for extracellular stimulation of HL-1 cells,” *Nanoscale*, vol. 7, no. 20, pp. 9275–9281, 2015.

[56] A. Czeschik, A. Offenhäusser, and B. Wolfrum, “Fabrication of MEA-based nanocavity sensor arrays for extracellular recording of action potentials,” *Phys. Status Solidi Appl. Mater. Sci.*, vol. 211, no. 6, pp. 1462–1466, 2014.

[57] E. Kätelhön, D. Mayer, M. Banzet, A. Offenhäusser, and B. Wolfrum, “Nanocavity crossbar arrays for parallel electrochemical sensing on a chip,” *Beilstein J. Nanotechnol.*, vol. 5, no. 1, pp. 1137–1143, 2014.

[58] B. Hofmann, E. Kätelhön, M. Schottdorf, A. Offenhäusser, and B. Wolfrum, “Nanocavity electrode array for recording from electrogenic cells,” *Lab Chip*, vol. 11, no. 6, pp. 1054–1058, 2011.

[59] B. A. Olshausen, “Book Review: Theoretical Neuroscience,” *J. Cogn. Neurosci.*, vol. 15, no. 1, pp. 154–155, 2003.

[60] M. Thé *et al.*, “Anisotropy of cell adhesive microenvironment governs cell internal

organization and orientation of polarity," *Proc. Natl. Acad. Sci. U. S. A.*, vol. 103, no. 52, pp. 19771–19776, 2006.

[61] M. Bornens, "The centrosome in cells and organisms," *Science (80-.).*, vol. 335, no. 6067, pp. 422–426, 2012.

[62] K. Haddeland and U. Soderham, "Sykepleierstudenters opplevelse av veiledningssituasjoner med sykepleiere i sykehuspraksis," *Nord. Sygeplejeforskning*, vol. 3, no. 1, pp. 18–32, 2013.

[63] W. Yu and P. W. Baas, "Changes in microtubule number and length during axon differentiation," *J. Neurosci.*, vol. 14, no. 5 I, pp. 2818–2829, 1994.

[64] J. C. R. Jones, A. E. Goldman, P. M. Steinert, S. Yuspa, and R. D. Goldman, "Dynamic aspects of the supramolecular organization of intermediate filament networks in cultured epidermal cells," *Cell Motil.*, vol. 2, no. 3, pp. 197–213, 1982.

[65] R. Kirmse, Z. Qin, C. M. Weinert, A. Hoenger, M. J. Buehler, and L. Kreplak, "Plasticity of intermediate filament subunits," *PLoS One*, vol. 5, no. 8, pp. 1–11, 2010.

[66] A. L. Hodgkin and A. F. Huxley, "A quantitative description of ion currents and its applications to conduction and excitation in nerve membranes," *J. Physiol.*, vol. 117, no. 1, pp. 500–544, 1952.

[67] D. Smetters, A. Majewska, and R. Yuste, "Detecting action potentials in neuronal populations with calcium imaging," *Methods A Companion to Methods Enzymol.*, vol. 18, no. 2, pp. 215–221, 1999.

[68] G. T. Wetzel and T. S. Klitzner, "Developmental cardiac electrophysiology recent advances in cellular physiology.," *Cardiovasc. Res.*, vol. 31 Spec No, pp. E52-60, Feb. 1996.

[69] V. Benfenati *et al.*, "A transparent organic transistor structure for bidirectional stimulation and recording of primary neurons," *Nat. Mater.*, vol. 12, no. 7, pp. 672–680, 2013.

[70] E. W. Keefer, B. R. Botterman, M. I. Romero, A. F. Rossi, and G. W. Gross, "Carbon nanotube coating improves neuronal recordings," *Nat. Nanotechnol.*, vol. 3, no. 7, pp. 434–439, 2008.

[71] M. H. W. Chan, J. D. Reppy, M. Kondo, S. Takada, Y. Shibayama, and A. P. Society, "CORRECTED 20 July 2007; SEE LAST PAGE," *Science (80-.).*, no. July, pp. 1100–1105, 2007.

[72] J. N. D. Kerr and W. Denk, "Imaging in vivo: Watching the brain in action," *Nat. Rev. Neurosci.*, vol. 9, no. 3, pp. 195–205, 2008.

[73] D. Khodagholy *et al.*, "In vivo recordings of brain activity using organic transistors," *Nat. Commun.*, vol. 4, 2013.

[74] M. R. Franz, M. C. Chin, H. R. Sharkey, J. C. Griffin, and M. M. Scheinman, "A new single catheter technique for simultaneous measurement of action potential duration and refractory period in vivo," *J. Am. Coll. Cardiol.*, vol. 16, no. 4, pp. 878–886, 1990.

[75] E. Neher and B. Sakmann, "Single-channel currents recorded from membrane of denervated

frog muscle fibres.," *Nature*, vol. 260, no. 5554, pp. 799–802, Apr. 1976.

[76] D. A. Robinson, "The Electrical Properties of Metal Microelectrodes," *Proc. IEEE*, vol. 56, no. 6, pp. 1065–1071, 1968.

[77] C. A. Thomas, P. A. Springer, G. E. Loeb, Y. Berwald-Netter, and L. M. Okun, "A miniature microelectrode array to monitor the bioelectric activity of cultured cells," *Exp. Cell Res.*, vol. 74, no. 1, pp. 61–66, 1972.

[78] P. Stratton, A. Cheung, J. Wiles, E. Kiyatkin, P. Sah, and F. Windels, "Action potential waveform variability limits multi-unit separation in freely behaving rats," *PLoS One*, vol. 7, no. 6, 2012.

[79] D. A. Rusakov, L. P. Savtchenko, and P. E. Latham, "Noisy Synaptic Conductance : Bug or a Feature ?," *Trends Neurosci.*, vol. 43, no. 6, pp. 363–372, 2020.

[80] D. Darmawan, M. B. Nugroho, R. Goyena, M. B. Nugroho, and L. S. B. A. & Wolfman, " 済無No Title No Title," *J. Chem. Inf. Model.*, vol. 53, no. 9, pp. 1689–1699, 2019.

[81] A. Fendyur, N. Mazurski, J. Shappir, and M. E. Spira, "Formation of essential ultrastructural interface between cultured hippocampal cells and gold mushroom-shaped MEA- towards 'IN-CELL' recordings from vertebrate neurons," *Front. Neuroeng.*, no. NOVEMBER, 2011.

[82] H. Persson, J. P. Beech, L. Samuelson, S. Oredsson, C. N. Prinz, and J. O. Tegenfeldt, "Vertical oxide nanotubes connected by subsurface microchannels," *Nano Res.*, vol. 5, no. 3, pp. 190–198, 2012.

[83] Y. Wu, H. Chen, and L. Guo, "Opportunities and dilemmas of: In vitro nano neural electrodes," *RSC Adv.*, vol. 10, no. 1, pp. 187–200, 2019.

[84] A. F. Mcguire, F. Santoro, and B. Cui, "Interfacing Cells with Vertical Nanoscale Devices: Applications and Characterization," *Annu. Rev. Anal. Chem. Annu. Rev. Anal. Chem*, vol. 111226, no. 1, pp. 1–12, 2018.

[85] M. Nakamura, N. Sato, N. Hoshi, and O. Sakata, "Outer helmholtz plane of the electrical double layer formed at the solid electrode-liquid interface," *ChemPhysChem*, vol. 12, no. 8, pp. 1430–1434, 2011.

[86] M. Chatti *et al.*, *Intrinsically stable in situ generated electrocatalyst for long-term oxidation of acidic water at up to 80 °C*, vol. 2, no. 5. 2019.

[87] Q. Liu, C. Wu, H. Cai, N. Hu, J. Zhou, and P. Wang, "Cell-based biosensors and their application in biomedicine," *Chem. Rev.*, vol. 114, no. 12, pp. 6423–6461, 2014.

[88] H. Helmholtz, "Der phpsik und chemie.," *Ann. der Phys. und Chemie*, vol. 7, p. 22, 1879.

[89] D. L. Chapman, " LI. A contribution to the theory of electrocapillarity ," *London, Edinburgh, Dublin Philos. Mag. J. Sci.*, vol. 25, no. 148, pp. 475–481, 1913.

[90] O. Stern, "ZUR THEORIE DER ELEKTROLYTISCHEN DOPPELSCHICHT," *Zeitschrift für Elektrochemie und Angew. Phys. Chemie*, vol. 30, no. 21-22, pp. 508–516, 1924.

[91] T. Pajkossy and D. M. Kolb, “Double layer capacitance of the platinum group metals in the double layer region,” *Electrochem. commun.*, vol. 9, no. 5, pp. 1171–1174, 2007.

[92] R. Weis, B. Müller, and P. Fromherz, “Neuron adhesion on a silicon chip probed by an array of field-effect transistors,” *Phys. Rev. Lett.*, vol. 76, no. 2, pp. 327–330, 1996.

[93] V. Thakore, P. Molnar, and J. J. Hickman, “An optimization-based study of equivalent circuit models for representing recordings at the neuron-electrode interface,” *IEEE Trans. Biomed. Eng.*, vol. 59, no. 8, pp. 2338–2347, 2012.

[94] S. Ingebrandt, C. K. Yeung, M. Krause, and A. Offenhäusser, “Neuron-transistor coupling: Interpretation of individual extracellular recorded signals,” *Eur. Biophys. J.*, vol. 34, no. 2, pp. 144–154, 2005.

[95] G. Wrobel *et al.*, “Cell-transistor coupling: Investigation of potassium currents recorded with p- and n-channel FETs,” *Biophys. J.*, vol. 89, no. 5, pp. 3628–3638, 2005.

[96] M. E. J. Obien, K. Deligkaris, T. Bullmann, D. J. Bakkum, and U. Frey, “Revealing neuronal function through microelectrode array recordings,” *Front. Neurosci.*, vol. 9, no. JAN, p. 423, 2015.

[97] S. Park, Y. J. Song, H. Boo, and T. D. Chung, “Nanoporous Pt microelectrode for neural stimulation and recording: In vitro characterization,” *J. Phys. Chem. C*, vol. 114, no. 19, pp. 8721–8726, 2010.

[98] W. Whyte, “Cleanroom Technology,” *Cleanroom Technol.*, 2001.

[99] A. Khairnar, “Chapter 2 Thin Film Deposition and Characterization Techniques,” *Thin Film Growth Charact. Tech.*, no. 2014, pp. 1–36, 2010.

[100] F. Yang and J. C. M. Li, *Micro and nano mechanical testing of materials and devices*. 2008.

[101] K. Seshan, *Handbook of Thin Film Deposition Techniques Principles, Methods, Equipment and Applications, Second Editon*. 2002.

[102] P. O. Oviroh, R. Akbarzadeh, D. Pan, R. A. M. Coetzee, and T. C. Jen, “New development of atomic layer deposition: processes, methods and applications,” *Sci. Technol. Adv. Mater.*, vol. 20, no. 1, pp. 465–496, 2019.

[103] R. W. Johnson, A. Hultqvist, and S. F. Bent, “A brief review of atomic layer deposition: From fundamentals to applications,” *Mater. Today*, vol. 17, no. 5, pp. 236–246, 2014.

[104] M. D. Sampson, J. D. Emery, M. J. Pellin, and A. B. F. Martinson, “Inhibiting metal oxide atomic layer deposition: Beyond zinc oxide,” *ACS Appl. Mater. Interfaces*, vol. 9, no. 39, pp. 33429–33436, 2017.

[105] O. Graniel, M. Weber, S. Balme, P. Miele, and M. Bechelany, “Atomic layer deposition for biosensing applications,” *Biosens. Bioelectron.*, vol. 122, no. July, pp. 147–159, 2018.

[106] H. C. M. Knoops, S. E. Potts, A. A. Bol, and W. M. M. Kessels, “Atomic Layer Deposition,” *Handb. Cryst. Growth Thin Film. Ep. Second Ed.*, vol. 3, pp. 1101–1134, 2015.

[107] M. Leskelä and M. Ritala, “Atomic layer deposition (ALD): From precursors to thin film

structures," *Thin Solid Films*, vol. 409, no. 1, pp. 138–146, 2002.

[108] H. B. Profijt, S. E. Potts, M. C. M. van de Sanden, and W. M. M. Kessels, "Plasma-Assisted Atomic Layer Deposition: Basics, Opportunities, and Challenges," *J. Vac. Sci. Technol. A Vacuum, Surfaces, Film.*, vol. 29, no. 5, p. 050801, 2011.

[109] L. Martinu, O. Zabeida, and J. E. Klemberg-Sapieha, *Plasma-Enhanced Chemical Vapor Deposition of Functional Coatings*, Third Edit. Elsevier Ltd., 2010.

[110] J. J. Shea, "Handbook of advanced plasma processing techniques [Book Review]," *IEEE Electr. Insul. Mag.*, vol. 18, no. 1, pp. 48–48, 2005.

[111] "0026-2692/00/$ - see front matter 2000 Elsevier Science Ltd. All rights," vol. 31, p. 2692, 2000.

[112] Microchemicals, "Photoresists AZ and MicroChemicals TI resists." .

[113] D. M. Tennant and A. R. Bleier, "Electron Beam Lithography of Nanostructures," *Compr. Nanosci. Technol.*, vol. 1–5, pp. 35–62, 2011.

[114] K. Hinrichs, K. J. Eichhorn, G. Ertl, D. L. Mills, and H. Lüth, *Ellipsometry of Functional Organic Surfaces and Films*, vol. 52. 2014.

[115] H. G. Tompkins and E. A. Irene, *Handbook of Ellipsometry*. 2005.

[116] D. H. Kim, P. P. Provenzano, C. L. Smith, and A. Levchenko, "Matrix nanotopography as a regulator of cell function," *J. Cell Biol.*, vol. 197, no. 3, pp. 351–360, 2012.

[117] M. J. Dalby, N. Gadegaard, and R. O. C. Oreffo, "Harnessing nanotopography and integrin-matrix interactions to influence stem cell fate," *Nat. Mater.*, vol. 13, no. 6, pp. 558–569, 2014.

[118] A. L. Rosa and M. M. Beloti, "Rat bone marrow cell response to titanium and titanium alloy with different surface roughness," *Clin. Oral Implants Res.*, vol. 14, no. 1, pp. 43–48, 2003.

[119] L. Hanson, Z. C. Lin, C. Xie, Y. Cui, and B. Cui, "Characterization of the cell-nanopillar interface by transmission electron microscopy," *Nano Lett.*, vol. 12, no. 11, pp. 5815–5820, 2012.

[120] F. Liu, D. Wu, R. D. Kamm, and K. Chen, "Analysis of nanoprobe penetration through a lipid bilayer," *Biochim. Biophys. Acta - Biomembr.*, vol. 1828, no. 8, pp. 1667–1673, 2013.

[121] D. Gusnard and R. H. Kirschner, "Cell and organelle shrinkage during preparation for scanning electron microscopy: effects of fixation, dehydration and critical point drying.," *J. Microsc.*, vol. 110, no. 1, pp. 51–57, May 1977.

[122] K. Cortese, G. Vicidomini, M. C. Gagliani, P. Boccacci, A. Diaspro, and C. Tacchetti, *High data output method for 3-D correlative light-electron microscopy using ultrathin cryosections*, vol. 950. 2013.

[123] N. Chaffey, "Hayat MA. 2000. Principles and techniques of electron microscopy: biological applications. 4th edn. 543pp. Cambridge: Cambridge University Press. £65 (hardback).," *Ann. Bot.*, vol. 87, no. 4, pp. 546–548, 2001.

[124] H. N. Southworth, *Scanning Electron Microscopy and Microanalysis*. 1975.

[125] S. Eick, “Extracellular Stimulation of Individual Electrogenic Cells with Micro-Scaled Electrodes,” *Fak. fuer Elektrotechnik und Informationstechnik*, vol. PhD, 2009.

[126] M. Dipalo *et al.*, “3D plasmonic nanoantennas integrated with MEA biosensors,” *Nanoscale*, 2015.

[127] X. Xie, A. M. Xu, S. Leal-ortiz, Y. Cao, C. C. Garner, and N. A. Melosh, “Nanostraw À Electroporation System for Highly E ffi cient Intracellular Delivery and Transfection,” no. 5, pp. 4351–4358, 2013.

[128] S. Kaech and G. Banker, “Culturing hippocampal neurons,” *Nat. Protoc.*, vol. 1, no. 5, pp. 2406–2415, 2006.

[129] N. Cell, *bok%3A978-1-59259-207-4*. .

[130] J. Riedl *et al.*, “Lifeact: A versatile marker to visualize F-actin,” *Nat. Methods*, vol. 5, no. 7, pp. 605–607, 2008.

[131] H. Y. Lou *et al.*, “Membrane curvature underlies actin reorganization in response to nanoscale surface topography,” *Proc. Natl. Acad. Sci. U. S. A.*, vol. 116, no. 46, pp. 23143–23151, 2019.

[132] G. Panaitov, S. Thiery, B. Hofmann, and A. Offenhäusser, “Fabrication of gold micro-spine structures for improvement of cell/device adhesion,” *Microelectron. Eng.*, vol. 88, no. 8, pp. 1840–1844, 2011.

[133] V. P. Collins, B. Arborgh, and U. Brunk, “A comparison of the effects of three widely used glutaraldehyde fixatives on cellular volume and structure. A TEM, SEM, volumetric and cytochemical study,” *Acta Pathol. Microbiol. Scand. - Sect. A Pathol.*, vol. 85, no. 2, pp. 157–168, 1977.

[134] D. Fakult, “Quantification and Improvement of the Electric Coupling between Electrogenic Cells and Microelectrode Arrays by Nanocavities and Nanostructures.”

[135] D. Braun and P. Fromherz, “Imaging neuronal seal resistance on silicon chip using fluorescent voltage-sensitive dye,” *Biophys. J.*, vol. 87, no. 2, pp. 1351–1359, 2004.

[136] J. R. Buitenweg, W. L. C. Rutten, W. P. A. Willems, and J. W. Van Nieuwkasteele, “Measurement of sealing resistance of cell-electrode interfaces in neuronal cultures using impedance spectroscopy,” *Med. Biol. Eng. Comput.*, vol. 36, no. 5, pp. 630–637, 1998.

[137] D. Jäckel *et al.*, “Combination of High-density Microelectrode Array and Patch Clamp Recordings to Enable Studies of Multisynaptic Integration,” *Sci. Rep.*, vol. 7, no. 1, pp. 1–17, 2017.

[138] J. Abbott *et al.*, “Extracellular recording of direct synaptic signals with a CMOS-nanoelectrode array,” *Lab Chip*, vol. 20, no. 17, pp. 3239–3248, 2020.

References

Appendices

Appendix 1

Deposition and structuring the metal layer

Figure A1.1 demonstrates the fabrication flow of the nanocavity MEAs in detail. First of all, lithography step was required in order to structure the metallization. For that, silicon wafer with a 1 µm thick insulating layer of silicon oxide was placed on a hot plate at 150 °C for 10 min for the purpose of dehydration of the water. Before applying the metal layer, the photoresist was required to structure the area. Double stack of resist was applied on the sample, which consist of, 4 ml of an undercut resist (LOR3b, MicroChemicals GmbH, Ulm, Germany) at 3000 rpm (rotation per minute) for 35 s with an acceleration of 500 rpm/s2 followed by a soft baked at 150 °C for 5 min, and 3.5 ml of a negative resist (AZ nLOF 2020, MicroChemicals GmbH, Ulm, Germany) with the same spin coating rate and soft baked at 110 °C for 1 min. Then the resists were exposed through a chromium mask in the mask aligner (Süss, MA-4 with 365 nm UV light source) for 1.4 s using the hard contact mode. Afterwards, post exposure bake at 110 °C for 1min was done. The resists then developed in MIF 326 (2.38% tetramethylammoniumhydroxid (TMAH) in H2O, MicroChemicals GmbH, Ulm, Germany) dissolving the exposed and undesired area, resulting in a structured feedlines. Metal then was deposited onto the sample via electron beam evaporation (Univex 400, Leybold GmbH, Cologne, Germany). This metal stack consists of a 20nm titanium, 200nm platinum/ gold, and 80nm of chromium layer. Finally the remaining resist was removed via lift-off process by immersing the wafer in to the acetone overnight and removing the negative AZ nLOF 2020 resist. After that, to remove the undercut LOR3b resist, the wafer was immersed into MIF326 for 5 min. To remove the chemical compounds, wafer was then rinsed and cleaned with deionized water and dried in a dry centrifuge and N_2 gun.

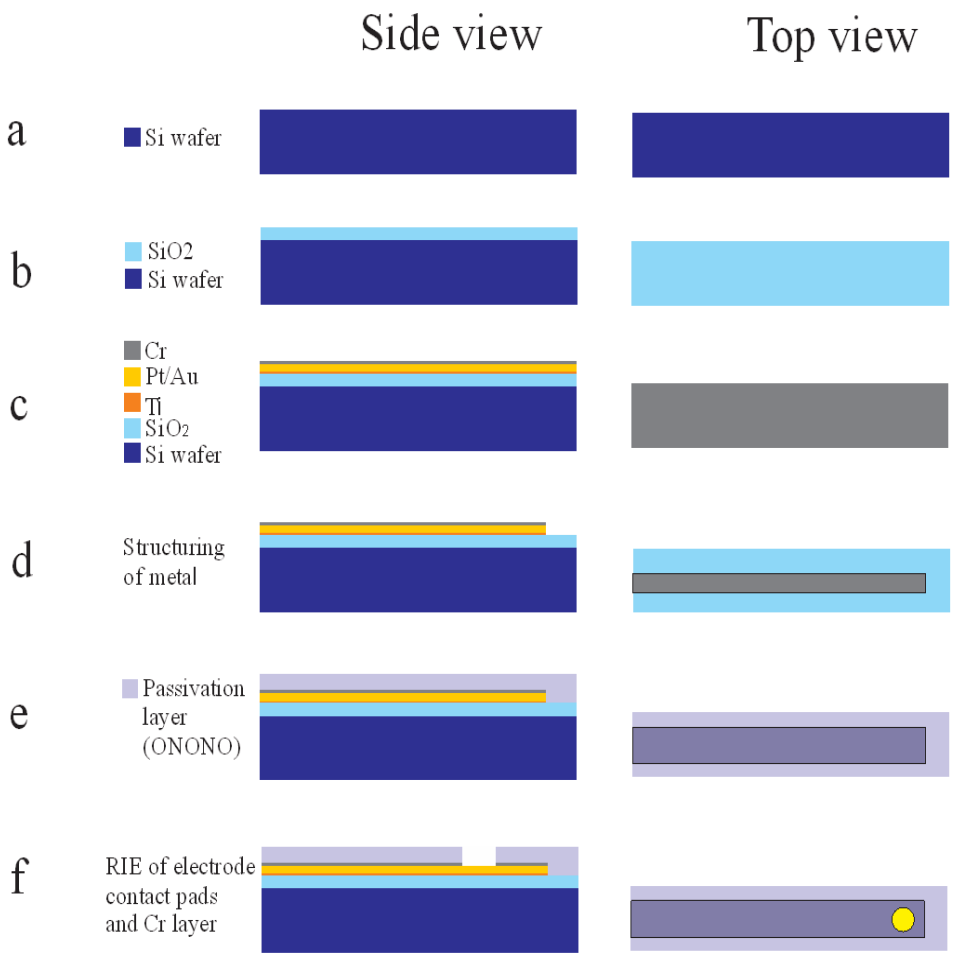

Figure A1.1 Schematic fabrication flow of microelectrode arrays. a: Si wafer. b: Thermal Oxidation using oxygen results in a thin layer (1 µm) of SiO2. c: Metal evaporation, through electron beam evaporation, results in a stack of Ti/ Pt or Au/ Cr. d: Structuring the metal stack via photolithography. e: Deposition of insulating layer (ONONO) via PECVD. f: Structuring and opening the electrode area and contact pads through photolithography, followed by RIE process.

Deposition and structuring of the ONONO layer

For the next step, deposition and structuring the passivation layer was employed. The process steps were represented in Figure A1.1.
First, plasma enhanced chemical vapor deposition (PECVD) was applied (SENTECH instruments GmbH, Berlin, Germany). A total 800 nm thicknesses of SiO_2 and Si_3N_4 was deposited, which means, three stack of SiO_2 (each 200nm) and two stack of Si_3N_4 (each 100nm) were covered at the entire wafer. In Table A1.1, the recipe for the deposition of SiO_2 and Si_3N_4 is demonstrated. SiO_2 is generated with the combination of 7.3 standard liter per minute (slm) monosilane (SiH_4) and 10.5 slm of oxygen (O_2) with pressure of 1 Pa. And for production of Si_3N_4, 7.8 slm of monosilane and 10slm of ammonia (NH_3) are used while the pressure is increasing to 8 Pa. The entire process was done at 280°C and the inductively coupled plasma radio frequency (ICP-RF) was 500W.

	SiO_2	Si_3N_4
Layer thickness[nm]	200	100
Process gases	SiH4/O2	SiH4/NH3
Gas flow [slm]	7.3/10.5	7.8/10
Process time [s]	500	500
ICP-RF [W]	500	500
Temperature [°C	280	280
Pressure [Pa]	1.0	8.0

Table A1.1. Detailed parameters of deposition of ONONO via PECVD system.

After the deposition of ONONO passivation layer, in order to open the recording area and the contact pads, second lithography was required. The wafer was dehydrated at 150 °C for 10 min. Then, a positive 3 ml of positive resist (AZ 5214 E, MicroChemicals GmbH, Ulm, Germany) was spin coated at 4000 rpm for 35 S with the acceleration of 500 rpm/s, and was soft baked at 110 °C for 1 min. Afterwards, the resist was exposed with mask aligner (Süss MA-4) in the hard contact mode. For placement of the opening of the ONONO layer exactly in the electrode are and the contact pads, before the exposure, the alignment of the mask and the wafer was necessary. UV light was exposed on the wafer for 5 sec through the mask with the 6 µm and 10 µm for electrode opening and the area of contact pads. After the exposure, the development needed to be performed, therefore the wafer was inserted into MIF326 for 1 min and washed with water to stop the development and clean the wafer.

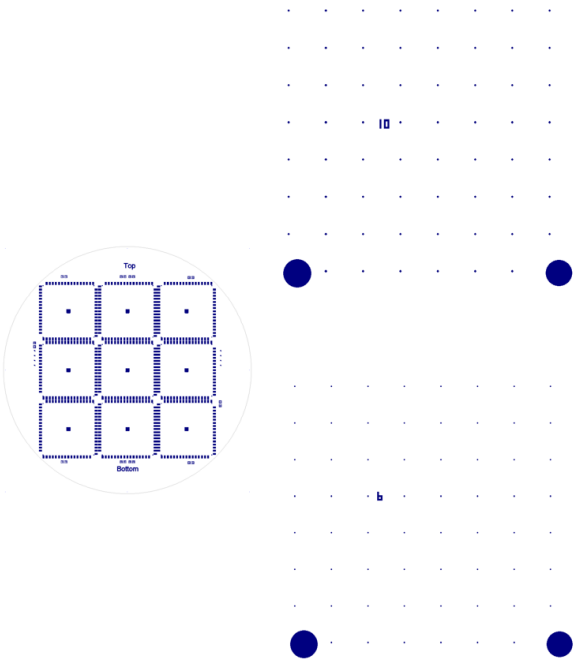

Figure A1.2 Schematic of the wafer scale mask of MEAs. in the left, 4 inch wafer contains 9 chips of with 1inch size and each MEA (right) contains 62 electrodes and 2 reference electrodes In this work, two different electrode diameters are use. 6 and 10 µm.

Reactive ion etching (RIE; Oxford Instruments, Abingdon, United Kingdom) was used for the opening of the ONONO layer. In total 64 openings in the electrodes and 64 contact pads were etched. Table 2 shows the parameters used for the physical etching process. Tetrafluoromethane (CF_4; 20 sccm), trifluoromethane (CHF_4; 20sccm), and oxygen (O_2, 2 sccm) were the process gases used for the etching. With etching rate of 21 nm/min, the complete etch time for the 800 nm ONONO takes 38 min. The radio frequency (RF) power was 150 W and the bias voltage was 350 W. The pressure during the entire process was 0.002 mbar.

	RIE of ONONO
Layer thickness[nm]	800
Process gases	CF4/CHF3/O2
Gas flow [sccm]	20/20/2
Process time [min]	38
Etch rate [nm/min]	22
RF power [W]	150
ICP power [W]	0
Bias voltage [V]	350
Pressure [mbar]	0.02

Table A1.2 Detail parameters for etching the ONONO layer, via RIE.

After all the etching process, the resist (positive resist AZ5214 E) remains on the wafer as a protection layer for MEAs during the sawing process. The wafer was cut into nine MEAs with the size of 1 x 1 inches each (DAD 3350 dicing saw, DISCO Corporation, Tokyo, Japan). Afterwards, the resist was removed from the sample by immersing into acetone followed by isopropanol, 20 min each. In the end samples are cleaned with deionized water (DI-water) and dried carefully in a stream of nitrogen. The fabrication process was completed.

Appendix 2

Sterilization

Prior to culture, samples must be cleaned. For this purpose, sample cleaning and sterilization are carried out, immersing into 70% ethanol for 30 sec, and rinsing twice with autoclaved Milli-Q water.

Cortical Rat neurons

Cortices were removed from E18 wister rats (animal testing approval: Landesumweltamt für Natur, Umwelt und Verbraucherschutz, Nordrhein-Westfalen, Recklinghausen, Germany, number 81-02.04.2018.A) and separated into individual cells by incubation at 37 °C with 0.05% trypsin EDTA (Life Technologies GmbH, Darmstadt, Germany), 5% CO_2, and 95% humidity for 10 min. Then the tissue was gently removed. Tissue then was washed 5 times with Supplemented Neurobasal medium (NB medium, Life Technologies GmbH, Darmstadt, Germany), 1% B-27 supplement (Life Technologies GmbH, Darmstadt, Germany), 0.5 mM L-glutamine (Life Technologies GmbH, Darmstadt, Germany) and 50 µg/ml of gentamicin (Sigma-Aldrich, Steinheim, Germany). After the last washing step, the supernatant was replaced with fresh supplemented Neurobasal medium and the tissue was triturated until the tissue was completely dissociated. Cells were counted with Neubauer improved cell counting chamber and 500000 cortical neurons in 3 ml supplemented Neurobasal medium were plated onto each sample. The samples then were kept at 37 °C and 5% CO_2. One to four hours after cell seeding, the medium was replaced completely with medium. From the first day *in vitro*, every three to four days, half of the medium was replaced with fresh warm medium.

Neuronal Media supplements

Media	Neuro Basal Media	10 mL
Serum	B-27	100 µL
Glutamine	Glutamine	25 µL
Antibiotic	Gentamycin	10 µL

Table A1.3 Substances to add to 10 mL supplement media for neuronal growth culture.

Sample cleaning

In order to reuse the sample after neuronal culture, the surface of the substrate can be cleaned from the cellular layer. This procedure is done with Trypsin EDTA, right after culture, at 37 °C two times for at least 1hour each. Afterwards samples are immersed into 1%Tergazyme solution in ultrapure-water, which is a concentrated ionic detergent with protease enzyme, for 10 min. finally, rinsing samples carefully in running water.

Appendix 3

Abbreviations

AC	Alternating current
ADC	Analog-to-digital converter
ALD	Atomic layer deposition
AP	Action potential
CMOS	Complementary metal oxide semiconductor
CPD	Critical point drying
CVD	Chemical vapor deposition
DIV	Days in vitro
EDX	Energy-dispersive X-ray
EEG	Electroencephalography
EIS	Electrochemical impedance spectroscopy
EtOH	Ethanol
FIB	Focused ion-beam
GHK	Goldman-Hodgkin-Katz
HBSS	Hank's balanced salt solution
IHP	Inner Helmholtz plane
IrOx	Iridium oxide
MEA	Microelectrode array
OHP	Outer Helmholtz plane
PBS	Phosphate buffered saline
PDMS	Polydimethylsiloxane
PECVD	Plasma-enhanced chemical vapor deposition
PLL	Poly-L-lysine hydrobromide
PVD	Physical vapor deposition
PSP	Post synaptic potential
RIE	Reactive ion etching
SEM	Scanning electron microscopy
SNR	Signal-to-noise
TiO_2	Titanium oxide
vol%	Volume percent
wt%	Weight percent

Appendices

List of Figures

List of tables

List of publications and conferences

Peer-reviewed publications

- Xiaobo Yuan, Nikolaus Wolf, Timm J. J. Hondrich, **Pegah Shokoohimehr**, Frano Milos, Manuel Glass, Dirk Mayer, Vanessa Maybeck, Michael Prömpers, Andreas Offenhäusser, and Roger Wördenweber,
"Engineering Bio-compatible Interfaces via Combinations of Oxide Films and Organic Self-Assembled Monolayers"
ACS Applied Materials & Interfaces, 12 (14), 17121-17129 (2020)
DOI: 10.1021/acsami.0c02141

- Timm J. J. Hondrich, Bohdan Lenyk, **Pegah Shokoohimehr**, Dmitry Kireev, Vanessa Maybeck, Dirk Mayer, and Andreas Offenhäusser
"MEA Recordings and Cell−Substrate Investigations with Plasmonic and Transparent, Tunable Holey Gold"
ACS Applied Materials & Interfaces, 11 (50), 46451-46461 (2019)
DOI: 10.1021/acsami.9b14948

- D. Kireev, **P. Shokoohimehr**, M. Ernst, V. Montes, K. Srikantharajah, V. Maybeck, A. Offenhäusser
"Fabrication of ultrathin and flexible graphene-based devices for in vivo neuroprosthetics"
MRS Advances 3(29), 1621-1627 (2018)
DOI: 10.1557/adv.2018.94

Contributions in Workshops, conferences and schools

- Dmitry Kireev, **Pegah Shokoohimehr**, Vanessa Maybeck, Bernhard Wolfrum, Andreas Offenhäusser,
"Flexible and Implantable Graphene Based Neural Probes, International Conference on Materials Design for Neural interfaces". MRS-2017 fall meeting

- Workshop of Oxford Instruments, 2017, Aachen, Germany

- **Pegah Shokoohimehr**, “Brain Penetraiting Electrodes)” (oral presentation) winter School “Neurotechnology: Fundamentals & Applications”, Hirschegg, Austria, 2018.

- Workshop and Training of Presenting for Scientists, 2019, Jülich, Germany

- **Pegah Shokoohimehr**, “Recording with CMOS (MEAs)” (oral presentation) Summer School “Bioelectronics: from in vitro to in vivo applications”, Hirschegg, Austria, 2019.

Band / Volume 63
Novel System Approach for a mm-range Precision Indoor Positioning System
R. Xiong (2020), xi, 144 pp
ISBN: 978-3-95806-517-8

Band / Volume 64
Quantitative investigation of group III-nitride interfaces by a combination of scanning tunneling microscopy and off-axis electron holography
Y. Wang (2021), 102 pp
ISBN: 978-3-95806-534-5

Band / Volume 65
Scalable Control Electronics for a Spin Based Quantum Computer
L. Geck (2021), xiv, 114, xv-xxxiii
ISBN: 978-3-95806-540-6

Band / Volume 66
DNA-capped silver nanoparticles for stochastic nanoparticle impact electrochemistry
L. Nörbel (2021), VI, 142 pp
ISBN: 978-3-95806-541-3

Band / Volume 67
Development, characterization, and application of intraretinal implants
V. Rincón Montes (2021), XII, 173 pp
ISBN: 978-3-95806-553-6

Band / Volume 68
Optogenetic and electrical investigation of network dynamics in patterned neuronal cultures
T. J. J. Hondrich (2021), x, 177 pp
ISBN: 978-3-95806-555-0

Band / Volume 69
Disentangling parallel conduction channels by charge transport measurements on surfaces with a multi-tip scanning tunneling microscope
S. Just (2021), xii, 225 pp
ISBN: 978-3-95806-574-1

Band / Volume 70
Nanoscale four-point charge transport measurements in topological insulator thin films
A. Leis (2021), ix, 153 pp
ISBN: 978-3-95806-580-2

Band / Volume 71
Investigating the Interaction between π-Conjugated Organic Molecules and Metal Surfaces with Photoemission Tomography
X. Yang (2021), xviii, 173 pp
ISBN: 978-3-95806-584-0

Band / Volume 72
Three-Dimensional Polymeric Topographies for Neural Interfaces
F. Milos (2021), 133 pp
ISBN: 978-3-95806-586-4

Band / Volume 73
Development, characterization, and application of compliant intracortical implants
K. Srikantharajah (2021), xiv, 155, xv-xvii pp
ISBN: 978-3-95806-587-1

Band / Volume 74
Modelling, implementation and characterization of a Bias-DAC in CMOS as a building block for scalable cryogenic control electronics for future quantum computers
P. N. Vliex (2021), xiv, 107, xv-xxviii pp
ISBN: 978-3-95806-588-8

Band / Volume 75
Development of Electrochemical Aptasensors for the Highly Sensitive, Selective, and Discriminatory Detection of Malaria Biomarkers
G. Figueroa Miranda (2021), XI, 135 pp
ISBN: 978-3-95806-589-5

Band / Volume 76
Nanostraw- Nanocavity MEAs as a new tool for long-term and high sensitive recording of neuronal signals
P. Shokoohimehr (2021), xi, 136 pp
ISBN: 978-3-95806-593-2

Information
Band / Volume 76
ISBN 978-3-95806-593-2

Mitglied der Helmholtz-Gemeinschaft

JÜLICH
Forschungszentrum